Study of Different Quantum Phases in Magic-angle Twisted Bilayer Graphene

Ipsita Das

Supervisor: Prof. Dmitri K. Efetov

A thesis presented for the award of the degree of
Doctor of Philosophy

Universitat Politècnica de Catalunya
Spain
January 2023

To my Baba, Maa and Didu.....

Contents

Acknowledgements

Abstract

The discovery of two dimensional materials opened a unique pathway to study the electronic properties of quantum materials which are otherwise absent in bulk systems. Soon after the discovery of graphene (2004), a plethora of 2D materials were found with various diverse properties such as metals, insulators, semiconductors, superconductors, magnets etc. Besides having different properties than bulk systems, these materials can be assembled by using the Van der Waals force, which greatly extends the possibilities of studying new phenomena. For a long time, van der Waals heterostructures have been made by vertically stacking one layer on top of another in which the lattice mismatch occurs only due to the translation. However, twist angle plays an interesting tuning knob to engineer the electronic properties of the 2D heterostructures. Following long standing theoretical predictions, people have observed exotic quantum phenomena in twisted bilayer graphene in 2018.

In this thesis, we have studied the electronic properties of magic angle twisted bilayer graphene (MATBG), which consists of two graphene layers rotated with respect to each other by an angle $\theta = 1.1^{\circ}$. It has been experimentally shown that MATBG possesses flat electronic bands in the low energy scale. This flat band hosts multiple correlated phenomena such as correlated insulators, superconductivity, magnetism etc.

We have studied different phases of MATBG in the presence of a magnetic field to reveal the zero-field ground state of the system. In the presence of a small magnetic field ($B < 3$ T), the Hall conductance of MATBG shows quantized value with the Chern numbers $C = \pm 1$, ± 2, ± 3 and ± 4 which nucleate from different integer fillings of the moiré bands, $\nu = \pm 3$, ± 2, ± 1 and 0, respectively. These phases can be interpreted as spin and valley polarized many body Chern insulators. The exact sequence and correspondence of the Chern numbers and

filling factors suggest that these states are directly driven by electronic interactions, which specifically break the time-reversal symmetry in the system.

We have also studied the evolution of the phase space of MATBG in high magnetic field and explored the Hofstadter spectrum. Due to the large moiré unit cell area MATBG reaches one full flux quantum (ϕ_0) per moiré unit cell close to 30 T. We studied a detailed magnetotransport behaviour of the system upto $B = 31$ T, corresponding to (ϕ_0). At (ϕ_0), a series of re-entrant correlated insulators are observed at the filling factors $\nu = +2, +3$. Interaction driven Fermi surface reconstruction is also observed at other fillings of the band which are identified by the emergence of new set of Landau levels.

We further studied the higher energy dispersive bands in MATBG in the presence of magnetic field. The analysis of the Landau level crossings in the Rashba-like dispersive bands enables a parameter free comparison to a newly derived magic series of level crossings in a magnetic field and provides constraints on the parameters of the Bistritzer-MacDonald MATBG Hamiltonian. For the first time, this allows us to experimentally verify the band structure of MATBG.

In the next section of this thesis, we have studied the effect of an important parameter, Coulomb screening on the ground state of the quantum phases such as correlated insulator and superconductor. The coexistence of these two states prompts intriguing questions about their relationships. We have directly tuned the electronic correlations by changing the separation distance between the graphene and a metallic screening layer. Correlated insulators are suppressed when the separations are smaller than the typical Wannier orbital size (15 nm) and also in devices with twist angles that slightly deviate from magic angle ($\theta = 1.10^\circ \pm 0.05^\circ$). Upon extinction of the insulating orders, the vacated phase space is taken over by superconducting domes that feature critical temperatures comparable to those in devices with strong insulators. Finally, we study the temperature dependence of the resistivity in MATBG and unveil a strange metal phase upto a very low temperature $T = 40$ mK.

We thus have experimentally demonstrated the effect of several external parameters, such as magnetic field, screening, temperature etc. on the ground state of MATBG and how they alter the microscopic mechanisms of different correlated phenomena in the system.

Resumen

El descubrimiento de materiales bidimensionales abrió un camino único para estudiar las propiedades electrónicas de los materiales cuánticos que son otros por lo demás ausente en los sistemas a granel. Poco después del descubrimiento del grafeno (2004), se encontró una plétora de materiales 2D con diversos propiedades tales como metales, aislantes, semiconductores, superconductores, imanes etc. Además de tener propiedades diferentes a los sistemas a granel, estos materiales se pueden ensamblar utilizando el van der Waals fuerza, lo que amplía enormemente las posibilidades de estudiar nuevos fenómenos. Durante mucho tiempo, las heteroestructuras de van der Waals se han hecho apilando verticalmente una capa encima de otra en la que la red el desajuste ocurre solo debido a la traducción. Sin embargo, el ángulo de torsión juega un botón de ajuste interesante para diseñar las propiedades electrónicas de las heteroestructuras 2D. Siguiendo predicciones teóricas de larga data, la gente ha observado fenómenos cuánticos exóticos en grafeno bicapa retorcido en 2018.

En esta tesis, hemos estudiado las propiedades electrónicas del grafeno bicapa torcido de ángulo mágico (MATBG), que consiste en dos capas de grafeno rotadas entre sí por un ángulo $\theta = 1.1°$. Se ha demostrado experimentalmente que MATBG posee bandas electrónicas planas en la escala de baja energía. Esta banda plana alberga múltiples fenómenos correlacionados, como aislantes, correlacionados, superconductividad, magnetismo, etc.

Hemos estudiado diferentes fases de MATBG en presencia de un campo magnético para revelar el estado fundamental de campo cero del sistema. En presencia de un pequeño campo magnético (B < 3 T), la conductancia de Hall de MATBG muestra un valor cuantificado con los números de Chern C = ± 1, ± 2, ± 3 y ± 4 que se nuclean a partir de diferentes rellenos enteros del muaré e bandas, $\nu = \pm 3$, ± 2, ± 1 y 0, respectivamente. Estas fases pueden ser interpretado como espín y

valle polarizado de muchos aisladores Chern de cuerpo. La secuencia exacta y la correspondencia de los números de Chern y los factores de llenado sugieren que estos estados están directamente impulsados por interacciones electrónicas, que rompen específicamente la simetría de inversión de tiempo en el sistema.

También hemos estudiado la evolución del espacio de fase de MATBG en alto campo magnético y exploró el espectro de Hofstadter. Debido a el gran área de celda unitaria muaré MATBG alcanza un cuanto de flujo completo (Φ_0) por celda unitaria muaré cercana a 30 T. Estudiamos un detalle comportamiento de magnetotransporte del sistema hasta $B = 31$ T, correspondiente a (Φ_0). En (Φ_0), se observa una serie de aisladores correlacionados reentrantes en los factores de llenado $\nu = +2, +3$. Superficie de Fermi impulsada por la interacción también se observa reconstrucción en otros rellenos de la banda que son identificado por la aparición de un nuevo conjunto de niveles de Landau.

Estudiamos más a fondo las bandas dispersivas de mayor energía en MATBG en presencia de campo magnético. El análisis del nivel de Landau Los cruces en las bandas dispersivas similares a Rashba permiten una comparación sin parámetros con una serie mágica recién derivada de cruces a nivel en un campo magnético y proporciona restricciones en los parámetros del Bistritzer-MacDonald MATBG Hamiltonian. Por primera vez, esto nos permite verificar experimentalmente la estructura de bandas de MATBG.

En la siguiente sección de esta tesis, hemos estudiado el efecto de un parámetro importante, detección de Coulomb en el estado fundamental de la fases cuánticas como aislante correlacionado y superconductor. La coexistencia de estos dos estados genera preguntas intrigantes sobre sus relaciones. Hemos sintonizado directamente las correlaciones electrónicas cambiando la distancia de separación entre el grafeno y una capa de protección metálica. Los aisladores correlacionados se suprimen cuando las separaciones son más pequeñas que el tamaño orbital típico de Wannier (15 nm) y también en dispositivos con ángulos de giro que se desvían ligeramente del ángulo mágico ($\theta = 1.1° \pm 0.05°$). Tras la extinción de las órdenes de aislamiento, el espacio de fase vacante es ocupado por domos superconductores que presentan temperaturas críticas comparables a las de los dispositivos con fuertes aislantes. Finalmente, estudiamos la dependencia de la temperatura de la resistividad en MATBG y revelamos una extraña fase metálica hasta una temperatura muy baja $T = 40$ mK.

Por lo tanto, hemos demostrado experimentalmente el efecto de varios parámetros externos, como campo magnético, detección, temperatura etc. sobre el estado fundamental de MATBG y cómo alteran los mecanismos microscópicos de diferentes fenómenos correlacionados en el sistema.

Chapter 1

Introduction

The electronic properties of two dimensional materials have been intensively studied in the field of experimental condensed matter physics over the last few decades. Many of the quantum materials derive their properties from reduced dimensionality, in particular from the confinement of electrons in two dimensional sheets. Research has been conducted in order to understand the complex two dimensional quantum materials in which electrons cannot be considered as independent particles but interact strongly and give rise to collective excitations known as quasiparticles. These understandings have been even employed to engineer new materials with completely different properties to improve the modern electronics.

In this thesis we will study the electronic properties of magic angle twisted bilayer graphene (MATBG), in which two layers of monolayer graphene are rotated with respect to each other by an angle (θ). While rotated by a specific angle ($\theta = 1.1^{\circ}$), this system encompasses a set of flat bands which host multiple strongly correlated phenomena.

In this introductory chapter, we will start with the description of 2D materials and their diverse properties starting from the discovery of graphene. Later, we will describe the van der Waals heterostructures, in which multiple two dimensional sheets can be assembled together to engineer completely new properties in the system. Another new and relatively unexplored direction is called the twistronics. In this method, different 2D quantum materials can be twisted with respect to each other to manipulate their band structure and electronic properties. We will discuss this in details in the next section of this chapter. We will then briefly discuss the advantage of studying twisted bilayer

graphene over other strongly correlated systems in condensed matter physics. Finally, we will end this chapter with a short outline of this thesis.

1.1 Two dimensional materials

During the first decades of 20th century, the existence of two dimensional (2D) materials was a highly debatable issue in the physics community. According to classical physics, 2D materials are highly unstable in any finite temperature due to the thermal fluctuation of lattice [1, 2]. This was in agreement with the observed decreasing melting temperature with the decreasing thickness of the thin films. The development of modern spectroscopy revealed the existence of 3D materials with layered structure, such as graphite or molybdenum-disulphide. Even though their exfoliation down to their two dimensional monolayers was thought to be possible only in the theoretical domain since Mermin demonstrated that strictly one and two dimensional materials can only exist hypothetically, i.e. if the crystal is described within the harmonic approximation [3].

Materials science had a major scientific breakthrough in 2004, when Andrei Geim and Konstantin Novoselov isolated a single layer of graphene from the bulk graphite by using a very simple technique, called mechanical exfoliation with scotch tape [4]. This one atom layer thick graphene showed exceptional electrical and mechanical properties [5, 6]. The discovery of graphene opened an avenue of 2D research. The importance of this achievement was sealed in 2010, when A. Geim and K. Novoselov were awarded the Nobel prize.

Soon after the discovery of graphene, an enormous number of 2D materials have been isolated from the bulk by the same method in the past decade. Among these, the most notable examples are a large class of transition metal dichalcogenides (TMDCs) [7]. The recent progress in exfoliation techniques such as micromechanical cleavage, ion intercalation, and surfactant-assisted ultrasonication has set the foundations for the manufacturing of essentially any given layered bulk material in the monolayer limit. To date, the isolated 2D materials cover almost all different phases of condensed matter, such as, metal, semiconductor, insulator, superconductor, topological insulator, ferromagnets etc [8–10]. Theses materials can be tuned in multiple different ways

by changing their chemical composition, crystallographic phases, carrier densities, local potential etc. The vastness of these materials and the innumerable ways to tune their properties further, brings unprecedented richness to the field of 2D materials.

Surprisingly, the 2D crystals are not only continuous but also exhibit high crystal quality. The latter is very important in case of graphene in which electrons can travel thousands of interatomic distances without scattering [4, 11, 12]. With the benefit of hindsight, the existence of such one-atom-thick crystals can be reconciled with theory. Indeed, it can be argued that the obtained 2D crystallites are quenched in a metastable state because they are extracted from 3D materials, whereas their small size ($<<$ 1 mm) and strong interatomic bonds ensure that thermal fluctuations cannot lead to the generation of dislocations or other crystal defects even at elevated temperature. However, a counter argument can be drawn where the 2D crystals gets stabilized by gentle crumpling in the third dimension. This 3D warping increases the elasticity and decreases the thermal vibration, making the 2D crystal stable [13, 14].

In general, for most of the 2D materials, loss of dimensionality gives rise to very different properties than the 3D bulk system. For example, the parent compound graphite is metallic but graphene is semi-metallic. In general, TMDCs have indirect band gap in their bulk, but the isolated monolayers have direct band gap which make them attractive for optical studies.

With the rise of tons of 2D materials and their vast properties, people started assembling multiple 2D layers together to alter the electronic properties of the product which is completely different than the parent materials. In the next section we will discuss this in detail.

1.2 Van der Waals heterostructures

All 2D materials can be easily separated from their bulk because they are stacked together in the three dimensional system by a weak force called van der Waals (vdW) force. Even before the discovery of graphene, the layered structure of graphite materials were confirmed by multiple studies and believed that it's 2D counterpart can not be derived in reality [15]. However, thanks to the weak vdW force, people have managed to isolate them in nature. The vdW force originates from the

quantum fluctuation of the electromagnetic fields and almost two to three magnitude smaller than the typical chemical bonds. This weak force endows the exfoliability of the layered materials - the ability to be thinned down mechanically, exfoliation.

Different 2D materials can also be assembled together by vdW force if they are brought sufficiently close to each other. This beautiful process gives rise to the vertical assembly of different 2D materials, called van der Waals heterostructure [16, 17]. There are other methods which can successfully combine multiple 2D layers together such as evaporation and molecular beam epitaxy (MBE) etc. However, the atomically clean interface has only been achieved by van der Waals heterostructure so far. The major advantages of the vdW heterostructures over other conventional heterostructures are,

1. Atomically sharp interfaces. By mechanical stacking one can control the number of layers of each 2D materials and there are not any chemical treatment involved in the process. Therefore, atomically sharp and clean interfaces can be easily achieved in vdW heterostructures [18]. It is highly nontrivial that the contamination inevitably present on top of 2D crystals and trapped during their assembly segregates into isolated pockets, leaving the buried interfaces clean and atomically flat in vdW heterostructures.

2. Isolation from the environment. vdW heterostructures presents an opportunity to isolate the 2D materials in focus from its environment by encapsulating with other 2D materials without altering its properties. For example, people observed that the electrical properties and mobility of graphene were enhanced significantly by encapsulating it with insulating hexagonal boron nitride (hBN) layers. Firstly, this hBN layers protect the graphene from any type of chemical doping that might arise during the fabrication of the device. Secondly, it also screens any charge puddle present in the substrate which also affect the properties of graphene [19–21].

3. In other growth processes (MBE etc.), lattice structure of one material greatly affects the other material growing on top and alters its properties by inducing strain etc. A small lattice mismatch between two layers changes the overall properties of the

system. However, this problem is easily avoided in vdW heterostructures. Each layer of 2D materials is separately prepared and then assembled together in vdW heterostructures and the effect of one layer is completely absent in other layers.

4. Electrostatic tunability. As the dimensionality is reduced in 2D vdW heterostructures, the charge carrier density also decreases within the system than 3D and makes it possible to tune the carrier density by applying electrostatic gate voltage. Although gating is also possible in semiconductor heterostructures, the gate tunability of vdW heterostructures is order of magnitudes higher. Additionally, introduction of ionic liquid gates makes the possibility of gate tuning even wider.

5. Finally, the ease of fabrication. The vdW heterostructures can be made in any lab without the need of expensive MBE systems.

For these reasons, in recent years many condensed matter experiments which once used to be studied semiconductors such as Si or GaAs, are now being performed in different vdW heterostructures. In particular, the eldest member of the 2D material family, graphene and its derivatives, have so far been the most popular platform due to its robustness and ultrahigh charge mobility that rivals GaAs quantum wells.

A basic 2D vdW heterostructure is shown in Figure 1.1. This structure is suitable for studying the electronic properties of graphene. Generally, the substrate is silicon oxide on top of silicon (Si/SiO_2). The monolayer graphene is sandwiched between two hBN layers from both top and bottom. These two hBN layers serve a very good encapsulating layers and protect from chemicals and charge puddles in SiO_2. The bottom gate can be made either with metal or with graphite to electrostatically tune the carrier density of graphene. It has been recently realised that the local gate shows better tunability and clean phases than the global silicon oxide gate.

The thicknesses of the hBN flakes are typically in the range of 5 nm to 100 nm. This range of thickness is a compromise between substrate screening which prefers thicker flakes and ease of fabrication which prefers thinner flakes. It has been shown that the encapsulation with hBN significantly reduces the charge puddles from the substrate

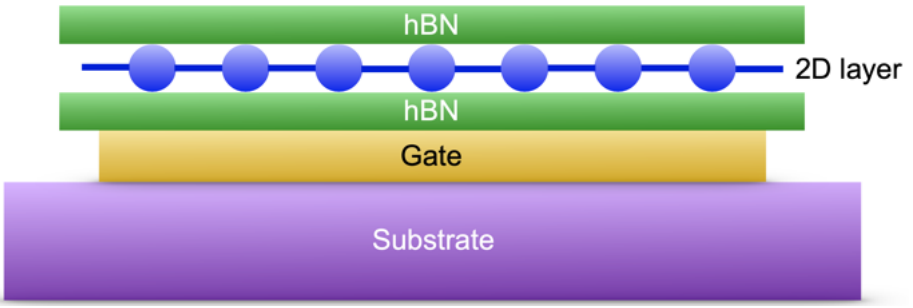

Fig. 1.1: Schematics of a typical hBN/graphene/hBN vdW heterostructures in which the 2D layer i.e. graphene is sandwiched between two hBN layers and the carrier density is tuned by the bottom metal gate.

(typically SiO_2) and boosts the mobility of graphene by order of magnitudes. This allows us to fabricate high quality devices that were only achievable by suspended graphene in vacuum [22, 23], which is far less versatile than the hBN encapsulated devices.

Besides the encapsulation, another interesting use of the vdW heterostructure is to combine a more conducting layer such as graphene or $NbSe_2$ with a less conducting material such as WSe_2 to make electrical contacts to WSe_2. Due to the large band gap of TMDCs, direct contact with metal creates a Schottky barrier and results into a very high contact resistance. This problem is often alleviated by first contacting the semiconductor with a graphene layer, and then contact to the graphene using metals [24].

After many years of intensive research, graphene field should logically reach a more mature stage. However, the possibility of combining graphene with other 2D crystals has expanded this field dramatically, well beyond simple graphene or 2D MoS_2. The interest in vdW heterostructures is growing as quickly as interest in graphene did couple of decades ago. As the technology of making vdW heterostructures moves from its humble beginnings, increasingly sophisticated devices and materials should become available to more and more research groups. This is likely to cause a snowball effect because, with so many 2D crystals, sequences and parameters to consider, the choice of possible vdW structures is limited only by our imagination. Even with the 2D components that have been shown to be stable, it will take time and effort to explore the huge parameter space. The decades of research

on semiconductor heterostructures and devices may serve as a guide to judge the probable longevity of research on vdW materials, beyond simple graphene.

When monolayer materials are vertically stacked, new properties only emerge if a sufficiently strong interlayer coupling is formed, which facilitates the hopping of electrons and redistribution of charge between the layers. More specifically, when the interlayer coupling is sharply reduced or severed, each layer becomes more independent, behaving similar to its monolayer configuration. Conversely, when the interlayer coupling is made strong, each layer's independence is reduced, and a superlattice forms that induces new properties. Stated simply, the interlayer coupling can facilitate the emergence of a new long-range periodicity, unique band structure, and dramatically new properties. One of the important parameter that gives rise to new properties in a heterostructure is the twist angle between two layers. The twist angle has a strong dependence on the interlayer coupling and band reconstructions. We will explore this parameter in the next section of this chapter.

1.3 Twistronics - A new degree of freedom

As discussed in the last section, vdW heterostructures opened up a new path in the materials science research. There exists an analogy between the vdW heterostructures and Lego to highlight the versatility of such heterostructures [16, 25]. However, a key ingredient is missing in this analogy, the twisting degree of freedom in vdW heterostructures. The relative lattice orientation between the 2D materials in a vdW heterostructure, or the twist angle θ, is arbitrary and can be precisely controlled during the fabrication of such heterostructures. This scenario is very different than other semiconducting systems, such as, GaAs, AlGaAs etc.

This unique twisting degree of freedom brings unprecedented richness into vdW heterostructures. Twisting two 2D materials can significantly modify the band structure and electronic interactions at low energies, especially when the twist angle is small but nonzero. This emerging field of twistronics - a term coined to refer to the study of effect of twist angle on electronic properties - has been the recent

hot-spot of the entire condensed matter physics community since the discovery of superconductivity in twisted bilayer graphene [26, 27].

The moiré pattern, a long range modulation of atomic density appears as a result of twisting two lattices with respect to each other. This has been shown in Figure 1.2. The moiré pattern originates from the spatial interference of two periodic lattices that are misaligned. Since most 2D materials have a hexagonal lattice (graphene, hBN, most TMDs, $NbSe_2$, etc.) or a distorted form of the hexagonal lattice (1-T' phases of TMDs), we shall here focus on lattices with hexagonal symmetry. In the next section, we will pick the simplest hexagonal lattice, graphene and briefly discuss the twisted graphene system.

1.3.1 Graphene

The easiest way to understand the periodicity of the moiré pattern is to look at the two periodic lattices in the frequency or reciprocal space. This is a central concept in solid state physics. The reciprocal lattice of a hexagonal lattice is a triangular lattice.

If a is the distance between nearest neighbors, the primitive lattice vectors can be chosen to be,

$$\vec{a_1} = \frac{a}{2}(3, \sqrt{3}), \quad \vec{a_2} = \frac{a}{2}(3, -\sqrt{3}) \tag{1.1}$$

The reciprocal lattice vectors are given by, b_1, b_2 with,

$$\vec{b_1} = \frac{2\pi}{3a}(1, \sqrt{3}), \quad \vec{b_2} = \frac{2\pi}{3a}(1, -\sqrt{3}) \tag{1.2}$$

The moiré pattern is determined by the shortest wave vectors that connects the reciprocal vectors of the different layers. While the detailed math of the explanation of such phenomena can be found in the literature, the moiré pattern can be understood as a real space counterpart of the acoustic beating phenomenon, where the sum of two sinusoidal sound waves with different frequencies f_1, f_2 can be decomposed as the product of a sinusoidal function of the mean frequency $(f_1 + f_2)/2$ and an envelope sinusoidal function with the difference frequency $(f_1 - f_2)/2$ (frequency of the beating is twice of this, thus $(f_1 - f_2)$). Analogously, the envelope wavevector of the moiré pattern is determined by the difference between the underlying wave vectors.

Let us consider the concrete example shown in Figure 1.2. In the real space, the moiré pattern is somewhat complicated to understand.

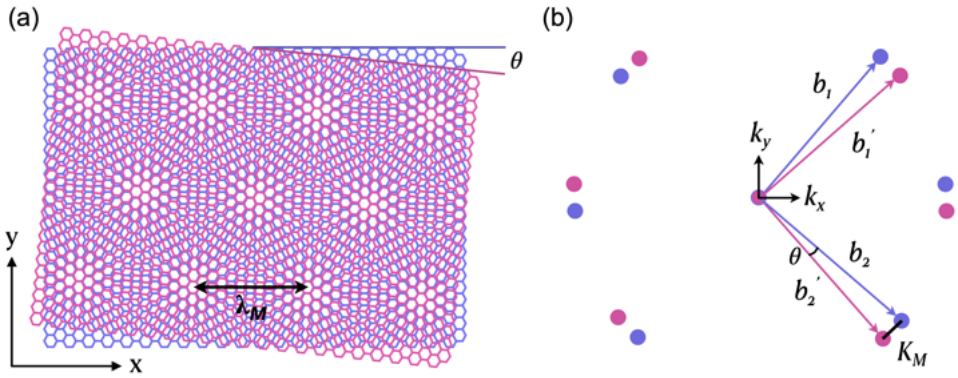

Fig. 1.2: Schematics of a moiré pattern generated by two hexagonal lattices. **(a)** Moiré pattern generated from the twisting of two hexagonal lattices by an angle θ in real space. **(b)** The reciprocal lattice points of the twisted moiré system in the first Brillouin zone.

However, in the reciprocal space the picture is much clearer, the two sets of reciprocal lattice points are simply rotated by the same angle θ with respect to the origin. From this picture, we can see that the smallest wave vector difference between the two sets of reciprocal lattice vectors is given by,

$$\Delta k = b_1 - b_1{}' \tag{1.3}$$

$$K_M = |\Delta k| = |b_1| \cdot 2\sin\theta/2 \tag{1.4}$$

Here K_M is the moiré wave vector. This defines the moiré length scale in the long range. From the relation between the real space and reciprocal space, we can define the moiré wavelength in the real space, which is given by,

$$\lambda_M = \frac{2\pi}{\sin(\pi/3)K_M} \tag{1.5}$$

Here λ_M is the moiré wave length of the superlattice unit cell. It can be simplified as,

$$\lambda_M = \frac{a}{2\sin(\theta/2)} \tag{1.6}$$

For very small twist angle $\theta \leq 1$, which is actually more interesting case as we will see later, we can simply write the moiré wavelength as,

$$\lambda_M \approx \frac{a}{\theta} \tag{1.7}$$

From the above equation, we can note couple of important points,

For two hexagonal lattices with the same lattice period a, the moiré wave length is inversely proportional to the twist angle (θ). Therefore, an arbitrarily large or small moiré structure can be achieved by changing the twist angle between two layers.

The number of encompassed unit cell in a moiré unit cell scales as θ^{-2}, which is of the order of 10^4 atoms for twist angles $\sim 1^\circ$. This poses a significant difficulty to the theoretical modelling of moiré systems at small twist angles. As we will see in Chapter 2, the tight-binding model is the most practical representation of the electronic band calculation in condensed matter physics. However, continuum model and effective model can also be constructed to capture the salient features of the moiré superlattice single particle bands. The area of the moiré unit cell is given by,

$$A_M = \lambda_M^2 \cos(\pi/3) = \frac{\sqrt{3}}{2}\lambda_M^2 \tag{1.8}$$

This area will be discussed and used in Chapter 2 in more detail for the calculation of the band structure of twisted bilayer graphene.

In this section we have introduced the moiré system very briefly and we will discuss the graphene moiré system specifically in details in the next Chapter.

1.3.2 Advantages over other correlated systems

One of the main characteristics of the twisted bilayer graphene, while rotated close to the magic angle is the formation of electronic flat band and observation of correlated phenomena in the system. People have observed many of these phenomena in other system as well. Correlated insulators, superconductors, magnetism, quantum anomalous Hall effect (QHE) etc. have been observed in multiple quantum materials before [28–30]. However, there are few advantages of studying these in twisted bilayer graphene compared to other systems, such as:

1. The carrier density of cuprates (BSCCO, YBCO) are much higher than graphene and it is not possible to tune the carrier density of these systems by applying a gate voltage. To study the full

phase space of these unconventional superconductors, one need multiple devices with different doping at the time of their growth [31]. On the other hand, twisted bilayer graphene is gate tunable and the complete phase space can be explored in a single device, just by applying the gate voltage to the system and changing its carrier density.

2. Graphene is the hexagonal honeycomb lattice, made of carbon atoms. This is very stable in the ambient condition compared to many pnictides and cuprates [32]. It is easier to fabricate these devices and measure them due to the better stability.

3. Due to the structural simplicity, twisted bilayer graphene is easier to study theoretically compared to cuprates and other heavy fermion systems.

4. It is reasonable to expect that several other typical condensed matter phases, from multiferroics to quantum spin liquids, might, one day, be realized in these moiré materials. Moreover, several new moiré systems have appeared, including double twisted bilayer graphene, twisted monolayer-bilayer graphene and twisted transition metal dichalcogenides (TMDs), leading to the emergence of the field of moiré quantum matter [33].

1.4 Outline of the thesis

In this introductory chapter, we have discussed a brief overview of 2D materials and van der Waals heterostructure followed by the hexagonal twisted moiré superlattice.

Chapter 2 discusses the theoretical basics of twisted bilayer graphene system. It starts with the band structure of graphene and bilayer graphene. Then it introduces a twist angle in the Hamiltonian and calculates the band structure of twisted bilayer graphene. The band structure is calculated by both tight binding model and continuum model. Finally, it discusses a very specific scenario when the twist angle is close to magic angle ($\theta = 1.1^{\circ}$).

In Chapter 3, we describes all the experimental methods that have been used in this thesis. The fabrication process of devices has been discussed in great detail. Also, the measurement steps and the cryogenic systems have been presented in this chapter.

Chapter 4 deals with the observation of Chern insulator in magic angle twisted bilayer graphene devices (MATBG) [34]. We start with the basic theoretical description of Chern insulators. Later in this chapter we represent our experimental data, which clearly shows the Chern insulators inside the flat band of MATBG pointing to the interaction of the charge carriers.

Chapter 5 portraits the Hofstadter spectrum of MATBG upto a very high magnetic field $B = 31$ T. The Hofstadter spectrum of the flat band with topological aspects and with interaction has been described for the first time here. This study clearly demonstrates the re-entrant correlated insulator and Fermi surface reconstruction at different integer fillings of the flat band at one magnetic flux quantum per moiré unit cell (Φ_0) [35].

Although the flat bands in MATBG hosts a lot of correlated phenomena at different carrier density, the high energy dispersive bands are also quite interesting and important to this system. Chapter 6 deals with the electronic properties of higher energy bands in MATBG which are Rashba-like. From the magnetotransport behavior, we have calculated a parameter free corrugation factor which puts a constraints on the Bistritzer-MacDonald Hamiltonian. From this, experimentally for the first time, we have verified the band structure of higher energy bands in MATBG [34]. We also discuss the high magnetic field Hofstadter spectrum of these dispersive bands and compare the emergent Landau levels with the theoretically predicted levels [35].

In Chapter 7, we discuss the effect of electrostatic screening on the correlated phenomena in MATBG. We change the distance between the metal screening layer and the twisted bilayer graphene by changing the thickness of the bottom hBN layer and study the temperature dependence of the phase space of three MATBG devices with slightly different twist angles to compare the existence of correlated insulators and superconductors in these devices [36]. This also helps us to understand the ongoing competition between different ground states of the flat band in MATBG.

Chapter 8 deals with one of the very important phases in correlated systems, which is strange metallicity. We study the temperature dependence of the resistivity in great detail for multiple devices with twist angle both near magic angle and far away from magic angle. This study discusses the existence of a strange metal phase in the devices close to magic angle inside the flat band [37]. This clearly shows a

non-Fermi liquid behaviour of the system and helps us to understand the microscopic mechanism of the electronic phases in MATBG.

Finally, in Chapter 9, we summarize the results discussed in different chapters and also give a future outlooks of the projects that have been carried out in this thesis.

Chapter 2

Theoretical Background

In this chapter, we will review the basic physics in twistronics systems and introduce the formulation necessary for understanding the band structure of moiré superlattices, in particular twisted bilayer graphene. Although chemically these superlattices are quite simple, often consisting of only one type of atoms (i.e. carbon), to understand their single-particle band structures is not a simple matter and requires quite involved calculations. Here, we will discuss in detail the issue of degeneracy and band counting in twisted moiré superlattices, which often causes quite some confusion.

The theories discussed in this chapter are all single particle physics, meaning that the Coulomb repulsion and exchange between the electrons, whether short ranged or long ranged, is neglected. This single particle physics have been quite well understood, at least in a semi-quantitative level. On the other hand, the phenomena that are discussed in the later chapters, which results from the single-particle flat bands in these twisted structures, are much less clearly understood, and the precise origins of those phenomena are still under debate.

We will start with the band structure of graphene followed by the band structure of Bernal stacked bilayer graphene. And then we will see how a twist angle in bilayer graphene changes its band structure. We will calculate the band structure of twisted bilayer graphene by tight-binding model and as well as continuum model. In the next section the specific case of the magic angle twisted bilayer graphene will be discussed where an electronically flat band is formed giving rise to the correlation in the system.

2.1 Band structure of graphene

Let us begin with the single-particle band structure of monolayer graphene. Graphene has a two dimensional honeycomb lattice of carbon atoms. The unit cell of graphene has two equivalent carbon atoms at the A and B sites, as shown in Figure 2.1**(a)**. Each carbon atom in this lattice assumes a sp^2 hybridization. The three in-plane orbits bond with adjacent atoms to form strong σ-bonds, while the electrons in the p_z orbit can hop in the entire plane through the π-bonds. The valence electronic bands of graphene has primarily p_z character, and we shall only consider them in the following [15].

If we only consider the nearest hopping, i.e. from A site to the adjacent B site and vice versa, the tight-binding Hamiltonian in the second-quantized form can be written as,

$$H = t \sum_{i,j=\langle i \rangle} a_i^\dagger b_j + h.c. \tag{2.1}$$

Here, a_i, $a_i^\dagger$, b_i, $b_i^\dagger$ are the annihilation and creation operators on the A and B sublattices respectively. t is the nearest hopping energy ($t \approx -2.7$ eV). The diagonalization of this tight-binding Hamiltonian is achieved by transforming the operators to the k-space,

$$a_i = \sum_k e^{ik \cdot r_{i,A}} a_k \quad b_i = \sum_k e^{ik \cdot r_{i,B}} b_k \tag{2.2}$$

The Hamiltonian can be written in the block-diagonal form as,

$$H = \sum_k h(k) = \sum_k f(k) a_k^\dagger b_k + h.c. \tag{2.3}$$

where $f(k) = \sum_{j=1}^{3} \exp ik \cdot \delta_j$ sums over all three possible hopping paths from B site to adjacent A sites. The eigenvalues of this block-diagonal Hamiltonian are,

$$E_\pm(k) = \pm |f(k)| \tag{2.4}$$

This energy dispersion is plotted in Figure 2.1**(c)**. As can be seen in the plot, the two bands touch at the K and K' corners of the first Brillouin zone, which are called the Dirac point of graphene. If we expand the Hamiltonian near one of the two corners (or valleys), we

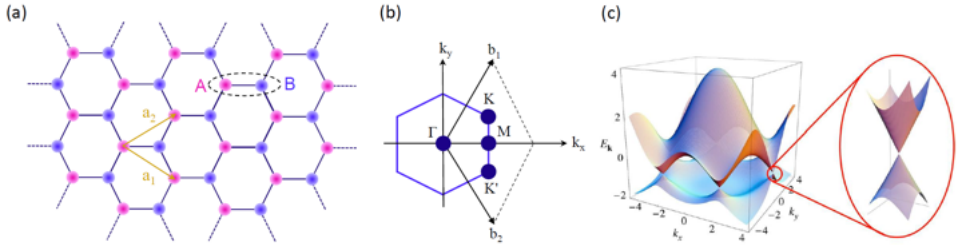

Fig. 2.1: Atomic structure of monolayer graphene. **(a)** Atomic structure of the honeycomb lattice in real space. A and B sublattices are marked in corresponding colours. Two lattice vectors are also shown here. **(b)** 1st BZ in the reciprocal space with corresponding reciprocal vectors (b_1, b_2) and two nonequivalent corners K and K'. **(c)** Electronic band structure of graphene. Zoomed in part shows the Dirac point.

obtain a massless Dirac Hamiltonian that describes a two-level system with inversion symmetry. For example, near the K valley we have,

$$h_K(q) = h(K+q) \approx \hbar v_F \begin{bmatrix} 0 & q_x - iq_y \\ q_x + iq_y & 0 \end{bmatrix} = \hbar v_F \sigma \cdot q \qquad (2.5)$$

Here we have represented the states on the two sublattices A and B in a two component spinor form, and $v_F = 3ta/2$ is the effective Fermi velocity in graphene.

Although we only considered the nearest-neighbor hopping, it can be shown that the massless Dirac points are protected against gap opening even if higher order hopping terms are considered. In fact, the gapless nature at the Dirac points are protected by a combination of C_2 and $\mathcal{T}$ symmetry of the lattice, where C_2 is the 2D spatial inversion operator that takes $(x, y) \to (-x, -y)$ and $\mathcal{T}$ is the time reversal operator.

A gapped Dirac point must have a mass term $m\sigma_z$ in their Hamiltonian (appended to Equation 2.5). While $\mathcal{T}$ demands that $m(K) = m(K')$, inversion symmetry on the other hand demands that $m(K) = -m(K')$. Therefore, when both symmetries are present, m must be zero for both valleys [38]. This symmetry argument naturally explains why graphene is a semimetal with Dirac electrons, while other 2D materials such as hBN and TMDCs are insulators or semiconductors. Having different atoms on A and B sites automatically breaks the C_2 inversion symmetry, and endows a mass term to the Dirac Hamiltonian.

One could also break the time-reversal symmetry instead of breaking the inversion symmetry to obtain gapped Dirac points, which is shown in the celebrated Haldane model [39].

In this symmetry analysis, we are relying on the fact that both C_2 and $\mathcal{T}$ takes the momentum k to $-k$ (not q), and thus K valley to K' valley. In most cases, the inter-valley hopping in graphene is negligible (conservation of valley charge). Thus, it is also useful to discuss the protection of a single Dirac point at either K or K' valley, using the reduced momentum $q = k - K$ or $q' = k - K'$. In this context within the same valley, the symmetry operations C_2 or $\mathcal{T}$ do not make sense anymore, since they map between different valleys. Instead, composite operation $C_2\mathcal{T}$ is a valid operation that takes to itself. Indeed, the Hamiltonian in Equation 2.5 is invariant under this composite operation,

$$C_2\mathcal{T}h_K(q)\mathcal{T}^{-1}C_2^{-1} = C_2\hbar v_F \begin{bmatrix} 0 & q_x + iq_y \\ q_x - iq_y & 0 \end{bmatrix} C_2^{-1} \tag{2.6}$$

$$C_2\mathcal{T}h_K(q)\mathcal{T}^{-1}C_2^{-1} = \hbar v_F \begin{bmatrix} 0 & q_x + iq_y \\ q_x - iq_y & 0 \end{bmatrix} \tag{2.7}$$

$$C_2\mathcal{T}h_K(q)\mathcal{T}^{-1}C_2^{-1} = h_K(q) \tag{2.8}$$

where $\mathcal{T}$ conjugates the Hamiltonian (we do not consider spin here), while C_2 switches its two rows and columns. This composite operation acts to forbid the gapping term $m\sigma_z$, because this term is not invariant under the $C_2\mathcal{T}$ operation,

$$C_2\mathcal{T}\sigma_z\mathcal{T}^{-1}C_2^{-1} = -\sigma_z \tag{2.9}$$

The $C_2\mathcal{T}$ symmetry within each valley requires both C_2 and $\mathcal{T}$ to be a symmetry of the Hamiltonian. However, when the $C_2\mathcal{T}$ symmetry is broken, it could be either C_2 or $\mathcal{T}$ (or both) that is broken, but which one it is, cannot be determined without extra information. In other words, if one only knows that the Dirac point at one valley is gapped by a mass term m, without knowing the mass term at the other valley is $-m$, or m, it cannot be determined whether C_2 or $\mathcal{T}$ is the remaining symmetry. The $C_2\mathcal{T}$ symmetry is thus crucial for understanding the formation of gaps at the Dirac points, not only in graphene but in general in hexagonal lattice systems, including twisted bilayer graphene.

2.2 Band structure of bilayer graphene

The case of bilayer graphene is interesting in its own right, since with two graphene monolayers that are weakly coupled by interlayer carbon hopping, it is intermediate between graphene monolayers and bulk graphite.

The tight-binding description can be adapted to study the bilayer electronic structure assuming specific stacking of the two layers with respect to each other (which controls the interlayer hopping terms). Considering the so called AB stacking of the two layers (which is the three-dimensional graphite stacking), the low energy, long-wavelength electronic structure of bilayer graphene is described by the following energy dispersion relation [40, 41],

$$E_{\pm}(q) = \left(V^2 + \hbar^2 v_F^2 q^2 + t_\perp^2/2 \pm (4V^2\hbar^2 v_F^2 q^2 + t_\perp^2 \hbar^2 v_F^2 q^2 + t_\perp^4/4)^{1/2}\right)^{1/2} \tag{2.10}$$

where $t_\perp$ is the effective interlayer hopping energy and t, v_F are the intralayer hopping energy and graphene Fermi velocity for the monolayer case. We note that $t_\perp(\approx 0.4)$ eV $< t(\approx 2.5)$ eV, and we have neglected several additional interlayer hopping terms since they are much smaller than $t_\perp$. The quantity V with dimensions of energy appearing in Equation 2.10 for bilayer dispersion corresponds to the possibility of a real shift, e.g. by an applied external electric field perpendicular to the layers, z direction in the electro-chemical potential between the two layers, which would translate into an effective band-gap opening near the Dirac point.

Expanding equation 2.10 to leading order in momentum and assuming $V << t$, we get,

$$E_{\pm}(q) = \pm\left(V - 2\hbar^2 v_F^2 q^2 V/t_\perp^2 + \hbar^4 v_F^4 q^4/(2t_\perp^2 V)\right) \tag{2.11}$$

We conclude the following,

1. For $V \neq 0$, bilayer graphene has a minimum band gap of $\Delta = 2V - 4V^3/t_\perp^2$ at $q = \sqrt{2}V/\hbar v_F$.

2. For $V = 0$, bilayer graphene is a gapless semiconductor with a parabolic band dispersion relation.

What about the chirality for bilayer graphene? Although the bilayer energy dispersion is non-Dirac-like and parabolic, the system is still chiral due to the A/B sublattice symmetry giving rise to the conserved pseudospin quantum index. The possible existence of an external bias-induced band gap and the parabolic dispersion at long wavelength distinguish bilayer graphene from monolayer graphene, with both possessing chiral carrier dynamics.

2.3 Bilayer graphene : with a twist

Now we can proceed to understand the electronic structure of twisted bilayer graphene (TBG). However, if we look closely at the atomic structure, the first issue we run into is the commensuration. Strictly speaking, a band theory can only be defined for systems with exact translational symmetry, and then the Bloch theorem will guarantee that all eigenstates of the system can be labeled by a momentum k. However, when two lattices are stacked together with a relative twist, there is in general no strict spatial periodicity in the resulting structure, except for some special cases. In the special cases when there is such a periodicity, this composite structure is commensurate, otherwise it is incommensurate. Examples of the two situations are shown in Figure 2.2. The commensurate structures can only be satisfied at a countable set of twist angles. An exact band theory can be constructed only for these commensurate twist angles. However, approximate band structures for incommensurate structures at small angles can still be constructed using the continuum model.

Let us denote the unit cell vectors of the two layers of graphene by a_1, a_2, and a_1', a_2' respectively. One of the common notation system to describe a commensurate structure is to use a pair of positive integers (n, m) such that the lattice vectors of the superlattice can be written as [42–44],

$$\begin{aligned} A_1 &= na_1 + ma_2 \\ A_2 &= -ma_1 + (n+m)a_2 \end{aligned}$$

Figure 2.2**(a)** shows the commensurate structure corresponding to $(m = 3, n = 2)$. The commensurate twist angle [45] corresponding to structure (m, n) is given by,

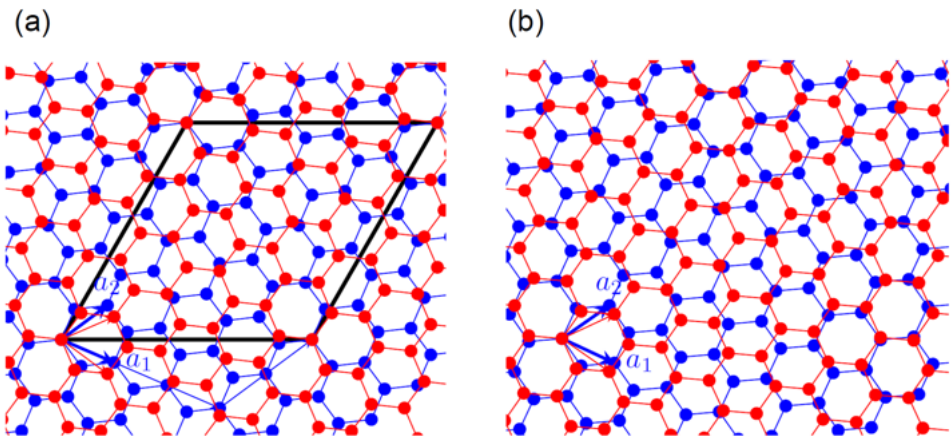

Fig. 2.2: **(a)** Commensurate and **(b)** incommensurate twisted bilayer graphene structures. In **(a)**, the large black parallelogram denotes the unit cell of the superlattice

$$cos\theta(m,n) = \frac{n^2 + 4nm + m^2}{2(n^2 + nm + m^2)} \tag{2.12}$$

In particular, the structures that are denoted by $(m, m-1)$ ($r = 1$ structures) have special importance, since the unit cell of these structures contains exactly one moiré spot. These structures are the most fundamental moiré structures, while the $r > 1$ structures are have larger unit cells than the moiré spots and are of higher order. It has been shown that at small angles, there is no fundamental difference between the electronic band structures of $r = 1$ and $r > 1$ structures, the latter is essentially the former folded into a smaller Brillouin zone. However, structures with different r have distinct spatial symmetry, [46] which have subtle effects on the topological properties of the bands in twisted bilayer graphene and caused some debate from a mathematical perspective. From the experimental side, it has been shown that realistic devices have non-negligible variation in local twist angles [47], and therefore these subtle differences might not be observable in the experiments.

To understand the experiment relevant physics in twist bilayer graphene at small twist angles $\theta << 1$ rad, it is therefore sufficient to focus only on $r = 1$ structures. Furthermore, the tight-binding

band structure of the $r = 1$ structures interpolates smoothly with the calculation from the continuum model. It should be noted that $r > 1$ structures are valid representation of TBG as well [48].

However, it must be kept in mind that equivalence of $r = 1$ and $r >1$ structures is only valid for small angles. TBG does not have strict inversion symmetry, and structures with different r have different chirality. It has been experimentally shown that this chirality can result in circular dichroism at large twist angles [49].

In the next sections, we will summarize the major approaches of theoretical models that describe the single particle band structure of twisted bilayer graphene. We will start with the most detailed but least intuitive models and later on describe the simpler and more approximate models. The main goal of these models is to obtain the eigenvalues $E_{nv}(q)$ and eigenstates $\Psi_{nv}(q)$ of the single particle Hamiltonian H, which should satisfy the single particle Schrödinger equation,

$$H\Psi_{nv}(q) = E_{nv}(q)\Psi_{nv}(q) \tag{2.13}$$

where q is the reduced momentum in the mini Brillouin zone (MBZ). Here, n and v are the band index (1, 2, 3, . . .) and valley index ($\pm$) respectively. Due to time reversal symmetry, it is guaranteed that $E_{n+}(q) = E_{n-}(-q)$. In the models where only one valley is considered we will simply use E_n and Ψ_n to denote the corresponding energies and eigenstates.

2.3.1 Tight binding model of twisted bilayer graphene

In a commensurate TBG structure labeled by (n, m), the total number of atoms in the moiré unit cell is equal to,

$$N = 4(n^2 + m^2 + nm) \tag{2.14}$$

Therefore, for structures larger than (11, 10) (twist angles smaller than $\sim 3^\circ$), the number of atoms quickly reaches 10^3 to 10^4, exceeding the capability of typical ab-initio methods, such as density functional theory (DFT), which can typically only deal with less than a few hundred of atoms per unit cell. Some approximations must be made to make this problem tractable.

The tight-binding model of twisted bilayer graphene builds upon the same p_z-orbital of the sp^2-hybridized carbon atoms that we used to model monolayer graphene, but in addition considers the σ-bonds between the layers, which is typically called the interlayer hybridization.

The tight-binding Hamiltonian is written as,

$$H_{TBG} = \sum_{i,j} w(i,j) c_i^\dagger c_j + h.c. \tag{2.15}$$

Here, i, j label the atoms in the unit cell and $w(i,j)$ is the generic site-dependent hopping parameter. In the literature the following approximation is typically used to describe the hopping energies, which is referred to as the Slater-Koster rule [44, 50],

$$w(i,j) = V_\pi \left[1 - \left(\frac{d_{i,j} \cdot \hat{z}}{d_{i,j}}\right)^2\right] e^{-\frac{d_{i,j}-a_0}{\delta}} + V_\sigma \left(\frac{d_{i,j} \cdot \hat{z}}{d_{i,j}}\right)^2 e^{-\frac{d_{i,j}-d_0}{\delta}} \tag{2.16}$$

where $d_{i,j} = r_i - r_j$ is the displacement vector between atom i and j, and d_{ij} is its magnitude. Here, V_π and V_σ are π-bond and σ-bond hopping parameters respectively. a_0 and d_0 are the interatomic spacing and interlayer spacing respectively, and δ is a hopping decay parameter. For two atoms directly on top of each other, $d_{i,j} = (0, 0, d_0)$ and $w(i,j)$ reduces to V_σ which represents a σ-bond. On the other hand, for two atoms side-by-side separated by $a_0, w(i,j) = V_\pi$, representing a π-bond. In general, the hopping direction is somewhere in between these two limits. A slightly different set of parameters could also be obtained from fitting the DFT calculations at small scales.

To solve the energy spectrum of the Hamiltonian Equation 2.15, we again transform it to the k-space,

$$c_i = \sum_k e^{ik\cdot(r_i+R)} c_k^I \tag{2.17}$$

where R is the origin of the unit cell containing the i-th atom, r_i is the displacement of i-th atom within the unit cell, and index $I = 1, \ldots N$ is the index of i-th atom within the unit cell. We end up with N operators in the form of c_k^I, each representing a plane wave with wavevector k that only have amplitude on the I-th atom in the unit

cell. With this transformation, the Hamiltonian is block-diagonalized in k as,

$$H_TBG = \sum_k h_TBG(k) = \sum_k \sum_{I,J} h_{I,J}(k) c_k^{I,\dagger} c_k^J + h.c. \tag{2.18}$$

where $h_{IJ}(k)$ is the hopping matrix that has the form of,

$$h_{IJ}(k) = \sum_R w(r_I + R, r_J) e^i k \cdot (r_I + R - r_J) \tag{2.19}$$

The summation runs over all possible paths of hopping from J-th atom into I-th atom, which could be in a different unit cell than J, labeled by its origin R. This $N \times N$ matrix is numerically evaluated and diagonalized to obtain the N eigenvalues and eigenvectors for each momentum k. The eigenvectors have the form of $(a_1, ..., a_N)^T$, where a_I is the amplitude of the plane wave on I-th atom. The single-particle band structure of TBG is now completely solved, having N mini-bands in the MBZ. For angles $\theta \sim 1°$, $N \sim 10^4$ and it is still quite computational demanding to diagonalize such non-sparse matrix for many k points in the MBZ, but is definitely tractable within the capability of cluster servers.

Figure 2.3 shows the tight-binding band structure of TBG for a few twist angles. We can compare them with the non-hybridized case and one can immediately notice a few crucial differences:

1. At all twist angles, the Dirac cones remain at K_S and K'_S, i.e. the interlayer hybridization does not gap out the Dirac points.

2. The intersections between the Dirac cones, which along M_S and Γ_S gap out due to the interlayer hybridization.

3. The slope of the energy versus the momentum $dE(q)/dq$ at the Dirac points, also known as the Fermi velocity v_F, is reduced (renormalized) due to the interlayer hybridization, compared to the bare graphene Fermi velocity of $v_F \approx 8.7 \times 10^5 ms^{-1}$. This renormalization is stronger as the twist angle θ is reduced. In fact, whether the Fermi velocity is significantly reduced or not is the criteria for smallness of twist angles in TBG, which is typically considered to be around $\theta \sim 3°$.

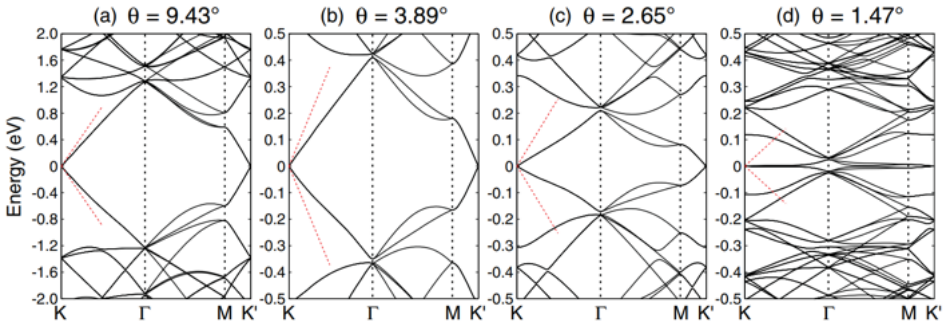

Fig. 2.3: Band structure of TBG calculated using the tight-binding model for four commensurate angles that correspond to (3, 4), (8, 9), (12, 13), and (22, 23). Adapted from Ref. [42]. The red dashed lines denote the slope of the original graphene Fermi velocity, $v_F \approx 8.7 \times 10^5 ms^{-1}$

As we have discussed in Section 2.1, the protection of the Dirac points in graphene requires both C_2 rotational symmetry and the time reversal symmetry $\mathcal{T}$. While the latter is usually not broken without any ferromagnetic ordering, C_2 symmetry is not a perfect symmetry of TBG. Depending on the twist center to be on a hexagonal site, an atom site, or a general location, the TBG lattice belongs to either D_6, D_3 or C_1 (no rotational symmetry) group. The C_2 symmetry is absent in both of the latter two cases. Therefore, mathematically speaking, the Dirac cones in TBG do not need to be gapless, except in the commensurate structures with D_6 symmetry.

However this is at odd with our observation, down to an energy scale of $\sim \mu$eV. It turns out that in TBG with such a big unit cell, the approximate symmetries also play an important role in protecting certain aspects of the band structure. Although C_2 is in general microscopically broken, it is broken so weakly that for the analysis of low-energy band structure in the MBZ the C_2 and thus D_6 symmetry is still approximately present, for small twist angles $\theta << 1$ rad. Therefore, the Dirac cones are approximately gapless. Another interpretation of this effect is that the breaking of the strict C_2 symmetry occurs on a large length scale $\sim a/\theta$ while a scattering process with a length scale $\sim a$ is necessary to introduce coupling between the K and K' Dirac cones to gap them out. Since the intervalley scattering process decays exponentially with $1/\theta$, the Dirac cones are exponentially better protected as $\theta \to 0$. Again, both arguments only works

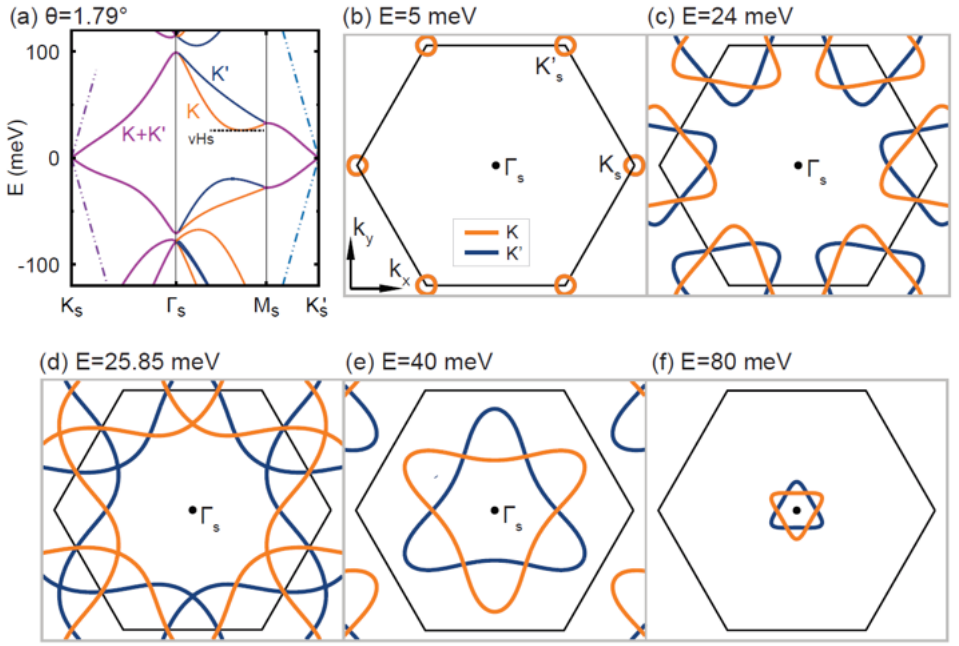

Fig. 2.4: **(a)** Band structure of $\theta = 1.8°$ TBG calculated with an ab initio tight-binding model. Dashed lines denote the original graphene Fermi velocity. **(b-f)** Fermi contours at five different energy cuts $E =$ 5 meV, 24 meV, 25.85 meV, 40 meV and 80 meV. Among them, **(d)** E = 25.85 meV corresponds to the van Hove singularity, which is labeled in **(a)**. The hexagons in **(b-f)** denote the MBZ of the superlattice

for small twist angles $\theta << 1$ rad. For large twist angles close to 30°, it is in principle possible to obtain gapped Dirac points, for an infinitely large and perfect structure [51].

In particular, it is of our interest to take a closer look at the band structures of small twist angles. Figure shows the bands and Fermi contours of $\theta = 1.79°$ TBG, corresponding to a (19, 18) commensurate structure. From these calculations, we can identify the following key features of the lowest mini-bands in TBG, which holds true above $\sim 1°$ unless specified. For clarity, we focus on the positive energy side, the bands are roughly symmetric on the negative side.

1. Right above the Dirac energy (Figure 2.4(b)), there are approximately round Fermi pockets (electron-like, meaning they expand as energy is increased) at K_S and K'_S points. There are in total 8 Fermi pockets in the MBZ from valley, spin, and layer/corner.

2. As the energy rises (Figure 2.4(c)), the trigonal warping of the Fermi pockets becomes pronounced. At each corner, the Fermi pockets from K and K' pockets form a crossing David star without hybridizing, due to the approximate valley conservation.

3. At a particular energy, the Fermi contours from K_S and K'_S points meet along the $\Gamma_S - M_S$ direction (Figure 2.4(d)). This point is also known as the van Hove singularity (vHs), and is labeled in Figure 2.4(a). It is a saddle point, as the energy rises, the Fermi contour converge towards it in one direction and expands away from it in a perpendicular direction. The density of states shows a logarithmic divergence at this energy.

4. Past the vHs, the energy contours merge into a different David star, now centered at Γ_S (Figure 2.4(e, f)). The Fermi contour is now hole-like, its size shrinks as energy is increased. Note that the degeneracy of the Fermi contour is now 4 - from valley and spin. This is not surprising. The layer/corner counting is invalid, because the Fermi contour is now centered on Γ_S instead of K_S or K'_S.

5. For most angles within 1° to 2°, there is a band gap above the lowest mini-bands of TBG [52] For larger twist angles, it is a semimetalic band edge. The bands above this band edge are often referred to as the remote bands. These remote bands usually contain multiple Fermi pockets with different degeneracies and sizes, which make their fermiology quite complicated.

In summary, the tight-binding model accurately describes the single-particle band structure of a small-angle TBG. All these single-particle band effects predicted by the tight-binding bands have been observed in the experiment. The drawback of the tight-binding model is that fewer insights can be obtained on how the electronic states couple and hybridize within the moiré unit cell, and that it cannot deal with arbitrary incommensurate twist angles. These issues are what motivate the development of the continuum model, as will be discussed next.

2.3.2 Continuum model

The tight-binding model is built upon an atomic basis. In the continuum model, however, our starting point is the other extreme - we

start with plane waves that propagate in each layer, and couple them by the interlayer hybridization. As explained before, the plane waves near the K-valley that can propagate in each layer must obey the Dirac equation (at low-energies),

$$h_K(q)\psi_K(q) = E_K(q)\Psi_K(q) \tag{2.20}$$

which gives rise to,

$$h_K(q) = \hbar v_F(q) \begin{pmatrix} 0 & e^{-i\theta_q} \\ e^{i\theta_q} & 0 \end{pmatrix} \tag{2.21}$$

where θ_q =1/ tan(q_y/q_x) the argument of the q vector. For two graphene layers that are at twist angles $-\theta/2$ and $\theta/2$ respectively, the Hamiltonian in each of the layers rotates as,

$$h_K^1(q) = \hbar v_F(q) \begin{pmatrix} 0 & e^{-i(\theta_q+\theta/2)} \\ e^{i(\theta_q+\theta/2)} & 0 \end{pmatrix} \tag{2.22}$$

and

$$h_K^2(q) = \hbar v_F(q) \begin{pmatrix} 0 & e^{-i(\theta_q-\theta/2)} \\ e^{i(\theta_q-\theta/2)} & 0 \end{pmatrix} \tag{2.23}$$

where we have defined the rotated Pauli matrices $\sigma^{\pm\theta/2}$. Note that these Hamiltonians act on a two-component spinor $(\alpha_q, \beta_q)^T$ which represent the amplitudes of the plane waves that resides on sublattice A and B, respectively, of a particular layer. We want to now introduce the interlayer coupling which hybridizes different states from layer 1 and layer 2. However, before going into that let me use a simpler 1D model to provide some more insight about the interlayer process and its momentum transfer.

To capture the interlayer hybridizing physics, we first consider a double-chain model as shown in Figure . We set the hopping within each chain to be t, and the inter-chain hopping to be w or $-w$. We consider two cases: the w's are all the same, or have alternating signs. In both cases, we define the unit cell to contain two atoms along the direction of the ladder, having in total four atom sites per unit cell. The unit cell has a length of 2 (we set $a = 1$), and the first BZ defined as $[-\pi/2, \pi/2]$. We can write down the hopping matrix for each k as,

$$h_{dc}(k) = \begin{pmatrix} 0 & tcoska & w & 0 \\ tcoska & 0 & 0 & \pm w \\ w & 0 & 0 & tcoska \\ 0 & \pm w & tcoska & 0 \end{pmatrix} \tag{2.24}$$

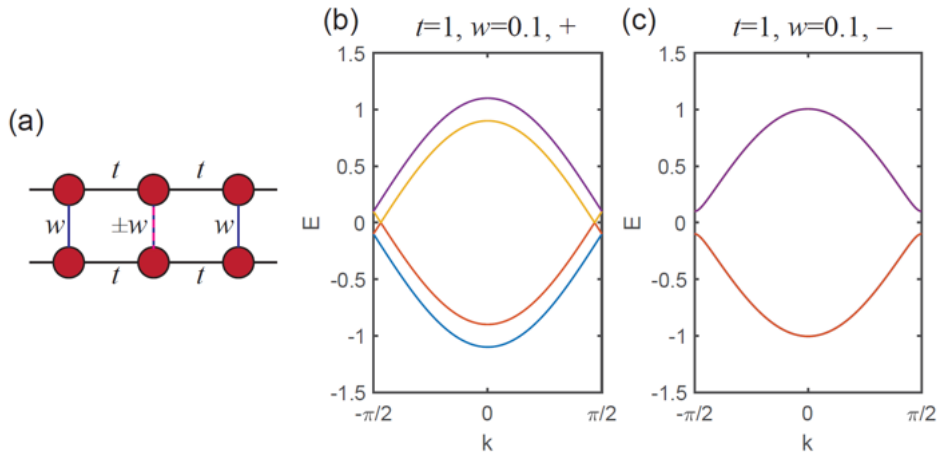

Fig. 2.5: A double-chain toy model. **(a)** Two chains with intra-chain hopping t are coupled by alternating inter-chain hopping w and $\pm w$. **(b)** When the inter-chain hopping is homogeneous (+), states with the same momentum are hybridized, and the originally degenerate bands are offset by $\pm w$. **(c)** When the inter-chain hopping is alternating (-), states with momentum that differ by $q = \pm\pi$ are hybridized. This results in new band gaps at momentum $q = \pm\pi/2$.

This Hamiltonian can be diagonalized to obtain the eigenvalues $E_n(k), n$ =1, 2, 3, 4, shown in Figure for the $+w$ and $-w$ cases respectively. When $w = 0$, there are two sets of degenerate bands, from the two decoupled chains. We can see that, when w is turned on, the two chains are hybridized in two completely different ways, depending on the pattern of the inter-chain hopping parameter. The happens due to the momentum transfer of the inter-chain hopping parameters.

2.4 Flat bands in twisted bilayer graphene

The only physical parameters in the continuum model are the graphene bare Fermi velocity v_F, the interlayer potential w, and the twist angle θ. It can be shown that there is in fact only one dimensionless parameter that controls the entirety of TBG physics, namely the ratio,

$$\alpha = \frac{w}{\hbar v_{F0} \left|K\right| \theta} \tag{2.25}$$

This is the ratio between the interlayer hopping amplitude w and

the energy at which the Dirac cone from layer 1 intersects with the cone from layer 2, $\hbar v_{F0} |K_D| /2$, up to a numerical factor. These are the two most important energy scales in TBG.

For small α (corresponding to large twist angles), $w << \hbar v_F |K| \theta$. The Dirac cones from the two layers are far apart in the momentum space such that their low-energy dispersion is minimally affected. When α is increased (twist angle decreases), we observe a dramatic reduction of the Fermi velocity v_F, in both the tight-binding and continuum models. This effect, which is called renormalization of the Fermi velocity, is a direct result of the interlayer hybridization. It has been shown that to the lowest order, the dependence of α and v_F is,

$$v_F(\alpha) = v_{F0} \frac{1 - 3\alpha^2}{1 + 6\alpha^2} \tag{2.26}$$

where v_{F0} is the monolayer graphene Fermi velocity.

For small α, $v_F \approx v_F 0(1 - 9\alpha^2)$ is a correction to the original Fermi velocity. However, for non-small α there is a zero in $v_F(\alpha), v_F = 0$ when $\alpha = 1/\sqrt{3}$, or when,

$$\theta = \frac{\sqrt{3} w}{\hbar v_{F0} |K|} \equiv \theta_M^1 \tag{2.27}$$

We have defined the first magic angle θ_M^1. Putting in the values for graphene, $v_{F0} = 8.7 \times 10^5 m s^{-1}$, $|K| = 4\pi/3a$, $a = 0.246$ nm, and $w \approx 0.11$ eV, we find the first magic angle to be,

$$\theta_M^1 \approx 1.1^\circ \tag{2.28}$$

The electronic band structure at the first magic angle θ_M^1 is extremely interesting. The Fermi velocity at the MBZ corners K_S and $K_S^{'}$ goes to zero, which means that the states surrounding these points have close to zero energy. How about the other parts of the lowest mini-band, such as Γ_S or M_S? Apart from the zero Fermi velocity, the entire band is flattened to be in a small energy window of a couple of meV. In other words, the interlayer hybridization in TBG creates flat bands near the charge neutrality point when $\theta \approx \theta_M^1$.

To conclude this section, it should be mentioned that the appearance of magic angles is a peculiar phenomena in twisted system with Dirac fermions, which requires the approximate $C_2\mathcal{T}$ symmetry to be present. However, it is not a requirement for the appearance of flat

bands. Besides TBG, moiré flat bands and associated phenomena have so far been generalized to twisted bilayer-bilayer graphene (TBBG), twisted WSe2, ABC trilayer graphene/hBN, TMD hetero-bilayers, and so on. The physics of twistronics (band folding and interlayer hybridization) applies similarly to these systems. Nevertheless, none of these systems are theoretically expected or shown to possess a magic angle in the same sense as in TBG - zero Fermi velocity and perfectly flat bands in a certain limit. In the latter systems, the flatness of the bands is a combined result of reduction of Brillouin zone, and deformation of the bands due to interlayer hybridization.

Chapter 3

Experimental Methods

The formation of the electronic flat band in twisted bilayer graphene, when rotated by an angle $\theta_M = 1.1°$, has been discussed in the last chapter. People have studied different moiré superlattice systems over the past few years and significant effort has been expended on improving the sample quality and complexity. Over the course of my PhD, we have also tried to improve the device quality by refining different fabrication steps that we will elaborate here. In the first section, we will describe the stacking process starting from the mechanical exfoliation. Then we will explain different nanofabrication processes of these devices.

While making the twisted bilayer graphene devices, a big number of devices are discarded since they are not twisted by the magic angle. In order to screen the best quality devices for further measurements, we have also developed several experimental set-ups which include a vacuum probe station, and a variable temperature insert (VTI) which can reach a base temperature of 1.5 K in a few hours. We will also describe these systems in detail.

We will also discuss a few specific topics about the instrumentation and measurement techniques relevant for the generic transport measurement at low temperature.

We have explored the twisted bilayer graphene system at an unprecedentedly high magnetic field in my PhD. Although the measurement techniques were similar in this study, special attention was given to remove any current loop susceptible to induce noise at high magnetic field (upto $B = 36$ T). In the last section of this chapter, we will discuss the high magnetic field measurement set up.

3.1 Fabrication Process

Nanofabrication of van der Waals heterostructures was introduced in 2013 in graphene-hBN heterostructures [53] and this fabrication process is widely used now to make one dimensional electrical contacts. The basic structure of an encapsulated twisted bilayer graphene device consists of hBN/bilayer graphene/hBN/graphite layers stacked together. The nanofabrication of such devices involves four main steps.

Exfoliation

We exfoliate several 2D materials, such as graphene, hBN etc on Si/SiO_2 substrates. After exfoliation, we examine these flakes with optical microscope and atomic force microscope (AFM) in order to choose the appropriate candidate for the next process.

Stamps

Stamps are made of Polydimethylsiloxane (PDMS) and a thin layer of polymer which helps us to stack multiple 2D layers. Making a clean and stable stamp is the key to getting good stacks. We will describe the stamp making process in detail in the next section.

Vertical assembly

In this step, we combine the exfoliated 2D flakes by using the stamps and make the desired heterostructures.

Clean room processing

We use electron beam lithography (EBL), reactive ion etching (RIE), and metal evaporators to make gates and electrical contacts to the bilayer graphene heterostructures.

Each of these steps is crucial in order to fabricate the clean devices. Although these steps are being used by all the experimental groups working on 2D materials, the design of the stacking technique is unique to each group and determines the device quality. So, in this chapter we will discuss our device fabrication techniques in detail.

3.1.1 Exfoliation

As mentioned in chapter 1, most of the two dimensional materials available right now are mainly bonded by the van der Waals (vdW) force in the bulk. The van der Waals force is much weaker than the chemical bonds which bind the atoms in a molecule. Therefore, each layer can be easily peeled off from the bulk using various physical or chemical methods.

In 2004, Andre Geim and Konstantin Novoselov introduced an incredibly simple yet elegant method to mechanically exfoliate two dimensional layers from its bulk material by using a scotch tape [4]. This method has yielded the highest quality flakes so far and is being used in fundamental research of 2D materials for last eighteen years.

Here we will describe this method in detail and discuss the crucial steps for the exfoliation of graphene and hBN flakes.

- **Cleaning of the Substrate**

  First, we use a diamond cutter to cut the Si/SiO_2 chips with the dimension of 5 cm $\times$ 5 cm. Then we clean these chips with O_2 plasma for the exfoliation of graphene and hBN with the following recipe.

  O_2 plasma : Power - 100 Watt, Flow rate - 50 SCCM, time - 3 mins. However, for the exfoliation of graphite, which will be used as the gate, we do not plasma clean the chips before exfoliation. We will explain the reason later.

- **Peeling the bulk material**

  In this process, we start by sticking a small amount of bulk crystal to a piece of scotch tape. After that we fold the tape 5-6 times to thin the material. In this step we try to ensure an uniform layer of material on the tape. However, we restrict the number of folding to 5/6 to make sure that the crystal does not become too small during this process.

- **Attaching the tape on the substrate**

  Next, we bring the tape very close to the clean substrates which have been placed on top of a glass slide. After attaching the tape to the top of the substrate, we press them gently in order to increase the adhesion between the flakes and the substrates.

- **Heating the substrates**

  Once we have pressed the tape gently on the substrates, we follow two different steps for graphene and graphite or hBN. For both graphene and graphite, we place the glass slides along with the substrates and tape on a hot plate at 110° for 5-7 mins. For hBN exfoliation, we do not heat the substrates.

- **Peeling the tape from substrates**

  Finally, we peel off the tape very slowly from the substrates leaving some freshly cleaved material on the substrates.

This procedure creates various flakes with different sizes and thickness on the substrate. Proper combination of the number of folds, pressure and heating results in the exfoliation of clean, monolayer graphene. The size of the monolayer graphene varies widely depending on the parameters described here. However, we generally choose the layers with a size of $\sim 50 \times 50$ μm for a clean stacking process.

Choice of flakes

It is important to start with a set of good flakes to have a successful stack in the end. In the very first step, we use an optical microscope to identify the size, thickness and quality of the flakes. This becomes possible because of the optical property of the 2D materials. Absorption of incident light by any two dimensional metal or semimetal depends on the thickness of that material while deposited on a substrate. For semiconductors and insulators incident light is refracted differently depending on the thickness. Monolayer graphene absorbs 2.3% of the incident light and the absorption increases linearly with the increasing number of layers. People have shown in the past, both using theoretical models and from experimental data, that monolayer graphene has the highest visibility on 290 nm SiO_2 layer on Si substrate (Si/SiO_2) [54–56]. However, hBN layers have better visibility on 90 nm SiO_2 substrate [57]. In all of our experiments we have exfoliated graphene and graphite on 290 nm Si/SiO_2 substrate and hBN on 90 nm Si/SiO_2 substrate. Although optical contrast is typically enough to distinguish between monolayer, bilayer or thicker graphite, we also used Raman spectroscopy to verify the number of graphene layers. Once it is verified by Raman spectroscopy we set a particular colour contrast in the microscope software to identify the monolayer graphene subsequently.

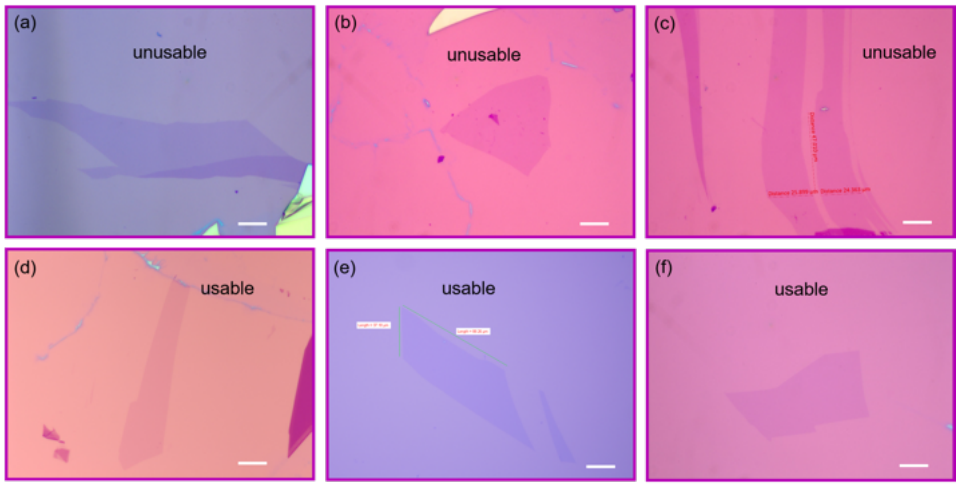

Fig. 3.1: Optical image of graphene flakes. **(a)**, **(b)**, **(c)** correspond to the type of flakes that we discard. **(d)**, **(e)**, **(f)** correspond to the type of flakes that we typically choose for the stacking. All the images are taken with 50X optical zoom. The scale bar in all the figures is 10 μm.

We also use atomic force microscopy (AFM) to characterize the quality and thickness of hBN flakes [58]. The AFM is a scanning probe microscope in which the topographical image of the sample surface is measured based on the interactions between a silicon tip and the sample surface. It is an ideal tool for creating 3D images on 2D materials. The 3D measurements directly image wrinkles, folds, cracks and any other surface defect of the 2D flakes.

Optical images

In this section, we will give some examples of flakes that we choose to stack. As mentioned earlier, we use the optical microscope to search for monolayer graphene once the colour contrast is set by the Raman spectroscopy. In Figure 3.1 we have shown a few images of the graphene flakes. We generally try to discard the flakes which are attached to thicker graphite layer as shown in Figure 3.1 **(a)**, or which have some tape residues as shown in Figure 3.1 **(b)** or very big flakes (larger than 60 - 70 μm) as shown in Figure 3.1 **(c)**. All these types of flakes create some difficulty during stacking. It is very hard to pick up a flake which is either bigger or attached to another thicker layer, as generally, they

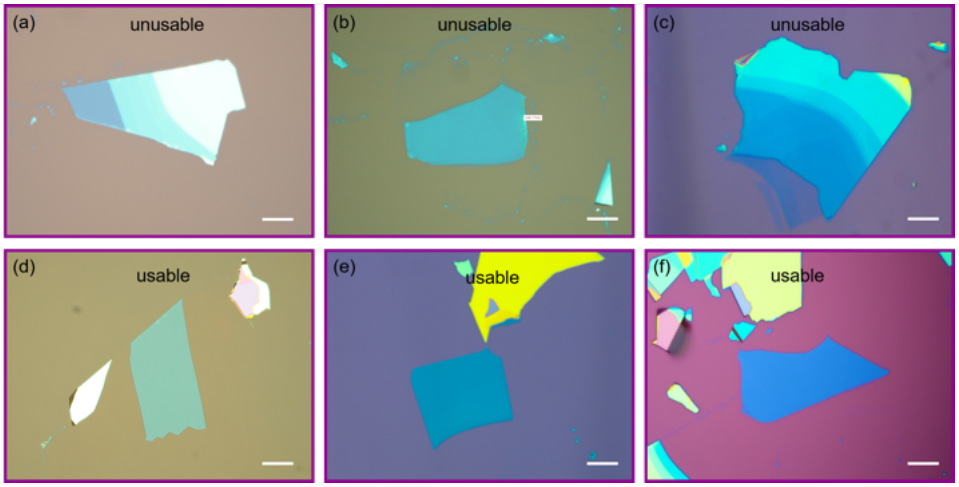

Fig. 3.2: Optical images of hBN flakes. **(a)**, **(b)**, **(c)** correspond to the type of flakes that we discard. **(d)**, **(e)**, **(f)** correspond to the type of flakes that we typically choose for the stacking. All the images are taken with 50X optical zoom. The scale bar is 10 μm in all the figures.

have a higher adhesion with the substrate. And any residue on the flake creates bubbles while picking up more layers. Naturally, it is undesirable to start with these types of flakes.

However, finding a good hBN flake is more difficult than finding a good graphene flake. Since we neither plasma clean nor heat the substrate for exfoliating hBN, it is harder to get clean, uniform flakes. Generally we use 10 - 20 nm thick hBN flakes for normal twisted bilayer graphene stacks. It is advantageous to use the hBN flakes which have thickness in this range for multiple reasons. Firstly, any non-uniformity or dirt on top of these flakes is very easy to detect by optical contrast. Secondly, these flakes are more flexible than thicker (50 - 60 nm) flakes, and thus there is lower probability of their cracking during the stacking process. We avoid those flakes which have any small crack or dirt on it. In the stacking process, it is preferable to use the top hBN which has at least one almost straight edge. We will explain the reason later in the vertical assembly section. In Figure 3.2 we have shown images of few hBN flakes to describe the type of flakes we immediately discard by optical microscope. The flake in Figure 3.2**(a)** is nonuniform and contains three different regions with different thickness. These types of flakes hinder the stacking process. Figure 3.2**(b)** shows a flake which

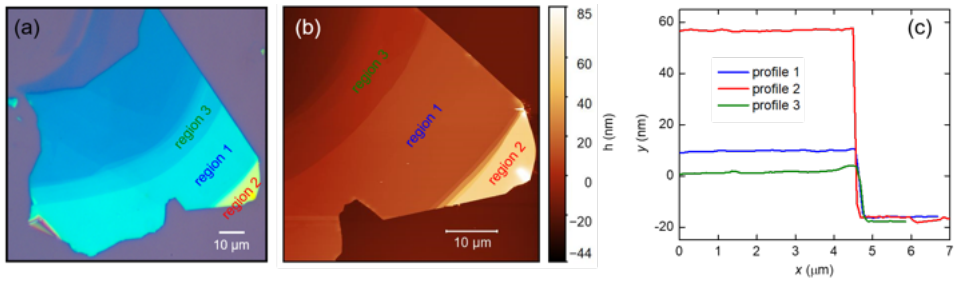

Fig. 3.3: AFM image of a hBN flake. **(a)** shows an optical image of a hBN flake on 290nm SiO_2 substrate. **(b)** represents an AFM image of the same flake with the colour scale and three regions marked separately. **(c)** shows the thickness of these three different regions marked in **(a)** and **(b)**.

is uniform but contains residues on top which is clearly visible in the optical image. We avoid these types of flakes as they introduce bubbles during the stacking. Figure 3.2**(c)** is another example of an inhomogeneous flake that we discard. On the other hand, Figure 3.2**(d)**, **(e)**, **(f)** represent a set of clean, homogeneous, isolated flakes that have been used in our devices.

AFM images

Experimentally, it is challenging to obtain clean 2D flakes of hBN and graphene. The scotch tape leaves adhesive residues on the exfoliated flakes. This residue is sometimes invisible under the optical microscope. Hence, to further characterize the flakes we perform AFM on hBN and graphite flakes. In the beginning we measured the thickness of a set of hBN flakes and fixed the colour contrast in the optical microscope for the specific thickness. This helps us to quickly detect the type of flake we want in the next step. In Figure 3.3 we have shown an optical image a hBN flake with different thicknesses in **(a)**. Three different regions are marked in corresponding colours. Figure 3.3**(b)** represents the AFM image. In 3.3**(c)** we can clearly see the height of three different regions. The yellowish region (region 2) has the maximum height (60 nm), green region (region 1) has a height of 12 - 15 nm and blueish green region (region 3) corresponds to 6 - 7 nm. As the colour contrast becomes more blueish, the thickness reduces. From this study we gain an overall understanding of the thickness of hBN

flakes while searching.

In each batch of fabrication, we choose a set of flakes (around 6 - 7) sitting on separate Si/SiO_2 substrates. We always keep the exfoliated flakes in a vacuum desiccator and use these within 2 - 3 days. We have noticed that freshly exfoliated flakes are easier to pick up from the substrate without cracks or bubbles.

In the mechanical exfoliation process, the substrate is generally full of flakes and the desired flake is surrounded by other thick materials and tape residues. Presence of any thick material or dirt or dust disrupts the flow of the polymer that we use for stacking. Therefore it is necessary to clean the environment of the desired flake before starting to stack. We use an AFM tip attached on top of a glass slide/PDMS for this purpose. This trick uses the micro-manipulating stage to put the AFM tip in contact with the undesirable material or dirt on the substrate and then drag it further away from the desired flake leaving its environment clean.

3.1.2 Preparation of Stamps

After the exfoliation and selection of a set of good flakes, we make a PDMS (Polydimethylsiloxane) stamp to make the heterojunction. The stamp is a stack of transparent and sticky polymers that is used to make a 2D heterojunction. In the beginning of 2D heterojunction research people used only PDMS for the dry transfer technique [59, 60]. Later polypropylene carbonate (PPC) was widely used due to its better adhesive properties. However, recently, people have found that polycarbonate (PC) is a more suitable material for stacking multiple layers at a higher temperature. PC has its glass transition temperature at 120° C which makes it easier to operate at a higher temperature without making it fluid.

PC film

1. PC is soluble in Chloroform. We mix 5% by weight PC with chloroform and stir it overnight with a magnetic stirrer.

2. When the PC is completely dissolved in chloroform, we apply 10 drops of it on a very clean glass slide (cleaned with Acetone, IPA).

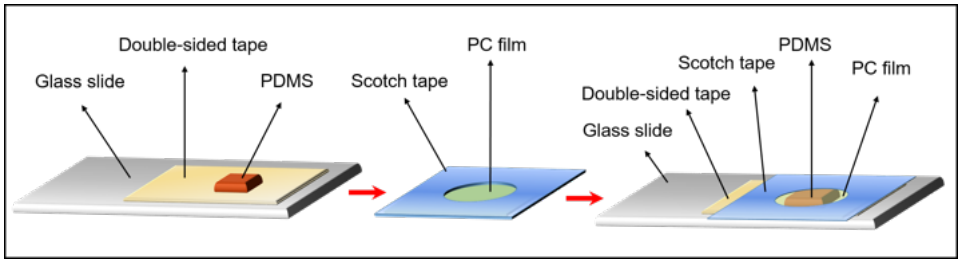

Fig. 3.4: PDMS/PC stamp for transferring.

3. We put another glass slide on top and quickly drag it along the surface making a thin film on top.

4. We place the glass slide on a hot plate at 90 - 95° C for 5 mins to completely dry the chloroform.

Stamps

The full stamp consists of several layers as illustrated in Figure 3.4.

1. First we take a clean glass slide and put a small piece of double sided tape cut with a sharp knife.

2. We use commercially bought 0.5 mm thick PDMS sheets from GelPack. We cut the PDMS in a small piece (1 mm × 1 mm) keeping the plastic cover on both sides. We remove the thick plastic cover and slowly place it on double-sided tape. While placing the PDMS on glass slide/double-sided tape, make sure there is no air bubble trapped in between. We then remove the thin plastic cover from the upper side of PDMS.

3. We take a small piece of scotch tape and make a small hole in the middle (2 - 3 mm diameter) either with a sharp knife or with a punching machine.

4. We cut a piece of (1 cm × 1 cm) PC film that has been made on the glass slide in the previous step with a very sharp knife. Make sure there is no wrinkle in the cut part. The PC film is generally a few μm thick.

5. The scotch tape with the hole is then placed on the PC film that has been cut and slowly peeled off from the glass slide. This gives

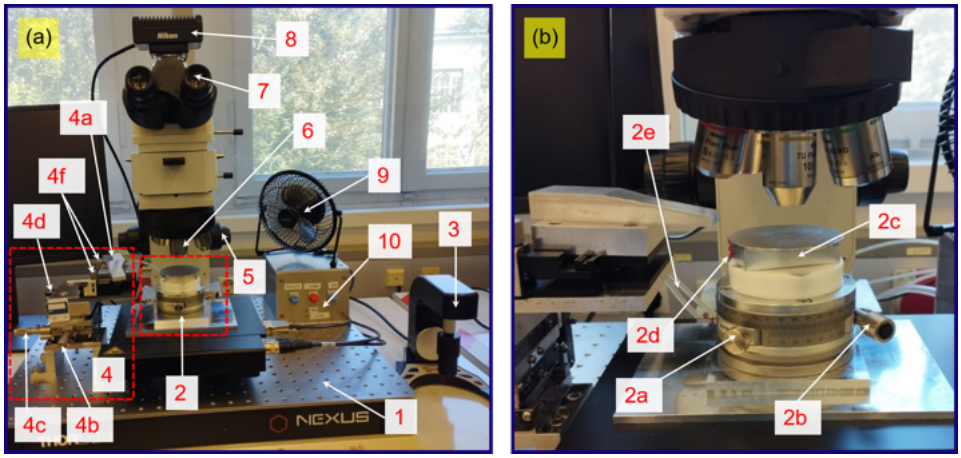

Fig. 3.5: Transfer stage. **(a)** Full transfer stage with all the different parts marked. **(b)** Zoomed-in picture of the sample stage with rotating plate screws marked.

us a free-standing PC film framed with a scotch tape as shown in Figure 3.4. Again, make sure that there is no folding in the free-standing film.

6. In the final step, the scotch tape with the PC film is placed on top of the PDMS. Make sure there is no air bubble trapped in between PDMS and PC film. In the end heat the full stamp at 90° for 5 mins.

The PDMS provides the necessary compressibility and the PC film provides the stickiness in order to pick up multiple 2D layers without folding, cracking or tearing.

3.1.3 Vertical Assembly

Vertical assembling of different 2D layers is done on a micro-manipulating stage, called transfer stage.

Transfer stage

We have built the full transfer stage in our lab with the different parts bought commercially. In Figure 3.5 we have shown the pictures of the full transfer stage that we use. The major components in this set-up are,

1. This is a heavy vibration reduction stage that we use to reduce any vibration that might come from the table during the stacking.

2. This is the sample stage which consists of several parts. Figure 3.5**(b)** shows a zoomed in picture of the sample stage. The parts are as follows:

   (2a) Coarse screw for the rotating stage. We use this to adjust the rotating scale before starting to stack.

   (2b) Fine screw for the rotating stage. We use this to rotate one flake w.r.t. other while stacking. We have a precision of 0.016° in this rotating stage.

   (2c) Sample plate with the heater and temperature sensor inside it. In the middle of the plate we have a small vacuum hole which is used to stick the substrate with the plate while picking up flakes from it.

   (2d) Shows the wiring for the heater and sensor.

   (2e) Vacuum lines attached to the sample stage and stamp holder (4a).

3. The X and Y manipulator of the sample stage is automated and controlled by the joystick shown here.

4. This compound part is used to manipulate the stamp. It consists of:

   (4a) The stamp leg holds the stamp. It has two vacuum lines to hold the glass slide of the stamp.

   (4b), (4c) X and Y axis manipulator of the stamp.

   (4d) Z axis manipulator for approaching, engaging and disengaging the stamp.

   (4f) Screws to tilt the stamp in X-Y and Z plane for a specific direction of approach.

5. Focusing knob used to change the focal plane by adjusting the height of the objective lens.

6. 4 different objective lenses.

7. Eye-piece.

8. Camera connected to the computer.

9. A small fan for the fast cooling of the sample stage.

10. Three knobs to change the vacuum for sample plate, stamp leg and stamp.

Next, we will describe the stacking process in detail.

Cut & stack process

This stacking process has been developed over the last 2 - 3 years in which we cut the monolayer graphene before starting to pick up other layers. Figure 3.6 illustrates the full stacking process step by step.

1. Before starting to pick up any layer, we first select the set of flakes that will be used in the stacking i.e. top hBN, graphene, bottom hBN and the bottom graphite. We make sure that the top hBN has atleast one straight edge.

2. Once we select the flakes, graphene is cut with an AFM tip. The size of each layer of cut graphene should match the size of top hBN. This helps us in pinning the graphene with hBN layer.

3. We place the substrate containing top hBN on sample stage and turn on the sample-stage vacuum. Then we attach the stamp with the stamp-leg by turning on the vacuum knob.

4. Then we navigate to the selected top hBN flake by using the joystick and make sure that the flake is in the centre of the focus of the eyepiece of our camera setup. At the same time we bring the PDMS/PC part in the centre and select a clean region in it. We align the top hBN with the clean region.

5. Next step is to increase the sample stage temperature to 90°. We bring the PDMS/PC very close to the sample by using the Z screw in the stamp manipulator. But the stamp should not touch the substrate yet.

6. We increase the temperature to 100°. Now, we slowly bring the stamp down and make a contact with the substrate. The first point of contact should be far from the selected flake.

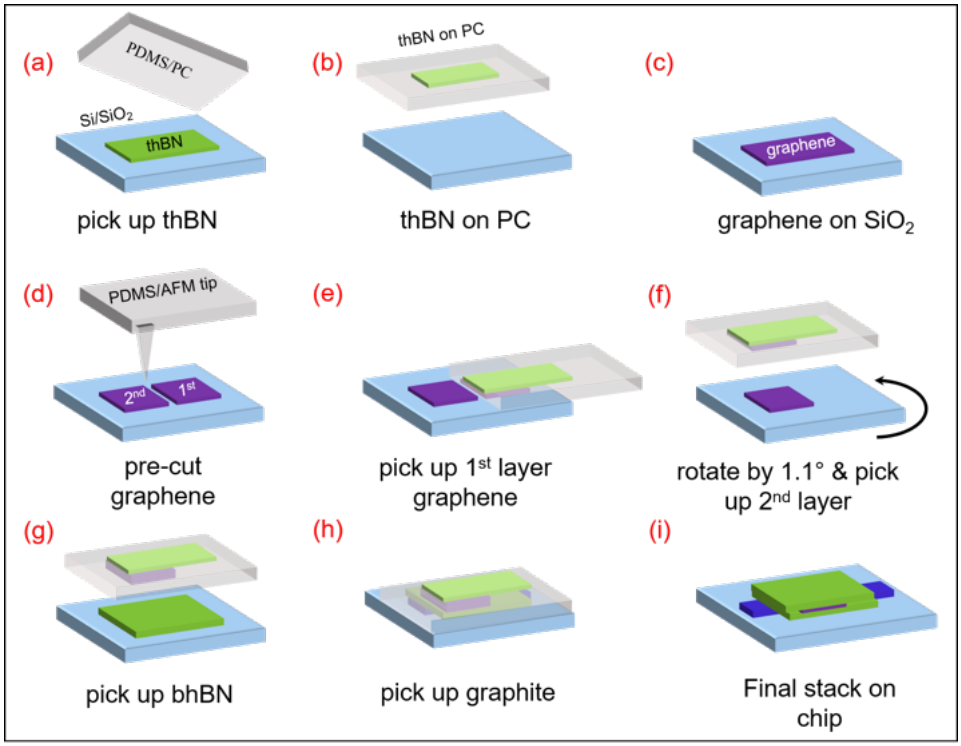

Fig. 3.6: Schematics of the stacking process. **(a)** Engaging the PDMS/PC stamp with top hBN on substrate. **(b)** Top hBN picked up on PC. **(c)** Selected graphene flake on substrate. **(d)** Cutting the monolayer graphene with AFM tip. **(e)** Making contact with the 1st graphene layer and picking up. **(f)** Rotating the 2nd layer of graphene by 1.1° and picking up. **(g)** Picking up the bottom hBN. **(h)** Picking up the graphite gate. **(i)** Depositing the final stack on substrate.

7. At this temperature PC has a very good stickiness. We increase the temperature to 110°. PC will start to flow as it is in fluid state, but we make sure that it does not touch the flake. However, the point of contact with the substrate should be close enough to see the optical fringes (as observed in Figure 3.8) near the flake.

8. Slowly we make the contact with the flake by using the Z-screw. In this step, we make sure that the fringes are moving smoothly and there is no sudden jump in the contacting surface. We let the fringes pass through the flake completely and wait for 2 - 3 mins.

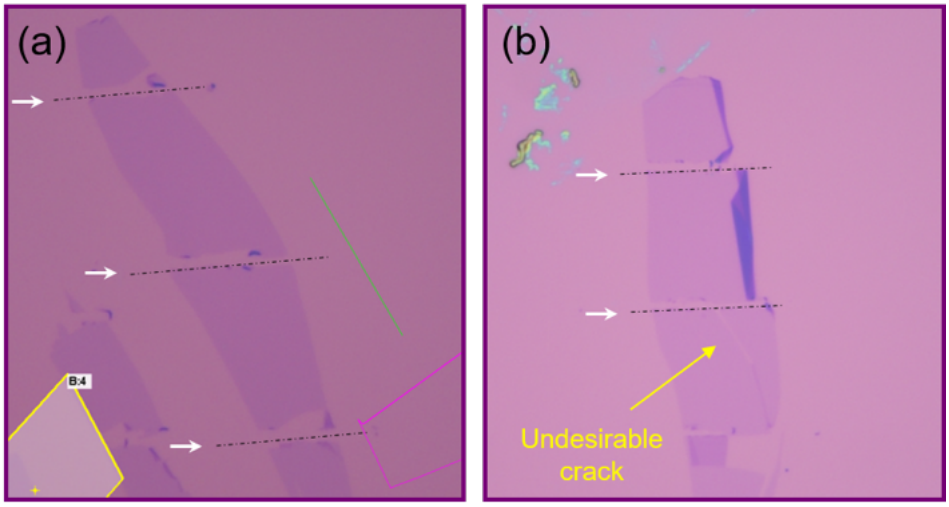

Fig. 3.7: Pre-cut graphene flakes. **(a)** A big graphene flake is cut in two pieces with AFM tip. **(b)** Graphene is cut in two pieces with undesirable crack and fold.

9. Now, we detach the PC from the substrate very slowly by moving the Z-screw backward.

10. Once the stamp is completely detached, we turn off the sample vacuum and change the sample. After placing the pre-cut graphene, we turn on the vacuum again.

11. We then align the graphene with the top hBN on PC and make sure that the straight edge of hBN is aligned properly with the graphene.

12. Next we bring down the stamp and make a contact with the substrate and let the PC flow until the optical fringes are visible near the flake.

13. At this stage, we make the fine alignment between the top hBN and graphene and make sure that the 1st graphene layer is properly framed with the hBN. Now we slowly make contact and cover the 1st layer completely. We do not let the PC touch the 2nd layer of graphene as it might dope the flake. Both 1st and 2nd layer of graphene used in the stacking process is cut from a single monolayer flake which we will discuss later.

14. We detach the PC from the substrate and rotate the sample stage by **1.1**° with the fine adjustment screw of the rotational stage.

15. We then align the 2nd layer of graphene with the top hBN/graphene on PC.

16. Again we make contact slowly with the 2nd layer and then detach the stamp from the PC. In all these steps we make sure that the contact is always very smooth.

17. We change the sample and place the bottom hBN on the sample stage.

18. Next we align the bottom hBN with the layers already on the PC. Both the graphene layers should be completely covered with the bottom hBN. We pick up this layer in the same way.

19. Next, we change the sample and place the graphite on top and repeat the same process to pick it up.

    Please note that, we maintain the temperature around 110-115° during the full stacking process to avoid any thermal relaxation of the metal plates. Next we deposit the full stack on a pre-patterned substrate which we will use to make electrical contacts later.

20. We place the pre-patterned substrate on the stage and turn on the vacuum. We increase the temperature to 140 - 145° and make contact with the PC far away from the stack.

21. Finally, we increase the temperature to 175° and let the PC flow on its own. Once the stack makes contact with the substrate, we leave it for 3-5 mins. Now slowly we raise the stamp by using the Z screw. First the PC will detach from the PDMS and as we continue raising it, the PC will start to detach from the glass slide as well. We use the X-Y screws to detach the PC film from the glass slide completely. Finally, we raise the stamp completely, leaving the PC and stack on the substrate.

22. To clean the PC on top of the stack, we place the substrate in chloroform for 5 mins followed by IPA for 5 mins and blow dry.

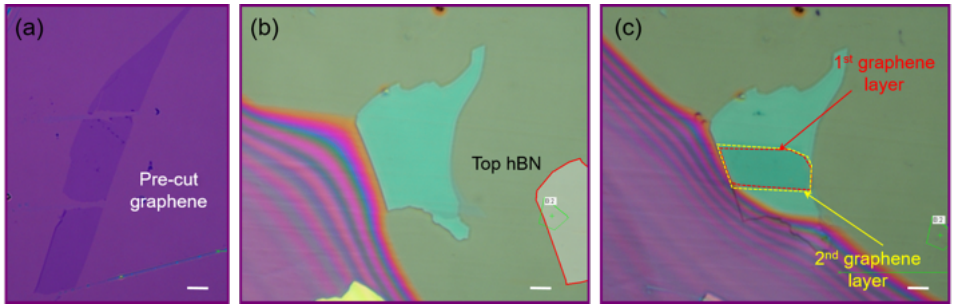

Fig. 3.8: Top hBN and graphene pick up. **(a)** A big graphene is cut in two pieces matching the size of the top hBN. **(b)** Picking up the top hBN. Colourful fringes show the evolution of the PC surface. **(c)** Top hBN along with the two layers of graphene picked up. Both of the graphene layers are attached with the edge of top hBN.

A few important points:

In Figure 3.7 we have shown two images of two graphene flakes. In the first image, we started with a bigger flake and cut it into two pieces matching with the width of the top hBN. The cuts are clean and there is no wrinkle or fold in the flake. However in the 2nd image we found some unexpected cracks and folding while cutting the flake. We immediately discard these types of flakes. This flake has a lot of strain, probably due to the inhomogeneous adhesion with the substrate and might relax to a different twist angle while stacking.

We try to cut the graphene so that the 1st layer of graphene is properly framed with the top hBN. This step helps us in reducing the probability of the relaxation of the twist angle. Figure 3.8 shows this scenario. After picking up, both the layers of graphene nicely touch the edge of the hBN as shown in Figure 3.8**(c)**.

We do AFM on the stack after cleaning the PC to choose a clean bubble free region to make the device channel.

3.1.4 Clean room fabrication

In the next step of the fabrication process we need to make electrical contacts with the graphene. This includes making electrodes and gates for measuring the quantum transport properties of twisted bilayer graphene as a function of carrier density. This involves several steps of lithography, etching and metal deposition in the clean room. The

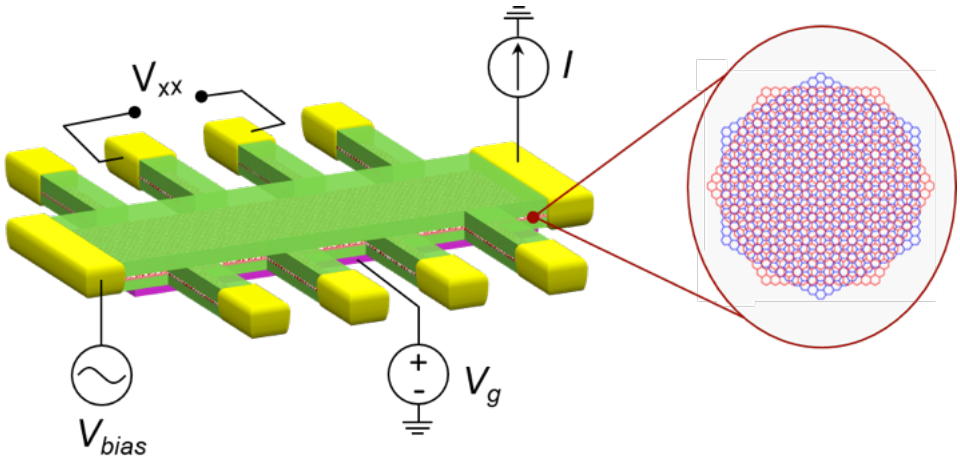

Fig. 3.9: Schematics of the device structure. Twisted bilayer graphene is sandwiched between two hBN layers shown in green colour. The stack is etched in Hall bar geometry and connected with gold (in yellow colour) showing the bias and gate voltage schematics. Zoomed-in part shows the moiré structure.

typical structure of our devices is illustrated in Figure 3.9. The most commonly used technique for contacting the encapsulated graphene device is the edge contact which was introduced by Cory Dean's group in 2013 [53]. The metal contact is fabricated by depositing evaporated metal along the etched 1D line in these encapsulated sandwiched devices. The major advantage of the edge contact device over the 2D top or bottom contact device is that the twisted graphene layers are fully covered with insulating hBN layers and are protected from any chemicals used during the fabrication process or charged puddles trapped in the substrate. Typical contact resistance of these devices ranges from 100 $\Omega\mu\text{m}^{-1}$ to 1000 $\Omega\mu\text{m}^{-1}$.

There are mainly three choices for the bottom gate: (i) Highly doped Si substrate with SiO_2 on top as the dielectric material. (ii) Metallic gate deposited by noble metal evaporation. (iii) 4 layers or thicker graphite. In all of our devices we have used thick (7 - 8 nm) graphite layers to electrostatically gate the devices. We have found that graphite gates have some advantages over the metallic gates. Firstly, it gives cleaner devices as this is a single step stacking process. Secondly, we can ensure that the gating is uniform and not hindered by any dirt on the gate.

After selecting the cleanest region with AFM, we make the design of the Hall bar in KLayout software to do the e-beam lithography. The details of the clean room processes are as follows:

1. Spin coat the substrate with PMMA 950A2 e-beam resist at a 4000 RPM speed for 60 sec followed by a baking at 150°C for 5 mins. This recipe gives a 270 nm thick PMMA layer.

2. Design the etch mask in the Hall bar geometry under e-beam lithography and develop the resist with MIBK:IPA (1:3) for 40 sec followed by IPA for 1 min.

3. The sample is then inserted in a reactive ion etcher (RIE). The typical etching recipe we use for etching away the hBN is a mixture of CHF_3 : O_2 in 10:1 ratio. This recipe also etches graphite with three times lower rate. In this step we etch the full stack all the way down to SiO_2. After the etching, the sample is cleaned with acetone and IPA.

4. After the etching mask has been defined, we design the electrodes in the KLayout software with the final images of the Hall bar structure.

5. Again spin coat PMMA with the same recipe followed by the baking at 150° for 5 mins.

6. Design the electrodes in EBL. In this step contacts for both Hall bar electrodes and gate electrodes are made.

7. Develop the resist with MIBK/IPA as mentioned before.

8. After developing the electrodes, place the sample in RIE to etch the top hBN using the same CHF_3 / O_2 recipe. This step is done to make sure that fresh graphene edges are exposed.

9. After the etching, immediately transfer the sample to the evaporator to avoid contamination of the freshly exposed graphene. We generally keep the sample under pumping overnight to make sure a pressure of $\sim 10^{-7}$ mbar is reached before deposition. We also refill our chromium crucible to make sure there is fresh chromium in the evaporator while making contact with graphene.

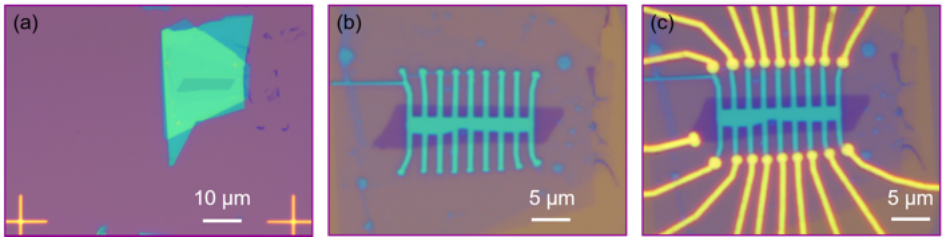

Fig. 3.10: Optical image of the device. **(a)** Optical image of a full stack deposited on a pre-patterned substrate. **(b)** Optical image of the Hall bar after etching rest of the stack in the 1st lithography process. **(c)** Optical image of the full device with all the contacts made with Cr/Au.

10. Next day, we evaporate chromium (Cr) and gold (Au) on the sample while rotating it at a tilted angle. The rotation is necessary to make sure that all the edges of the sample receive equal metal evaporation. 5/6 nm Cr is evaporated with e-beam evaporation at a rate 1 Å/sec rate. Then 50 nm of Au is deposited with thermal evaporation at a 1 Å/sec rate.

11. After evaporation the sample is placed in acetone. Keep it in acetone for several hours and once there are visible wrinkles in the metallic layer, spray some more acetone forcefully to properly lift off the undesirable metal. Check under microscope while keeping inside acetone and then finally blow dry.

At this point the device fabrication is finished. Figure 3.10 shows the optical image of a full device starting from the stack.

We have to be careful while designing the Hall bar when using the graphite local gate. The electrodes can never overlap with any part of the graphite. Also, make sure that there is no part of graphene is connected with the graphite at the point of metal deposition. Otherwise, it will result into a direct shortage between device and the gate. There is also a drawback of putting all the contacts outside of the graphite edge. There will always be some part of the Hall bar (0.5 - 1 μm), which can not be gated by the graphite. This region, not being gated with the graphite, becomes highly resistive at lower temperature and at high magnetic field making the four probe measurement difficult. To avoid this problem we use the silicon layer to apply a global gate. This helps to gate the graphene away from the CNP and reduce the

contact resistance.

After finishing the fabrication, we prepare the sample for measurement. In all of our measurement set up, we use the same 28-pin chip carrier. So, we cut the sample to fit inside the chip carrier and paste it with silver paste. And finally wire bond the device with the chip carrier for the measurement.

3.2 Measurement set-up

In this section we will describe different measurement set-ups that we have built during my PhD in order to better measure the electrical transport properties of twisted bilayer graphene devices. We have strategically developed different set-ups to systematically screen the device and finally measure the magic angle device in dilution fridge. This includes mainly three different measurement platforms,

1. Vacuum probe station : In this set up we measure the device at room temperature and under vacuum condition.

2. 1.5K cryostat : This is a dry cryogenic system to perform basic measurements with a base temperature of 1.5K.

3. Dilution fridge : All the final measurements are done in this system.

3.2.1 Vacuum Probe Station

We use the vacuum probe station to check the electrical connection of our devices at room temperature and at low pressure. After the fabrication of the MATBG devices, we check the electrical contacts of the electrodes in this station. We use a low pressure environment to make sure that we do not dope any impurity in graphene while gating the device at room temperature.

Figure 3.11 shows the images of our home-built vacuum probe station. It mainly has four different parts:

1. This is the main vacuum compartment of the set-up. It is made with several vacuum components which were commercially brought and assembled together.

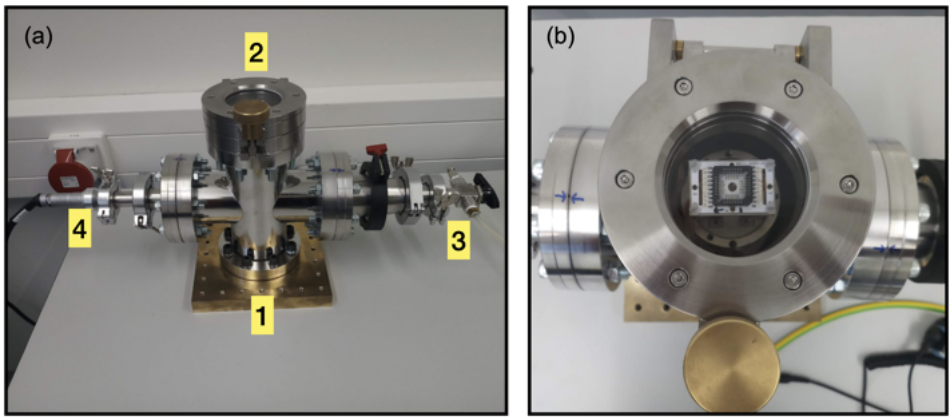

Fig. 3.11: Images of the vacuum probe station. **(a)** Picture of the complete vacuum station. **(b)** Zoomed-in picture of the sample holder.

2. This is the sample holder with a glass window. A zoomed-in picture of this part is shown in Figure 3.11**(b)**. We can load the sample through the glass window which can be opened and closed through a screw.

3. The vacuum line and the venting lines are connected through this region. There is a one way valve which allows us to make the vacuum inside the set-up or vent it in order to load or unload the sample.

4. Electrical connection to the sample. The electrical cable is connected through a Fischer connector with the sample wires. It finally connects a breakout box with the sample through which we perform the measurements.

We connect lock-in amplifier and voltage sourcemeter to measure the device in this set up. We check the electrical connections of all the electrodes by measuring their two-probe resistance. Additionally, we also measure the four-probe resistance of the device to have an idea of the twist angle of the device. Due to the hybridization of the electronic bands in MATBG, four probe resistance is two orders of magnitude higher than the non-twisted or low angle twisted device. We only proceed with those devices which have a four-probe resistance of $R_{xx} \sim 10 - 40$ kΩ.

3.2.2 Dilution Fridge

Near the magic angle, the flat bands of the twisted bilayer graphene systems have a very small energy scale ($\leq$ 10 meV). Hence measuring different phenomena in this system requires ultra-low temperature and this is achieved by using a dilution refrigerator where ^{3}He is pumped from a mixture of ^{3}He and ^{4}He to reach milli-kelvin temperature. However, it is sometimes non trivial to perform the measurements at this temperature. All the electrons have extremely low heat capacity at milli-kelvin temperatures. Therefore, even small coupling with the outside environment can increase the sample temperature. To avoid such a scenario we need to install special filters inside the fridge.

Fridge set-up

In this section, we will briefly describe the basic principle of the dilution refrigerator (DR). DR systems are the only refrigerator systems that provide continuous cooling power at temperatures below 300 mK. They can provide temperatures as low as 10 mK and operate without moving parts at the low temperature stages. A DR uses the heat of the mixing of the two stable isotopes of helium, ^{3}He and ^{4}He, to obtain cooling. In order to be able to run the dilution refrigerator's cooling cycle, one should first obtain a starting temperature of liquid helium (4.2 K) or below.

The cooling cycle is possible due to special and fortunate properties of ^{3}He and ^{4}He mixtures at low temperatures. Figure 3.12**(b)** shows the vapor pressures (gas-liquid equilibrium temperature) of ^{4}He and ^{3}He respectively. As pressure is reduced, the gas-liquid equilibrium shifts towards lower temperatures. At saturated vapor pressure pure ^{4}He undergoes a phase transition at 2.17 K from a normal fluid into a superfluid (resulting in completely different properties of the two isotopes below this transition temperature). Diluting the ^{4}He with ^{3}He results in a decreasing superfluid transition temperature, as shown in Figure 3.12**(a)**. At temperatures below 0.8 K (depending on concentration) the ^{3}He / ^{4}He mixture will separate into two phases: a ^{3}He rich phase (concentrated phase) and a ^{3}He poor phase (dilute phase). Approaching absolute zero temperature, the concentrated phase becomes pure ^{3}He while in the dilute ^{4}He rich phase there remains 6.4 % of ^{3}He. The enthalpy of ^{3}He in the dilute phase is larger than in the concentrated phase. Hence energy is required to move ^{3}He atoms from the concen-

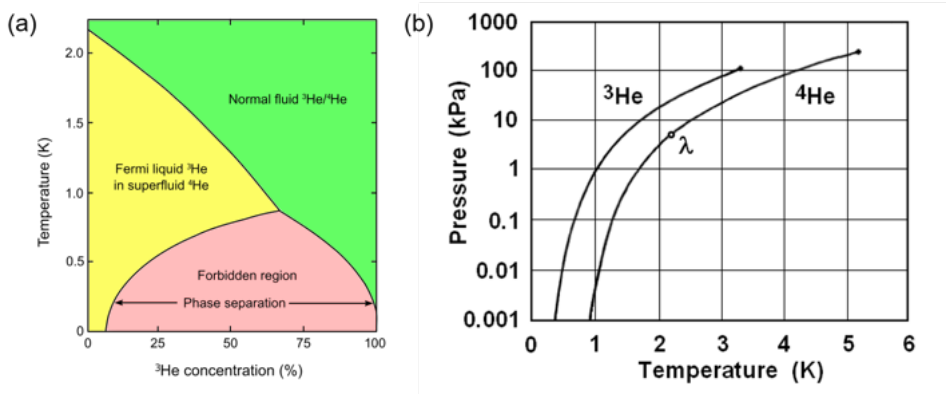

Fig. 3.12: **(a)** Phase diagram of ^{3}He and ^{4}He. **(b)** Vapour pressure of ^{3}He and ^{4}He.

trated to the dilute phase. In a DR this energy is taken from a well isolated environment (the mixing chamber), so cooling will occur. This process is analogous to adiabatic expansion of a high-pressure gas into a low-pressure gas, which absorbs heat. The heat absorbed per mole of diffused ^{3}He is equal to the difference in the enthalpy of the concentrated phase and the dilute phase, $H_c(T) - H_d(T) = T(S_c(T) - S_d(T))$, where $S_{c,d}$ is the entropy of the two phases. The entropy in both phases has a linear relation with T and the cooling power therefore is proportional to T^2.

The key difference between dilution cooling and pumping cooling is that the latent heat L of a gas-liquid transition has a lower bound even in the limit of zero temperature, while the 'latent heat' of the diffusion from the concentrated phase to the diluted phase $H_c(T) - H_d(T)$ goes to zero when $T \to 0$.

For the use of the dilution fridge here we will summarize the main points to cool down the fridge and where the heat goes in each step.

1. 300K to 4K: Exchange gas coupled to 4He bath or pulse tube. Heat removed by evaporation of ^{4}He or pulse tube.

2. 4K to 1K: Condensation of helium gas while 1K pot is turned on. Heat removed by evaporation of ^{4}He in the 1K pot.

3. 1K to 0.3K: ^{3}He pumped out from the mixture by a turbo pump. Heat removed by pumped out ^{3}He.

4. Below 0.3K: ^{3}He crossing the concentrated-dilute phase boundary. Heat removed by pumped out ^{3}He.

Fridge wiring

The typical cooling power of the dilution fridge is of the order of 100 μW at T = 100 mK. It is necessary to decrease any thermal link with the environment.

There are three different mode of heat transfer: conduction, convection and radiation. In a cryogenic system, all gases (including helium) are adsorbed in the internal cold surfaces, and therefore convection cannot occur. Conduction and radiation, however, is ubiquitous and must be carefully minimized. Generally the main thermal connection between the sample and the outside environment is via the conductive wires. Let's consider a piece of metal with thermal conductivity $K(T)$, length L and cross section A. Temperature of the two ends are T_1 and T_2 respectively. The heat conduction through the wire is equal to

$$\dot{Q} = K(T)A\frac{dT}{dx} \tag{3.1}$$

multiply both sides with dx we find

$$\dot{Q}L = A\int_{T_1}^{T_2} K(T)dT \quad \dot{Q} = \frac{A}{L}\int_{T_1}^{T_2} K(T)dT \tag{3.2}$$

If $T_2 = 300$ K and $T_1 = 4$ K, the material specific thermal integral $\int_0^T K(T)dT = \Theta(T)$ at T_1 is negligible compared to T_2. So we need to use the material which has much higher $\Theta(T_1)$ than $\Theta(T_2)$.

Pure copper has very high electrical conductivity and extremely high thermal conductivity as well. For wiring from 4K to 300K, we want to minimize the thermal coupling from 300K into the 4K parts of the fridge. Therefore, a resistive metal or alloys, such as phosphorus bronze, manganin, brass, or beryllium copper, is typically used. These materials have one or two orders of magnitude smaller thermal conductivity integral than copper, and can greatly reduce the heat conduction through the wires.

In a DR, the wiring usually consists of several parts. The wires that come from room temperature are typically thermally 'anchored' at several stages, at 4 K (helium bath/pulse tube), at 1 K (1 K pot/still) and finally at 900 mK, before they reach the sample, so that heat is

dumped into an intermediate stage that has much larger cooling power, instead of the sample. In between these stages, resistive metals such as manganin or phosphorus bronze can be used. The final connection between the mixing chamber and the sample, however, is made with pure copper. This is because the sample, while sitting on an insulating chip carrier and in vacuum, has no thermal coupling to the mixing chamber other than the sample wires. To effectively cool down the sample, it is necessary to use a thermally conducting metal to couple it to the mixing chamber. Pure copper wires are the best choice for this purpose. The choice of wiring material and wire diameter further depends on the acceptable wiring resistance. In general, low wiring resistance is contradictory with low thermal coupling because of the Wiedemann-Franz law. For typical four-wire (Kelvin) connection, a resistance of 100 Ω per wire has no effect on the measurement, but it might be problematic for certain experiments that requires low-impedance sourcing. The last pathway of heat transfer - radiation, should also be avoided in designing a sample stage. This can be alleviated by inserting radiation shields between parts at different temperatures. In a DR, the sample should only be able to see parts at 4K or lower. Since thermal radiation power scales as T^4 radiation from parts at 4K is in general not detrimental to the sample temperature, but it is still preferable to enclose the sample in some type of opaque shroud anchored to the mixing chamber temperature.

Filtering

Thermal radiation takes the form of incoherent electromagnetic waves that propagate in free space. Since the photons that emanate from hotter surfaces have higher energy density than the photons that emanate from colder surfaces, the net result is a heat transfer mediated by the photons. By blocking the line-of-sight paths from the hotter surfaces with a radiation shield, we effectively block these thermally excited electromagnetic fields from propagating, thus cutting down on the thermal radiation power. However, in a DR there is yet another loophole for thermally excited electromagnetic fields to leak into the sample, and it is again the sample wires. Being good conductors, these wires also carry high-frequency electromagnetic waves. They act like a wave-guide to transmit thermal radiation into the sample. Unless proper filters are installed, frequency components up to 100 GHz can

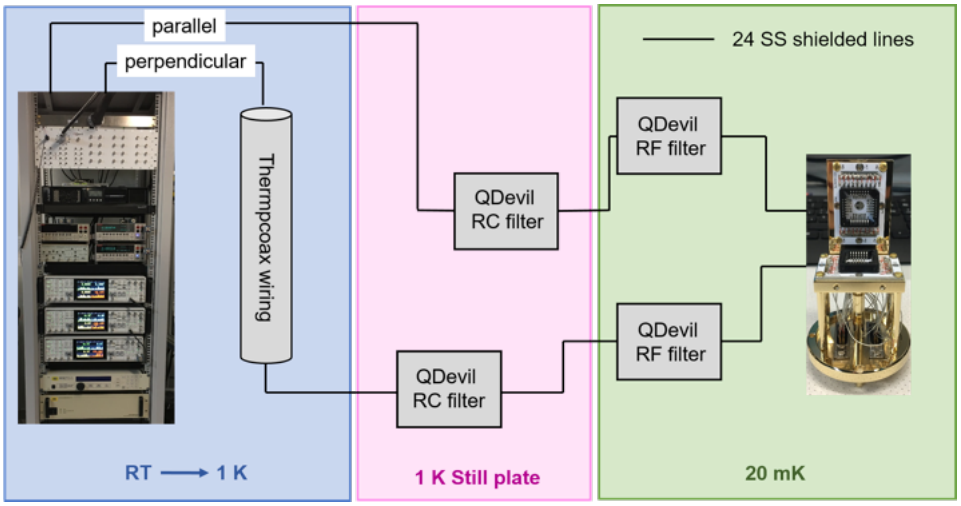

Fig. 3.13: Filtering in the dilution fridge.

leak into the system.

In our DR, we combine the copper-tape filter with a two-stage lumped RC filter to achieve full-bandwidth filtering, from 16 kHz up to optical frequencies. The RC filters are anchored at the 1K pot, while the copper-tape filter is wrapped around the cold finger of the mixing chamber right before connecting to the sample. The last part of the connection towards the sample should be made by pure copper wires anchored at the mixing chamber temperature to efficiently thermalize the sample. The choice of R and C values also deserves some attention: if R is too large (larger than a few kΩ), each wire contributes too much lead resistance, making four-probe measurement more tricky to perform; if C is too large, an a.c. signal will experience a large phase delay when passing through it, causing trouble with the lock-in measurements and limits the maximum measurement frequency. The full instrumentation setup is illustrated in Figure 3.13.

3.3 High magnetic field set-up

We have measured our devices in the European Magnetic Field Laboratory (EMFL) upto an unprecedented high magnetic field of $B = 34$T. Although the measurement set up was similar to transport, the sample probing was very different than our typical dilution fridge. The

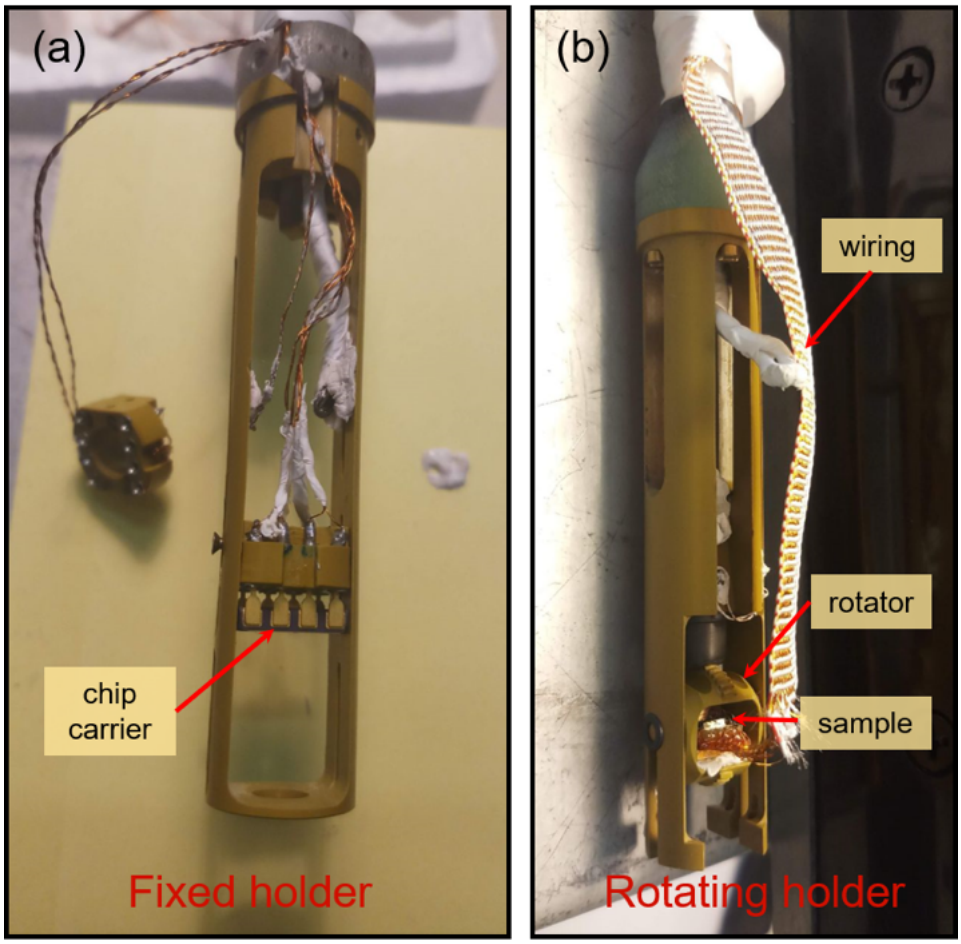

Fig. 3.14: Sample probe and holder in high magnetic field set-up.

structure of the magnet is much bigger and stays underground. The dilution fridge is placed inside the magnet and the sample stick is such that, it sits exactly at the centre of the magnetic field.

The structure of these magnets are way more complicated than superconducting coil magnets. They have multiple layers made of different materials. Each of these layers gives rise to different magnetic field.

The basic design of this magnet requires very high current flow while operating at a magnetic field above $B = 20$ T. This huge current causes instability and mechanical vibration. The mechanical vibration caused by the magnet translates into electrical noise in our measure-

ment. To avoid this problem we have used several filters and amplifiers for the measurement. At the same time, the sample holder is also different and smaller than our typical one. In Figure 3.14 we have shown the sample holders at the bottom of a long probe. We have used a fixed holder and a rotating probe for different measurements that we will describe in Chapter 5.

Chapter 4

Chern Insulators in Magic-angle Twisted Bilayer Graphene

Low energy flat electronic bands in magic angle twisted bilayer graphene host a series of strongly correlated electronic phenomena which are otherwise absent in a single system. Some of these states such as correlated insulators, superconductors, magnetism, anomalous quantum hall effect etc. are quite rare to observe. The presence of various phenomena in a single platform suggests that the strong correlation breaks certain symmetries of the system and gives rise to these many body quantum phases. These phases can also be stabilised by several external parameters such as electric field, magnetic field, pressure, strain etc. However, the exact microscopic mechanism of these states are still unclear to the community. It is important to understand the topology and symmetry of the flat bands in order to unveil the mechanism of these quantum phenomena.

The low energy bands are four-fold (spin and valley) degenerate and are separated from the higher energy dispersive bands at charge neutrality point (CNP) [61]. Two four-fold degenerate bands can be understood as the series of eight-fold degenerate topologically non-trivial bands [62].

In condensed matter physics, one of the main topological invariant of the Bloch bands is its Chern number, which dictates the quantum phases of the particles inside the band. In this chapter, we will present the observation of Chern bands in MATBG and underlying topological

nature of the system. In the first section, we will introduce the general idea of Chern number of bands and Chern insulator.

4.1 Introduction to Chern insulator

Chern insulator can be described as a filled Bloch band in a lattice characterized by a non-zero Chern number even in the absence of an external magnetic field. But before going into the details of the Chern insulator, we will first discuss a system of two dimensional electron gas in an external magnetic field.

4.1.1 Quantised Landau levels

The Lagrangian for a particle of mass m and charge $-e$ moving in a background magnetic field $\mathbf{B}$ $(\nabla \times \mathbf{A})$ is given by,

$$L = \frac{1}{2}m\dot{x}^2 - e\dot{x} \cdot A \tag{4.1}$$

From this Lagrangian, we can derive the Hamiltonian of the system given by,

$$H = \frac{1}{2m}(\mathbf{p} + e\mathbf{A})^2 \tag{4.2}$$

Since the electrons are restricted in the plane, we can write $\mathbf{x} = (x, y)$ and consider the magnetic field to be constant and perpendicular to the plane, $(\nabla \times \mathbf{A}) = \mathrm{B}\hat{z}$. The canonical commutation relations are

$$[x_i, p_j] = i\hbar\delta_{ij} \quad \text{and} \quad [x_i, x_j] = [p_i, p_j] = 0 \tag{4.3}$$

We will first calculate the energy spectrum by using the pure algebraic method, where we don't have to specify a choice of gauge potential $\mathbf{A}$. We will also consider,

$$m\dot{x} = \mathbf{p} + e\mathbf{A} = \pi \tag{4.4}$$

Now, the commutation relations from the Poisson bracket are,

$$[\pi_x, \pi_y] = -ie\hbar B \tag{4.5}$$

Let us introduce the raising and lowering operator as,

$$a = \frac{1}{\sqrt{2e\hbar B}}(\pi_x - i\pi_y) \quad \text{and} \quad a^\dagger = \frac{1}{\sqrt{2e\hbar B}}(\pi_x + i\pi_y) \tag{4.6}$$

In terms of these operators the Hamiltonian can be written as,

$$H = \frac{1}{2m}\pi \cdot \pi = \hbar w_B(a^\dagger a + \frac{1}{2}) \tag{4.7}$$

In this Hilbert space the energy eigenstates can be constructed by the creating and annihilating operator as,

$$a^\dagger|n\rangle = \sqrt{n+1}|n+1\rangle \quad \text{and} \quad a|n\rangle = \sqrt{n}|n-1\rangle \tag{4.8}$$

In this picture the energy of the state $|n\rangle$ is,

$$E_n = (n + \frac{1}{2})\hbar\omega_B \tag{4.9}$$

In the presence of a magnetic field, the energy states of a particle get equally spaced, and the spacing is proportional to the magnetic field, B. These energy levels are called Landau levels. Unlike the harmonic oscillator, each of these energy state has a degeneracy, which is associated with the choice of gauge potential, $\mathbf{A}$.

Landau gauge

We can choose the gauge potential such that,

$$\nabla \times \mathbf{A} = B\hat{z} \tag{4.10}$$

In the Landau gauge picture, $\mathbf{A} = xB\hat{y}$, where the magnetic field B has both translational and rotational symmetry in the (x, y) plane. However, $\mathbf{A}$ breaks translational symmetry in the x direction and also breaks rotational symmetry. In this picture, the Hamiltonian can be written as,

$$H = \frac{1}{2m}\left({p_x}^2 + (p_y + eBx)^2\right) \tag{4.11}$$

The energy eigenstates are

$$\Psi_k(x, y) = e^{iky} f_k(x) \tag{4.12}$$

Acting on this wavefunction with the Hamiltonian, the operator p_y will get replaced by its eigenvalue $\hbar k$,

$$H\Psi_k(x, y) = \frac{1}{2m}(p_x^2 + (\hbar k + eBx)^2)\Psi_x(x, y) \equiv H_k\Psi_k(x, y) \tag{4.13}$$

The energy eigenvalues are

$$E_n = \hbar w_B \left(n + \frac{1}{2}\right) \tag{4.14}$$

In this picture if we write down the full wavefunction in the explicit form,

$$\Psi_{n,k}(x,y) \sim e^{iky} H_n(x + kl_B^2) e^{-(x+kl_B^2)^2/2l_B^2} \tag{4.15}$$

Here, $l_B = \sqrt{\frac{\hbar}{eB}}$ is called the magnetic length which governs any quantum phenomena in a magnetic field.

Degeneracy

The wavefunction depends on the two quantum numbers n and k. However, the energy of each state depends on only one quantum number n.This indicates that the eigenstate has a degeneracy associated with it. If we consider a sample with two length scales in the x and y direction to be L_x and L_y, the total number of states will be

$$N = \frac{L}{2\pi} \int_{-L_x/l_B^2}^{0} dk = \frac{L_x L_y}{2\pi l_B^2} \tag{4.16}$$

In the quantum mechanical picture, total current is given by,

$$\mathbf{J} = -\frac{e}{mA} \sum_{filledstates} \langle \Psi | - i\hbar\nabla + e\mathbf{A} | \Psi \rangle \tag{4.17}$$

In the Landau gauge picture, if we apply an electric field in the x direction, the current in the x-direction is, $J_x = 0$. The current in the y direction is given by,

$$J_y = -\frac{e}{mA} \sum_{n=1}^{\nu} \sum_{k} \langle \Psi_{n,k} | - i\hbar \frac{\partial}{\partial y} + exB | \Psi_{n,k} \rangle \tag{4.18}$$

Now if we simplify the J_y compare it with the conductivity tensor, we have,

$$\sigma_{xx} = 0 \quad \text{and} \quad \sigma_{xy} = -\frac{e\nu}{\Phi_0} \tag{4.19}$$

Or, in terms of resistivity,

$$\rho_{xx} = 0 \quad \text{and} \quad \rho_{xy} = \frac{\Phi_0}{e\nu} = \frac{2\pi\hbar}{e^2\nu} \tag{4.20}$$

This is the typical Quantum hall resistivity in the Landau gauge picture. In order to understand the Chern insulator, we have to first realize the concept of Berry phase and Chern number of a quantum mechanical particle in a magnetic field.

4.1.2 Berry phase and Berry connection

Berry phase is an important concept in the topological band theory. It tells us that in quantum adiabatic transport under a slowly varying magnetic field, the wavefunction of the particles can be modified by terms other than the dynamical phase. We will present a brief description of the Berry phase of a particle in an external magnetic field and later on calculate the Chern number from it.

Computing the Berry phase

Let us consider a system with x^a number of degrees of freedom. The Hamiltonian of this system can be written as $H(x^a, \lambda^i)$, where λ^i are the parameters of the Hamiltonian. These parameters are fixed, with their values determined by some external apparatus. To begin with, the system is in the state $|\Psi\rangle$. If we change the parameter λ of the Hamiltonian, the state itself will also evolve as $|\Psi(\lambda(t))\rangle$. If we vary the parameter λ and finally put it back to the initial state, according to the adiabatic theorem in quantum mechanics, the energy eigenstate will also remain in its initial state, except it will gain a phase difference. The new state will be

$$|\Psi\rangle \to e^{i\gamma}|\Psi\rangle \tag{4.21}$$

The wavefunction of the system will evolve through the time dependent Schrödinger equation,

$$i\hbar\frac{\partial|\Psi\rangle}{\partial t} = H(\lambda(t))|\Psi\rangle \tag{4.22}$$

Now, for every choice of the λ there will be a ground state with fixed phase, and these states are defined as $|n(\lambda)\rangle$. According to the adiabatic theorem, the ground state can be written as,

$$|\Psi(t)\rangle = U(t)|n(\lambda(t))\rangle \tag{4.23}$$

Where $U(t)$ is some time dependent phase. If the particle traverses in a closed path C in the parameter space, $U(t)$ will be given by,

$$U(t) = \exp\left(\oint_C \langle n|\frac{\partial}{\partial\lambda^i}|n\rangle\dot{\lambda}^i dt\right) \tag{4.24}$$

The Berry curvature is given by,

$$A_i(\lambda) = -i\langle n|\frac{\partial}{\partial\lambda^i}|n\rangle \tag{4.25}$$

And finally the Berry phase is given by,

$$e^{i\gamma} = \exp\left(-i\oint_C A_i(\lambda)d\lambda^i\right) \tag{4.26}$$

The Berry curvature is the ingredient to calculate the Chern number of a band in the crystal. We will now consider a two dimensional crystal to calculate the Chern number of the electronic band.

4.1.3 Chern number of the band

In the last section, we learned that Berry phase is the integral of the Berry potential over a closed path. In this thesis we will always consider a two dimensional electronic system where this closed curve is given by the the Fermi surface of the Brillouin zone (BZ). In this picture, The Chern number of the filled band is given by the the integral of the Berry curvature over the full Brillouin zone and is related to the Hall conductance. In this section, we will derive the Chern number of a filled band from the Berry curvature.

Let us consider a spin in a magnetic field $\vec{B}$. In Hilbert space, it consists of two states. The Hamiltonian can be written as,

$$H = \vec{B}\cdot\vec{\sigma} - B \tag{4.27}$$

This Hamiltonian has two eigenvalues, 0 and $-2B$. We can denote the ground state as $|\downarrow\rangle$ and the excited state as $|\uparrow\rangle$. So, we can write $H|\downarrow\rangle = -2B$ and $H|\uparrow\rangle = 0$.

Spherical polar co-ordinate

We will consider the magnetic field $\vec{B}$ in spherical polar co-ordinate. The Hamiltonian can be written as,

$$H = -B\begin{pmatrix}\cos\theta - 1 & e^{-i\phi}\sin\theta \\ e^{+i\phi}\sin\theta & -\cos\theta - 1\end{pmatrix} \tag{4.28}$$

Two normalised eigenstates are given by,

$$|\downarrow\rangle = \begin{pmatrix} e^{-i\phi}\sin\theta/2 \\ -\cos\theta/2 \end{pmatrix} \quad \text{and} \quad |\uparrow\rangle = \begin{pmatrix} e^{-i\phi}\cos\theta/2 \\ \sin\theta/2 \end{pmatrix} \tag{4.29}$$

We can now easily calculate the Berry phase arising from these states,

$$A_\theta = -i\langle\downarrow|\frac{\partial}{\partial\theta}|\downarrow\rangle = 0 \quad \text{and} \quad A_\phi = -i\langle\downarrow|\frac{\partial}{\partial\theta}|\downarrow\rangle = -\sin^2\left(\frac{\theta}{2}\right) \tag{4.30}$$

The resulting Berry curvature is given by,

$$F_{\theta\phi} = \frac{\partial A_\phi}{\partial\theta} - \frac{\partial A_\theta}{\partial\phi} = -\frac{1}{2}\left(\sin\frac{\theta}{2}\right) \tag{4.31}$$

Now in the Cartesian co-ordinate, the Berry curvature takes the form, $F_{ij} = -\epsilon_{ijk}\frac{B^k}{2B^3}$. In order to calculate the Berry phase from this, let us consider a closed path C that enclosed the surface S. The Berry phase is given by,

$$\int F_{ij}dS_{ij} = 2\pi C \tag{4.32}$$

This integer $C \in \mathbf{Z}$ is called the Chern number.

Hall conductance and Chern number

The Hall conductance equals the integral of the Berry curvature of the filled bands over the full Brillouin zone (BZ). The Hall conductivity of a band insulator, when the Fermi level is in the gap, is the integral of the Berry curvature over the BZ [63].

$$\sigma_{xy} = \frac{e^2}{h}\frac{1}{2\pi}\int\int d_{kx}d_{ky}F_{xy}(k) \tag{4.33}$$

Hence, from our Hall conductance transport measurements, we can calculate the Chern number of the band.

4.2 Different degeneracies in MATBG

The low energy physics of magic angle twisted bilayer graphene is dominated by the moiré Brillouin zone of the superlattice which results from the twisting of the two layers of graphene. In the mini BZ of MATBG,

several symmetries are present in the ground state. C_{2x}, C_{3z} and $C_{2z}\mathcal{T}$ are the rotational symmetry present in the system. This system also has unitary particle-hole symmetry. All moiré bands are four fold degenerate, valley (K and K') and spin ($\uparrow$ and $\downarrow$). We will discuss this degeneracy in the next following sections. The eightfold Landau level degeneracy in bilayer graphene is reduced to fourfold. Experimentally, this degeneracy lifting is always seen in samples showcasing the correlated insulators and superconductivity. Importantly, each Landau level emanating from charge neutrality is eightfold degenerate. This degeneracy can be explained by noting the doubling due to spin, valley and layer degrees of freedom. We remark that the layer index is not generally a good quantum number, however, because these low-lying Landau levels can be understood as coming from the mini Dirac points, there is still a twofold degeneracy arising from the mini-valley degeneracy.

4.3 Basic characterization of MATBG

I have started my PhD when the field of magic angle twisted bilayer graphene has just started (2018). So for obvious reason, I have spent a long time figuring out the optimal stacking and fabrication process to get clean and homogeneous devices. In this section, we will show some basic characterization of the magic angle twisted bilayer graphene devices and how to calculate the twist angle of these devices from the Landau fan diagram.

4.3.1 Temperature dependence of the resistance

Twisted bilayer graphene hosts a pair of flat bands when rotated by an angle θ close to the first magic angle $\theta_M = 1.1°$. As we mentioned in Chapter 1, due to the formation of this flat band, electrons loose their kinetic energy and get confined in the band. This results to a higher resistance and lower conductance in our devices compared to the normal AB Bernal stacked bilayer graphene. The room temperature four probe resistance for a device close to magic angle is of the order of R_{xx} = 10 - 20 kΩ. This is the very first check that we measured in a room temperature vacuum probe station. In this process, we discard the devices which have lower four probe resistance ($R_{xx} < 5$ kΩ). After this screening process, we measured the potentially good

devices in the 1.5 K cryostat. Where we thoroughly measured the R_{xx} as a function of gate voltage V_g at different temperatures staring from room temperature (300 K) until $T = 1.4$ K.

We first plotted the resistance in the temperature range of $T =$ 40 K to 1.4 K in Figure 4.1. The first line curve in Figure **(a)**, is at 40 K which clearly shows a oscillatory pattern in R_{xx}. As we decrease the temperature, this oscillatory pattern develops to either charge neutrality point (CNP) or band insulator (BI) or different integer filling insulating states. The last line curve in Figure **(a)** is at $T = 1.4$ K. The sharp peak in resistance at $V_g = 0$ Volt corresponds to the CNP with the resistance value of $R_{xx} = 22$ kΩ. As we keep increasing the gate voltage either in positive or in negative direction, the band gets populated with increased number of electrons or holes. Around $V_g =$ (±) 1.4 Volt, we found another highly resistive peak which corresponds to the band insulator. This marks the full filling of the band. At this point we have a band gap where the density of states (DoS) diverges and the conductance becomes very small giving rise to high resistance ($R_{xx} \sim 150$ kΩ).

We have further measured the device in the dilution fridge with a base temperature of $T = 20$ mK. We will discuss the detailed temperature dependence of different filling inside the flat band in Chapter 8. In this section we want to draw attention to the superconducting pockets that develop close to the half filling of the band. In Figure **(b)**, the last curve at $T = 20$ mK has three zero-resistive superconducting pockets at $V_g =$ - 1.0 Volt (-1/2 filling) and at $V_g =$ + 0.75 & + 0.9 Volt (before and after +1/2 filling). We will discuss the superconducting states in detail with several measurements later in this chapter. Before that, we will calculate the exact twist angle of this device from the magnetic field dependence of R_{xx}.

4.3.2 Extraction of the twist angle

Accurate calculation of the twist angle of the devices is very important in understanding the phenomena observed in our devices. We used several methods to determine the twist angle of our devices.

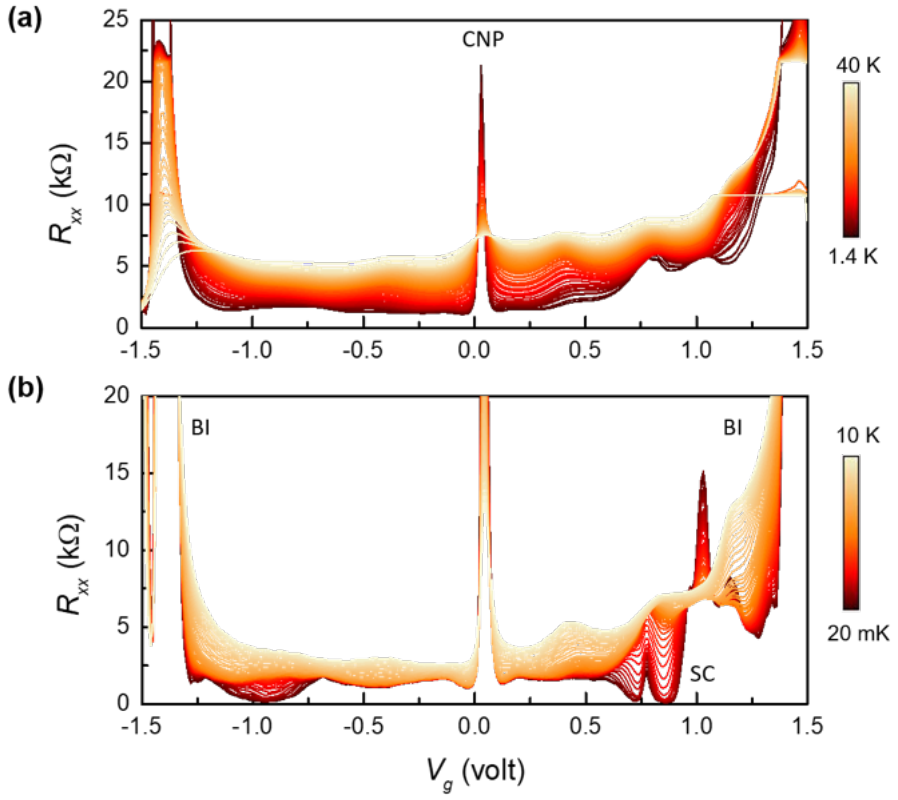

Fig. 4.1: Temperature dependence of the longitudinal resistance R_{xx} as a function of gate voltage V_g. **(a)** shows R_{xx} as a function of V_g in the temperature range of $T = 40$ K to 1.4 K. Charge neutrality point (CNP) and band insulators (BI) are marked. **(b)** shows the same R_{xx} vs. V_g for the temperature range of $T = 10$ K to 20 mK. This clearly shows the insulating half filling state in the electron doped side with two superconducting pockets on each side and an undisturbed superconducting pocket at the hole doped side.

Method 1 :

The superlattice carrier density n_S is defined as the total number of electrons required to completely fill one flat band in the superlattice. n_S is related to the twist angle θ by,

$$n_s = \frac{4}{A} \approx \frac{8\theta^2}{\sqrt{3}a^2} \tag{4.34}$$

where A is the unit cell area and $a = 0.246$ nm is the lattice constant of graphene. When the twist angle is sufficiently small ($1^\circ < \theta < 3^\circ$), the superlattice carrier density n_S is associated with a pair of single particle band gaps at their corresponding Fermi energy. Therefore, we can calculate the twist angle θ, from the measured density of the insulating states at the band edge of the superlattice according to equation 4.34. Experimentally we apply local gate voltage V_g to tune the carrier density inside the band. So first we will describe the process to calculate the carrier density n from the applied gate voltage V_g via the graphite gate. The graphite gate acts as a parallel plate capacitor. The carrier density n is related to the V_g by this equation,

$$n = \frac{C_g V_g}{e} \tag{4.35}$$

where C_g is the gate capacitance. We derive this C_g from the Landau fan diagram of the flat band. Under an external magnetic field the flat band develops several Landau level starting from CNP. We consider a LL with filling factor $\nu_{LL} = 4$ to calculate the gate capacitance where they are related by,

$$\nu_{LL} = \frac{nh}{eB} = \frac{h}{e^2}\frac{C_g V_g}{B} \tag{4.36}$$

From the slope of a Landau level in V_g-B phase space C_g can be calculated for a particular LL. Once we know the value of C_g for a particular device, the superlattice density n_S can be easily found out from the resistance peak at the band insulator. In this device the voltage required to completely fill the band is $V_S = 1.4$ Volt. So the superlattice carrier density will be given by $n_S = C_g V_S/e$. Finally we calculate the twist angle from equation 4.34. In Figure we have shown a resistance curve for a device with twist angle $\theta = 1.04^\circ$

Method 2 :

There is another method which involves Hofstadter's butterfly to extract the twist angle of the devices. This method is more useful for the devices with smaller twist angle. The effect of applying strong magnetic fields such that the magnetic length becomes comparable with the superlattice potential length-scale is described by the Hofstadter's butterfly. In the density picture this model is given by the Wannier diagram where the Landau levels are represented by,

$$\frac{n}{n_S} = \nu\frac{\phi}{\phi_0} + s \tag{4.37}$$

where ϕ is the magnetic flux through an unit cell of the superlattice, ν is an integer and $s = 0$ labels the main Landau fan and $s = \pm\ 1$ corresponds to the first satellite Landau fan etc. Two adjacent Landau fans intersect when $\phi/\phi_0 = 1/q$ or, $1/B = qA/\phi_0$, where q is an integer. Therefore, we expect to see Landau level crossings at periodic intervals of $1/B$ with the periodicity proportional to the unit cell area A. In Figure, we plotted the magneto-transport data as a function of n and $1/B$. From the periodic crossings we calculated the unit cell area to be $A =$ which gives the twist angle $\theta = 0.95°$.

Once we measured a device the twist angle close to the magic angle, we further characterize it thoroughly in the dilution fridge. We have observed several strongly correlated phenomena such as correlated insulators, superconductors at different integer fillings of the flat band. Additionally, we found magnetic states and Chern insulators in our devices upon applying an external magnetic field. We will first describe the superconductivity of the device which is one of the most characteristic features of a magic angle twisted bilayer graphene (MATBG).

4.3.3 Superconductivity

In two dimensional systems, observation of superconductivity can be verified by several measurements such as, RT-transition, dc IV characteristics, Fraunhofer oscillation, Berezinskii-Kosterlitz-Thouless (BKT) transition etc.

In Figure 4.2 we have shown different characteristics measurements of a superconducting state in MATBG. Figure **(a)** shows the typical R vs T of a superconductor. The normal state resistance of this state is $R_{xx} = 6$ - 7 kΩ. The superconducting transition temperature, given

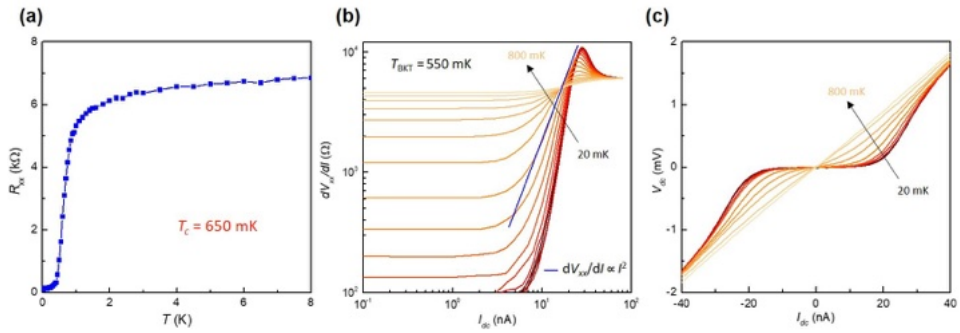

Fig. 4.2: Temperature dependence of the longitudinal resistance R_{xx} as a function of gate voltage V_g. **(a)** shows R_{xx} as a function of V_g in the temperature range of $T = 40$ K to 1.4 K. Charge neutrality point (CNP) and band insulators (BI) are marked. **(b)** shows the same R_{xx} vs. V_g for the temperature range of $T = 10$ K to 20 mK. This clearly shows the insulating half filling state in the electron doped side with two superconducting pockets on each side and an undisturbed superconducting pocket at the hole doped side.

by the temperature at which resistance of the device decreases by 50% of it's normal value is $T_c = 650$ mK. However, in two dimensional superconductor, BKT transition is more accurate to find out the T_c of the system. Figure **(b)** illustrates the differential voltage (dV/dI) as a function of bias current (I_{dc}) at different temperature from $T = 20$ mK to 800 mK. According to the BKT theory, the line fitting of $dV/dI \propto I^2$ defines the transition temperature. This dictates the transition temperature to be $T_c = 550$ mK which almost in agreement with the R vs T transition.

In Figure **(c)** we have plotted the dc IV characteristics of the superconductor from the temperature $T = 20$ mK to 800 mK. The black curve in this figure corresponds to the lowest temperature IV with the flat region in it which determines the critical current $I_c = 20$ nA of the superconductor.

In other devices, we observed several superconducting domes at different fillings along with correlated insulating states sometimes. Figure 4.3 **(a)** shows longitudinal resistance R_{xx} as a function of filling factor for several temperatures from 100 mK to 40 K. Correlated insulating states appeared at $\nu = \pm 2$ states accompanied by two strong superconducting domes. Figure **(b)** corresponds to the temperature dependence of the resistance at optimal doping of the superconductor.

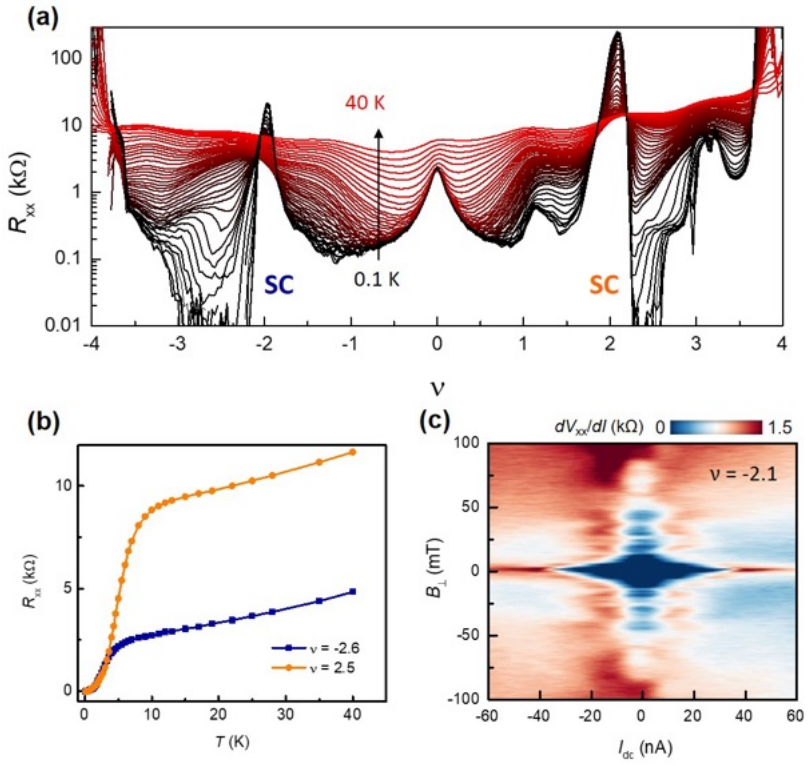

Fig. 4.3: Superconductivity. **(a)** Longitudinal resistance R_{xx} vs. ν. **(b)** Temperature dependence of longitudinal resistance R_{xx} at optimal doping of the superconducting dome. **(c)** Differential resistance dV_{xx}/dI as a function of DC current I_{dc} and B showing Fraunhofer patterns.

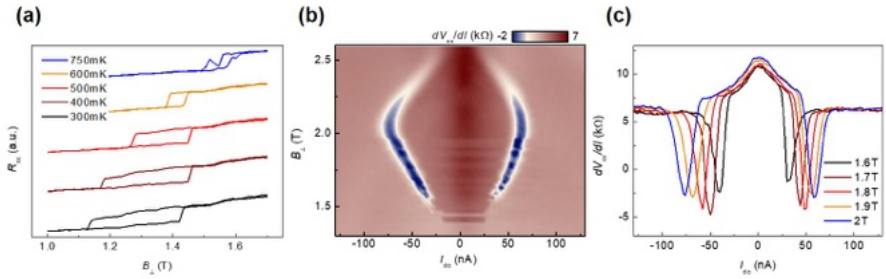

Fig. 4.4: Orbital magnetism. **(a)** shows temperature dependence of the hysteresis loop of longitudinal resistance R_{xx} as a function of $B_\perp$. **(b)** shows colour map of differential resistance dV_{xx}/dI vs. DC current I_{dc} and $B_\perp$ with carrier density fixed, showing the critical current of the magnetic state. **(c)** Line-cut of dV_{xx}/dI in **(b)** at different $B_\perp$, with critical current indicated by the deeps of dV_{xx}/dI.

In this device we have observed a critical temperature of $T_c = 5$ K (with a transition width around 7K), which is one of the highest T_c reported in MATBG devices so far. We also note that the definition of T_c as the 50% normal-state resistance value (currently used in all of the work reported in this field) give some uncertainty due to transition broadening might induced by structural inhomogeneity. We further measured the differential conductance dV_{xx}/dI as a function of perpendicular magnetic field and d.c. current bias, I_{dc}. Fraunhofer like pattern confirms the existence of superconductivity in our devices.

4.3.4 Magnetism

In addition to superconductors we also have observed a magnetic ordered state close to $\nu = +1$ state. Figure 4.4 represents a detailed measurement of this state. At zero magnetic field we did not observe any peak in R_{xx}. Above a magnetic field of $T = 1$ T, a strong hysteretic increase of R_{xx} appeared. As we measured R_{xx} as a function of upward and downward magnetic field, a clear hysteretic behavior was observed indicating the formation of a magnetic state. The hysteretic behavior faded out above $T = 750$ mK. We further measured the differential resistance as a function of $B_\perp$ and d.c. excitation current, which shows a critical current for this state pointing to a typical phase transition. Overall, these findings may suggest a close competition between topologically trivial and non-trivial insulators at $B_\perp = 0$ T, which directly

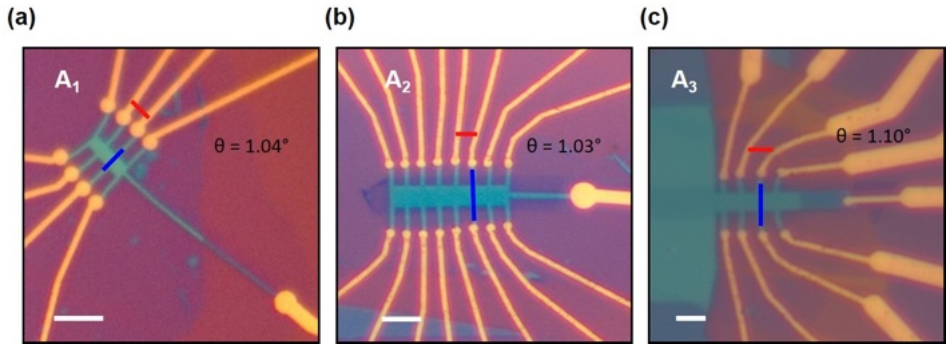

Fig. 4.5: Optical images of the device A1, A2, A3. **(a)** A1; **(b)** A2; **(c)** A3. The optical image of final devices etched in multi-terminal Hall bar geometry from graphite/hBN/MATBG/hBN stack. The red and blue lines in the device region mark the probes used for the measurement of R_{xx} and R_{xy} respectively. Scale bars are 5 μm.

impacts the superconductor and orbital magnet phases.

4.4 Chern insulators in MATBG

Now we will discuss the main result of this chapter which is the observation of Chern insulators in MATBG. As we have mentioned many times earlier that the flat bands in MATBG emerged as a rich platform to explore strongly correlated phenomena. The magnetic field phase space of the flat band also unveil many information about the band symmetry and topology of the system. Electron interaction can break the symmetry of the band and give rise to several quantum phases. The specific symmetry and degeneracy of these flat bands have been discussed in previous sections.

Here we will describe the studies of three MATBG devices close to magic angle θ = 1.03 - 1.10°. These devices were not aligned to the hBN substrates. Figure 4.5 shows the optical images of these three devices with proper scale bar. We perform four-terminal longitudinal resistance (R_{xx}) and Hall resistance (R_{xy}) measurements, where the carrier concentration ν in the MATBG is continuously controlled by voltage V_g at the graphite gate. Applying a perpendicular magnetic field $B_\perp$ at T = 1.5 K reveals a set of broad wedge-shaped regions in the ν–B phase space, where $R_{xx} \approx 0\ \Omega$. We also measured the Hall resistance R_{xy} of these states where, $R_{xy} = h/Ce^2$. These quantized

regions follow a linear slope of,

$$\frac{d\nu}{dB} = \frac{Ce}{h} \tag{4.38}$$

which can be traced to different integer fillings ν at B = 0. These singular states show a clear correspondence between the Chern number and filling factor (C, ν). We find a robust sequence for the ($\pm$4, 0), ($\pm$3, $\pm$1), ($\pm$2, $\pm$2) and ($\pm$1, $\pm$3) states in different devices.

4.4.1 Magnetic field dependence of the longitudinal resistance

We will separately show the existence of correlated Chern insulators in three different devices.

Device $A_1(\theta = 1.04°)$

Figure 4.6 demonstrates the Chern insulating states combined with the Landau levels inside the flat band of MATBG. Device A_1 has prominent Chern insulators with Chern number $C = \pm 4, 3, 2, 1$ emerging from the subsequent superlattice unit cell filling of $\nu = 0, +1, +2, +3$ without interrupted by any Landau gaps. Since we did not observe Landau levels in this device even at lowest temperature, signature of Chern states confirms their robust topological origin.

At lower T, we also observe a clear set of Landau-level (LL) fans, which follow the typically reported fourfold degeneracy at the charge neutrality point. The energy gaps associated with these states are up to an order of magnitude smaller than the gaps of the (C, ν) states, which have values of $\Delta \approx 1$ meV. The (C, ν) states are more visibly pronounced, and some already quantize below $B_\perp < 0.3$ T and $T < 10$ K. This is in contrast to LL quantization.

Device $A_2(\theta = 1.03°)$

Figure 4.7 shows Chern states along with the Landau levels emerging from CNP and $\nu = +2$ state in device A2. In addition, it has a new set of Landau levels emerging from $\nu = \pm 2$ states confirming the formation of new Fermi surface. In device A2 we observed signature of several Chern insulators ($C = \pm 1, \pm 2, \pm 3$) emerging from a single filling, ν

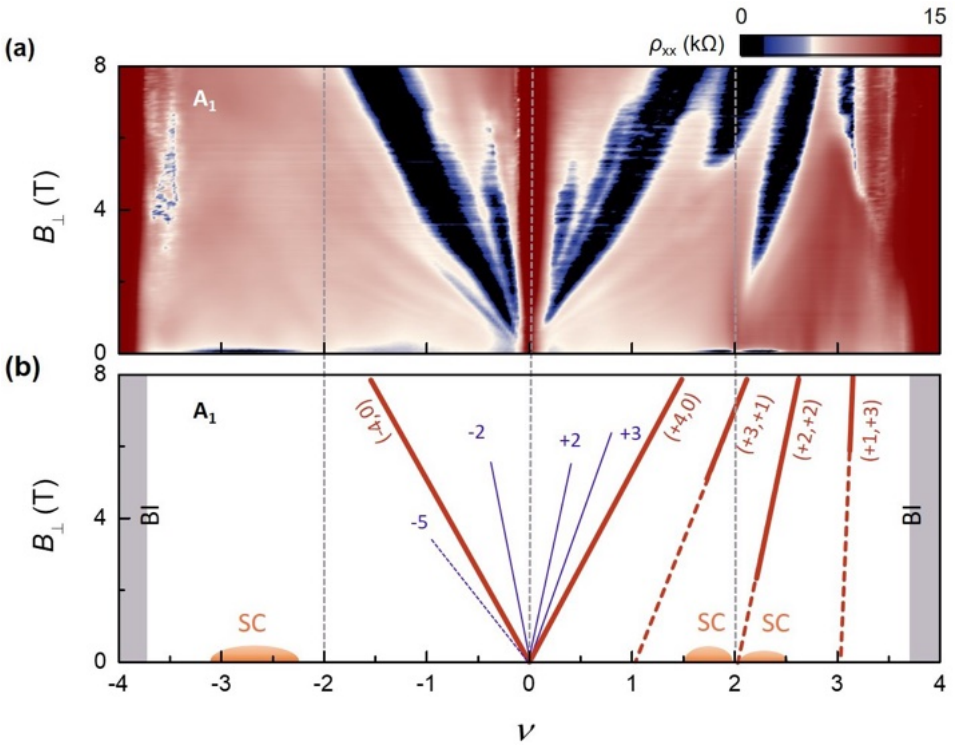

Fig. 4.6: Full range magnetic field phase diagram of flat band in device A_1 at 30 mK. **(a)** Longitudinal resistance (color plot) as a function of filling factor, ν and magnetic field $B_\perp$. **(b)** Schematics of the Landau level and Chern insulators shown in **(a)**. Dark orange lines correspond to the Chern insulators $(C, \nu) = (\pm 4, 0), (3, 1), (2, 2), (1, 3)$. Blue lines are the Landau levels emerging from CNP. Light orange regions define the position of superconductors in the phase space. We have found that the band insulator (electron doped side of (3,1) state) becomes highly resistive when B $>$ 3 T at the base temperature of 20-30 mK, and the excitation current starts to be highly suppressed, so degrading the data quality. This issue is not present for the measurements at 1.5 K, where the current is not critically suppressed by the insulator, and the data clearly shoes a correct slope for the (3,1) state.

$= \pm 3$, which hints the competition between different Chern numbers. However, they are not fully developed due to the interruption by $\nu = \pm 3$ interaction induced gap.

Device $A_3(\theta = 1.10°)$

Figure 4.8 shows the similar Chern states along with the Landau levels emerging from CNP and $\nu = +2$ state in device A3. In addition, it has a new set of Landau levels emerging from $\nu = \pm 2$ states confirming the formation of new Fermi surface. In device A2 we observed signature of several Chern insulators ($C = \pm 1, \pm 2, \pm 3$) emerging from a single filling, $\nu = \pm 3$, which hints the competition between different Chern numbers. However, they are not fully developed due to the interruption by $\nu = \pm 3$ interaction induced gap. We also observed a signature of orbital magnet at $\nu = +1$ state in device A3.

However, these states do not form in a zero $B_\perp$ field. Although they require a $B_\perp$ field to nucleate, the (± 4, 0), (3, 1) and (-2, -2) states already form at a negligibly small $B_\perp > 0.1$ T. The very small values of the field for which these states appear, especially the (-2, -2) state, suggests that they are very competitive to the true ground state in the zero field. In contrast, the (-3, -1) and (± 1, ± 3) states require higher fields of $B_\perp > 2$ T. Figure 4.9 summarizes the corresponding critical $B_\perp$ fields for all the states and devices.

We interpret these states as correlated Chern insulators (CCIs) that are driven by interactions and stabilized by a small $B_\perp$ field. These states are different than Landau levels in graphene system [64, 65]. These states are possible because the underlying flat bands of MATBG can be thought of as Chern bands with eightfold valley, spin and sublattice degeneracy, which carry opposite Chern numbers $C =$ 1 and $C =$ -1 [66–69]. Lifting the degeneracy of these bands by gaping out their Dirac points and polarizing them can create topologically non-trivial gaps. This is analogous to the interaction-driven formation of quantum Hall ferromagnets from degenerate LLs in large B fields, although the microscopic origins are distinct. In MATBG, the flat moire bands allow interactions to dominate and open CCI states in the zero B-field limit.

The exact sequence of Chern numbers at different fillings gives an insight into the dominant symmetry-breaking mechanisms. Unlike in previous studies, where $C2$ symmetry was deliberately broken by the

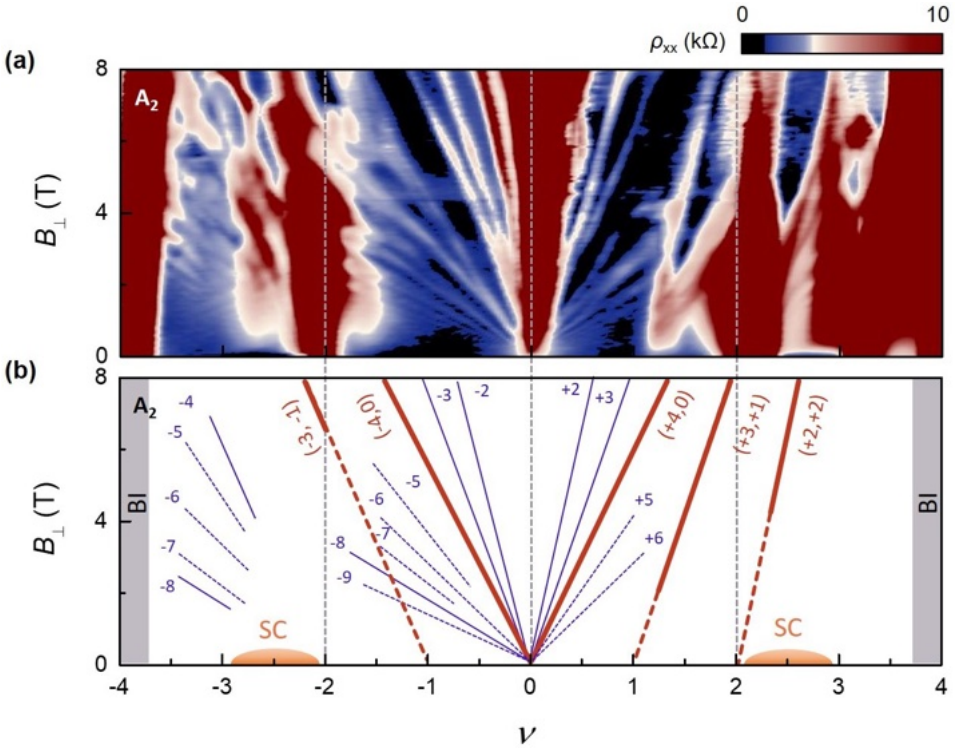

Fig. 4.7: Full range magnetic field phase diagram of flat band in device A_2 at 30 mK. **(a)** Longitudinal resistance (color plot) as a function of filling factor, ν and magnetic field $B_\perp$. **(b)** Schematics of the Landau level and Chern insulators shown in **(a)**. Dark orange lines correspond to the Chern insulators $(C, \nu) = (\pm 4, 0), (\pm 3, \pm 1), (\pm 2, \pm 2), (+1, +3)$. Blue lines are the Landau levels emerging from CNP and ν = -2. Light orange regions define the position of superconductors in the phase space.

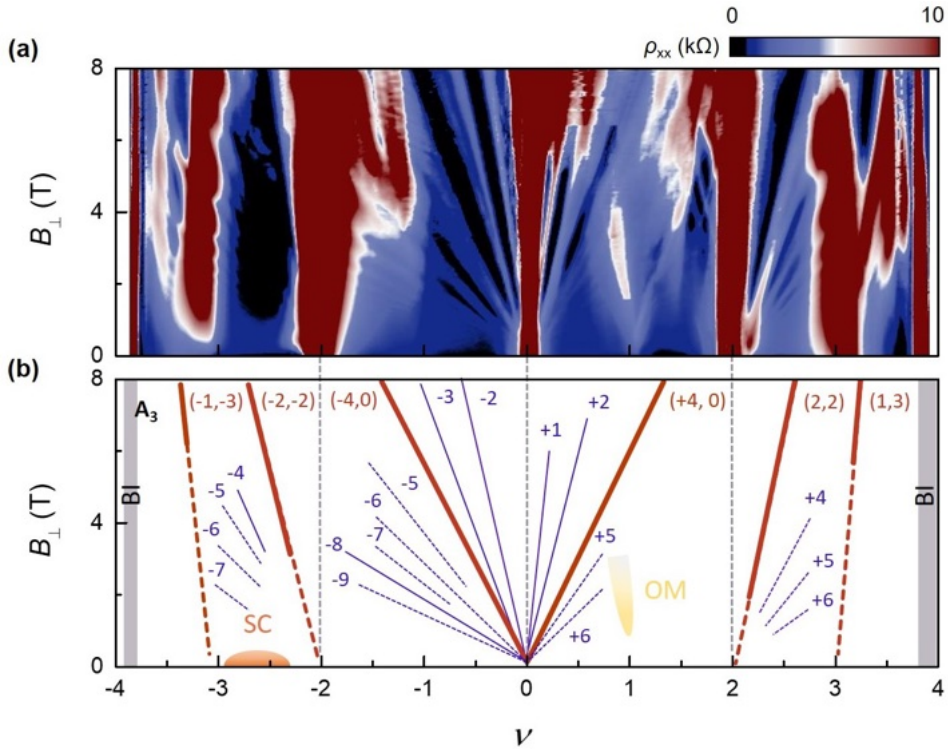

Fig. 4.8: Full range magnetic field phase diagram of flat band in device A_3 at 30 mK. **(a)** Longitudinal resistance (color plot) as a function of filling factor, ν and magnetic field $B_\perp$. **(b)** Schematics of the Landau level and Chern insulators shown in **(a)**. Dark orange lines correspond to the Chern insulators $(C, \nu) = (\pm 4, 0), (\pm 2, \pm 2), (-3, -1)(\pm 1, \pm 3)$. Blue lines are the Landau levels emerging from $\nu = 0, \pm 2$. Light yellow regions mark the position of the orbital magnet.

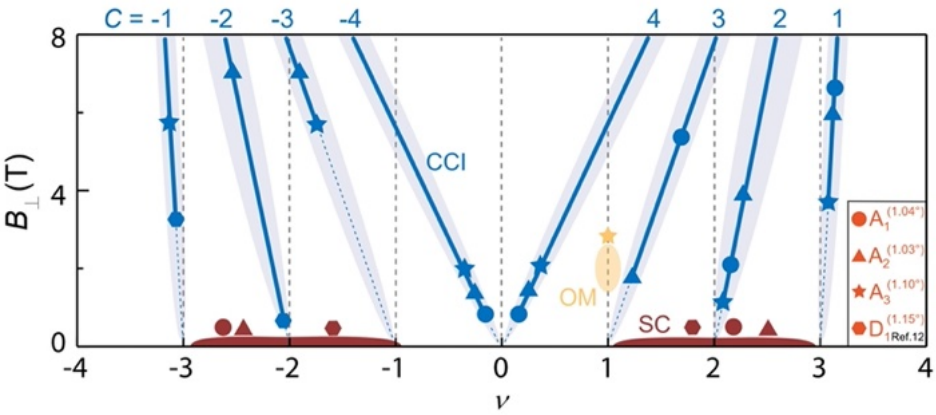

Fig. 4.9: Schematic of the cumulative phase diagram for several devices, summarizing the observed CCI, superconductor (SC) and orbital magnet (OM) in the$\nu - B_\perp$ plane. The position of the device icons for each CCI corresponds to the critical $B_\perp$ field values (uncertainties indicated by the error bars are defined by the full-width at half-minimum values of $dR_{xx}/dB_\perp$ versus $B_\perp$ for fixed C) at which these states form. Similarly, the optimal doping positions for SC are marked by the corresponding device icons.

alignment of MATBG with hBN substrates, we avoid this by keeping the angle between the crystallographic orientations of MATBG and hBN as $\theta > 10°$. Generally, broken $C2$ symmetry (and keeping T unbroken) leads to a sign reversal of the Chern numbers in the K and K' valleys; in contrast, broken T symmetry (and keeping $C2$ unbroken) is expected to preserve their Chern numbers. This can have a clear impact on the resulting many-body states and the predicted Chern numbers for each ν.

Breaking either symmetry at charge neutrality as a parent state of the other fillings predicts the (± 2, ± 2) and (± 1, ± 3) states, $C2$ breaking predicts the existence of the (± 1, ± 1) and (0, 0) states, instead of the (± 3, ± 1) and (± 4, 0) states predicted from the breaking of T symmetry and observed in the experiment. Therefore, the interactions in the $B_\perp$ field in MATBG specifically break the T symmetry at $\nu = 0$ and break both T and $C2$ symmetries at $\nu = \pm 1$ and ± 3.

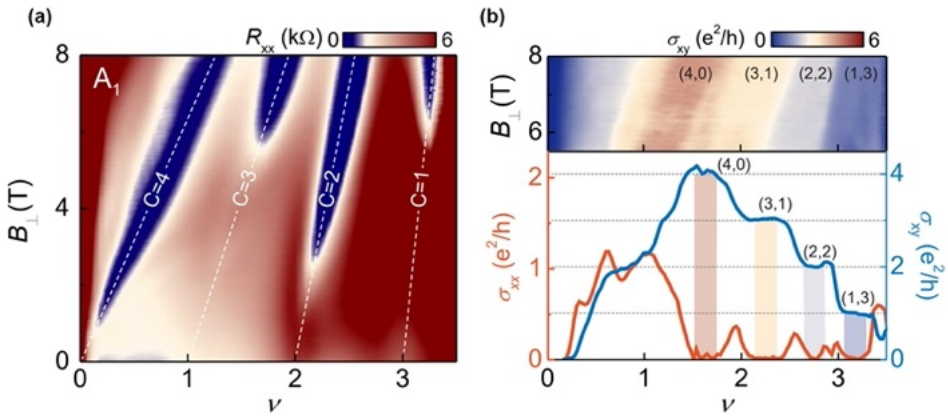

Fig. 4.10: Chern insulators in device A1. **(a)** Colour plot of R_{xx} versus ν and $B_\perp$, measured at $T = 1.5$ K. The white lines indicate the trajectories of four different topologically non-trivial Chern gaps with (C, ν) indices of (4, 0), (3, 1), (2, 2) and (1, 3). **(b)** Corresponding Hall conductance σ_{xy} versus ν and $B_\perp$ (top) and line cuts showing quantized σ_{xy} and vanishing longitudinal conductance of the Chern insulators at $B_\perp = 8$ T (bottom).

4.4.2 Magnetic field dependence of the transverse resistance

As we have discussed in previous section, the Chern number of the Chern insulator is related to the Hall conductance. In this section we will discuss the Hall conductance of these Chern states in detail. Figure 4.10 summarizes both R_{xx} and R_{xy} for the electron side of the flat band. Figure **(a)** shows the colour plot of four Chern insulators $(C, \nu) = (+4, 0)$, $(+1, +3)$, $(+2, +2)$ and $(+3, +1)$. The dark blue coloured wedge shaped regions show perfect zero resistance. Figure **(b)** shows the Hall conductivity σ_{xy} for these Chern states. The σ_{xy} values are perfectly quantized at the specific integer quantization value. The bottom panel is the line cut for both R_{xy} and σ_{xy} taken at $B = 8$ T. For the Chern state $(C, \nu) = (+4, 0)$, $(+1, +3)$, $(+2, +2)$ and $(+3, +1)$ the Hall conductance σ_{xy} is quantized at a value of $4e^2/h$, $3e^2/h$, $2e^2/h$, $1e^2/h$ correspondingly. The integer value in front of the e^2/h gives the Chern number C.

Here we have to discuss a central question. Why do the Chern insulators require a finite magnetic field to nucleate? Since the $(\pm 4,$

0), (3, 1) and $(-2, -2)$ states already occur in the weak-field limit as low as $B_\perp \approx 0.1$ T corresponding to a negligibly small magnetic flux per moire unit cell of only $\Phi < 0.01\Phi_0$ (where Φ_0 is the flux quantum), we find it unlikely that the onset of the Hofstadter subbands is responsible. Because T breaking is crucial to the observed sequence of Chern states, we would expect the application of weak $B_\perp$ to stabilize this phase because the applied magnetic field breaks the T symmetry (but not $C2$). At $B_\perp = 0$, the many-body states of different Chern numbers, including topologically trivial $C = 0$ states, closely compete with one another in energy and are obscured by disorder, but the application of $B_\perp$ energetically favours the states with higher C values [70–72].

4.5 Broken symmetry in the flat band

We have further explored two different scenarios where either C2 or time reversal symmetry T is broken. Breaking different symmetries of the parent state in charge neutrality ($\nu = 0$) can give rise to different observable especially at $\nu = 0$ and 1 state. As shown in following Figure breaking C2 symmetry gives opposite Chern numbers in different valleys. In this scenario, the only allowed total Chern numbers at $\nu = 0$ state are $C = 0$ instead of $C = \pm 4$ observed experimentally and well explained by broken T symmetry. Similarly, breaking C2 symmetry (parent state at $\nu = 0$) always leads to a total Chern number of $C = \pm 1$ at $\nu = \pm 1$ instead of $C = \pm 3$ we observed experimentally. By comparing our experiential results and following schematic, the Chern insulating state stabilized at magnetic field breaks T symmetry at $\nu = 0$ and breaks both T and C2 at $\nu = \pm 1, \pm 3$.

4.6 Difference between Chern insulators and Landau levels

We calculated the energy gap of these Chern insulators and these are upto one order magnitude larger than the typical Landau level gaps in these samples.

Figure 4.12 shows the temperature dependence of both longitudinal and transverse resistance R_{xx}, R_{xy} of the Chern insulators. We have

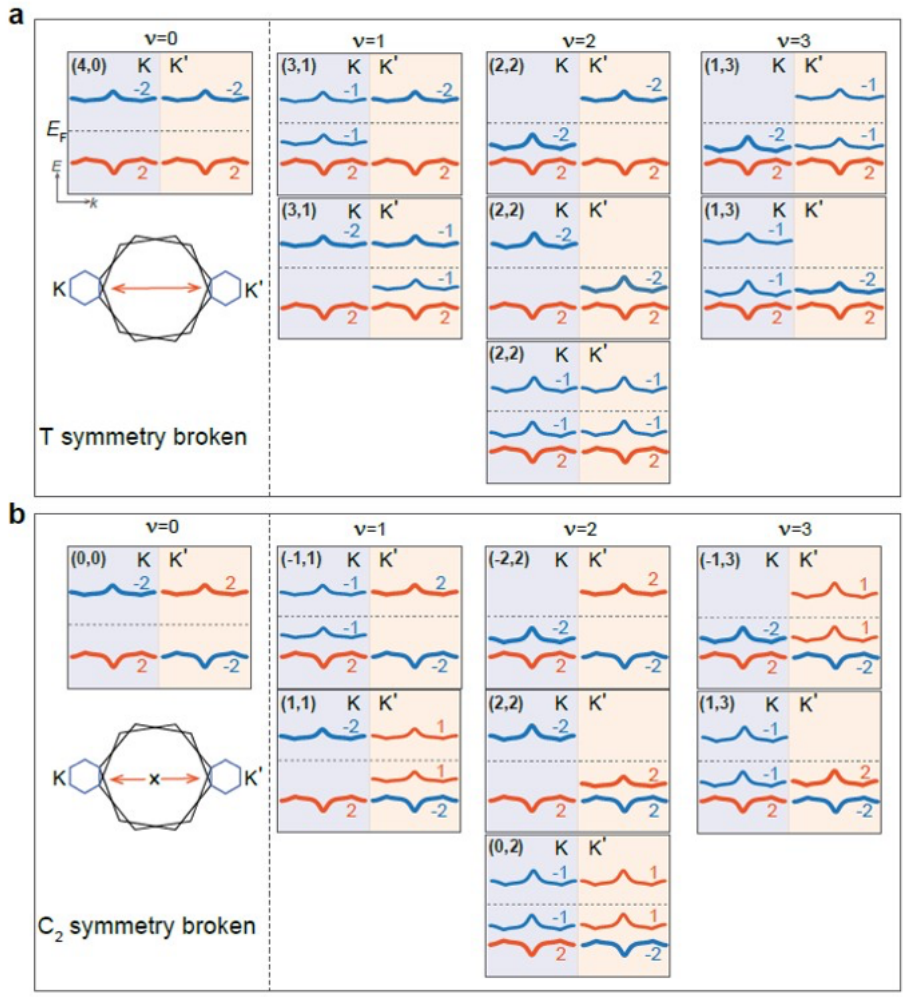

Fig. 4.11: Different scenarios for broken C2 and T symmetry at different integer fillings. **(a)** Possible Chern states at all the integer filling when time reversal T symmetry is broken but C2 is preserved at $\nu = 0$. Our physical observable at $\nu = 0, 1$ come under this scenario. **(b)** Chern states at all integer filling when C2 is broken but time reversal symmetry T is preserved.

measured the Chern states at several temperature starting from T = 20 mK till 10 K at different magnetic fields. Upper panel of Figure **(a), (b), (c), (d)** are the plot of R_{xx} as a function of filling factor ν at 6 T for the Chern states (4,0), (3,1), (2,2), (1,3). We have observed that the R_{xx} goes to zero because of the quantization of the state. Lower panel is the transverse conductivity σ_{xy} as a function of filling factor ν. We calculated the gap of all the Chern states from the temperature activation behavior, $R_{xx} \sim e^{-\Delta/kT}$ at 6T. Figure **(e)** is the longitudinal resistance R_{xx} in logarithmic scale as a function of inverse temperature ($1/T$). By the Arrhenius fitting (shown in the corresponding dotted straight lines) we have calculated the gaps for each Chern state. Strikingly, these gaps $\Delta(4,\ 0)$ = 11.2K, $\Delta(3,\ 1)$ = 7.1 K, $\Delta(2,\ 2)$ = 10.4 K, $\Delta(1,\ 3)$ = 4.4K are much higher than the typical Landau gaps in MATBG. This allows us to disentangle Chern states from typical Landau levels in the system.

In this chapter, we have discussed a detailed view of the high magnetic field phase diagram of MATBG and demonstrates its underlying topology and symmetry. The topological nature of the flat bands in MATBG observed in this study has implications for the potential understanding of the superconducting phase, which needs to be understood on the basis of the ground states found here. To further comprehend the microscopic mechanisms driving the CCI and interactions between the various quantum states (CCI, superconductor and orbital magnet), one possible direction is to control the correlated states by inducing dielectric screening or spin–orbital coupling in higher-quality devices in further experiments.

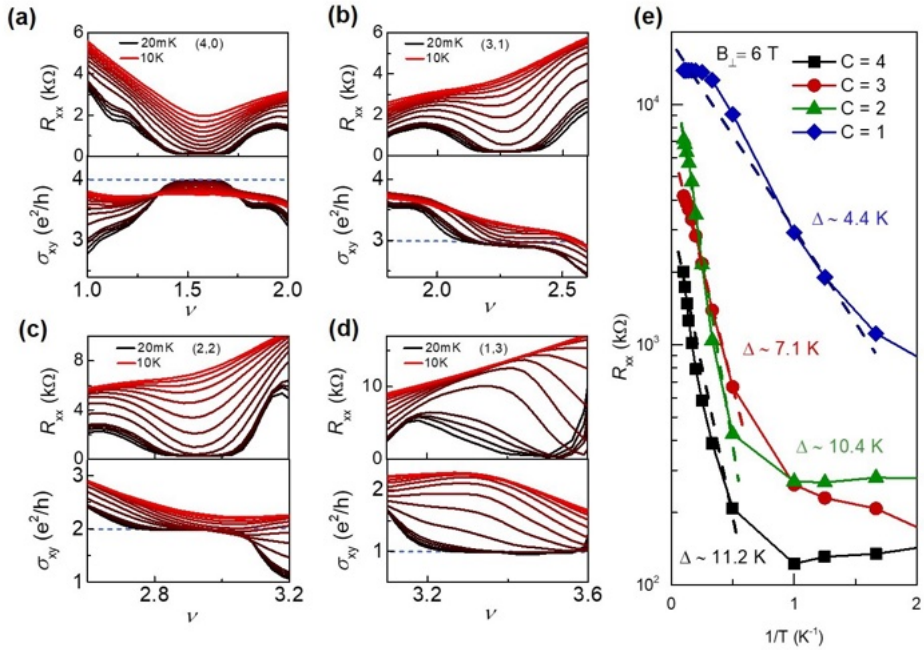

Fig. 4.12: Temperature dependence and gap extraction for all the Chern insulators. **(a), (b), (c), (d)** upper and lower panels shows the longitudinal resistance, R_{xx} and transverse conductivity σ_{xy} of the Chern insulator (4,0), (3,1), (2,2) and (1,3) as a function of ν taken at several temperatures. Lower panel corresponds to the quantization of σ_{xy} below 600mK. **(e)** Extraction of gap for all the Chern insulators. Longitudinal resistance R_{xx} is plotted as a function of inverse temperature $(1/T)$ at 6T. The data is measured for device A1

Chapter 5

Flat Bands at High Magnetic Field

In the previous chapter, we have discussed an important emerging phenomena in magic angle twisted bilayer graphene while placed in an external magnetic field. However all the results were restricted upto a field of $B = 8$ T. In this chapter, we will discuss the detailed magneto-transport behaviour of the flat band of MATBG while placed in an unprecedented high magnetic field upto $B = 34$ T. The high magnetic field creates a fractal electronic phenomena called Hofstadter butterfly in a moiré superlattice system. Although people have studied the magnetic field dependent phenomena in MATBG for a few years, high magnetic field behaviour was unexplored before.

Previous studies of the electronic properties of graphene–hexagonal boron nitride (hBN) superlattices in the presence of high magnetic field have provided great insight into the Hofstadter spectrum. However, flat electronic bands with strong correlation and non-trivial topology have never been explored in this light before. Together, these phenomena make MATBG an interesting platform to study Hofstadter spectrum enriched with band topology and strong interaction.

In the first section of this chapter, we will describe the basic physics of the Hofstadter butterfly in any superlattice system. Then we will discuss the Hofstadter spectrum of MATBG in detail and report the observation of re-entrant flat electronic bands at one magnetic flux per moiré unit cell.

5.1 Hofstadter butterfly in the flat band of MATBG

Electrons develop a discrete quantized energy spectrum while moving in a spatially varying periodic lattice potential. Additionally, in two dimensions, when moving under a perpendicular magnetic field, electrons develop a quantized energy spectrum, characterised by discrete energy levels, called Landau levels. As a result, two dimensional electrons when placed under both magnetic field and a periodic lattice potential generate a recursive energy spectrum, called the Hofstadter spectrum. This complex energy spectrum results from the interplay between two characteristic length scales associated with periodic lattice potential and the magnetic field. The Hofstadter butterfly energy spectrum was the first quantum fractal spectrum discovered in physics.

Even though it was theoretically predicted by Douglas R. Hofstadter back in 1976, experimental efforts have always been limited by the commensuration of two length scales in real systems. The periodicity in typical atomic lattices is of the order of few angstroms, which would require a magnetic field of $\sim$ kT to fulfill the commensurability condition. On the other hand, artificially engineered materials (periodicity of hundreds of nanometers) require a magnetic field that is too small to overcome the disorder completely.

Many experimental efforts have been made to create superlattices which can achieve the commensuration condition within an affordable limit. One of the successful approaches was the moiré superlattice of graphene and hBN in 2013. In this section, first we briefly introduce the concept of the Hofstadter butterfly, including the theoretical model of Bloch electrons in the magnetic field, the resulting Harper's equation and its solution, and its realizations in non-graphene systems. Then, we discuss the ways to realize the fractal Hofstadter spectra in graphene, and introduce three types of graphene superlattice structures, including graphene/hBN, twisted graphene layers and nano-fabricated graphene superlattices. In particular, the details of the fractal Hofstadter spectrum in graphene will be discussed extensively for the graphene/hBN superlattice and the twisted bilayer graphene. In the end we will talk about the motivation of our work and the special features of the spectrum in MATBG that reveals a qualitatively new Hofstadter spectrum, which arises due to the strong electronic correlations in the re-entrant flat bands.

5.1.1 Hofstadter butterfly in moiré superlattice

In his seminal paper in 1976, D. R. Hofstadter considered the Bloch periodic energy function to be,

$$W\left(\overrightarrow{k}\right) = 2E_0(\cos k_x a + \cos k_y a) \tag{5.1}$$

where E_0 is an empirical parameter, λ is the period of the lattice potential and $\mathbf{k}$ is the wave vector. The momentum was then replaced by the Peierls substitution as,

$$\hbar\mathbf{k} \rightarrow \hbar\mathbf{k} - e\mathbf{A} \tag{5.2}$$

where e is the electron charge and $\mathbf{A}$ is the magnetic vector potential with $\mathbf{B} = \nabla \times \mathbf{A}$. By solving the time independent Schrödinger's equation, we get the wave function to be,

$$\Psi(x, y) = g_n e^{i\alpha m} \tag{5.3}$$

with $x = n\lambda$ and $y = m\lambda$ where m, n are integers and α depends on the energy. The Harper's equation is given by,

$$g_{n+1} + g_{n-1} + 2\cos(2\pi n\Phi/\Phi_0 - \alpha)g_n = \epsilon g_n \tag{5.4}$$

where $\Phi = B\lambda^2$ is the magnetic flux through the moiré unit cell, $\Phi_0 = h/e$ is the magnetic flux quantum and $\epsilon = 2E/E_0$ with energy E. At rational fillings with $\Phi/\Phi_0 = p/q$, where p and q are co-prime integers. The solution of the Harper's equation reveals that the Bloch band would split into q distinct energy sub-bands, resulting in a recursive fractal energy diagram as shown Figure 5.1**(b)**, the so called Hofstadter butterfly.

In 1978, G. Wannier included the density of states of the system into the picture and transferred the fractal energy spectrum into a linear diagram, the so-called Wannier diagram. In this representation, Hofstadter's butterfly is described by the Diophantine equation, given by,

$$n/n_0 = t(\Phi/\Phi_0) + s \tag{5.5}$$

where n is the carrier density and n_0 is the carrier density of a unit cell. The first quantum number t corresponds to the topological properties of the Landau level flat band and the second quantum number s is the Bloch band filling index. Later on, the fractal spectrum was also calculated for triangular lattices [73] and honeycomb lattices [74].

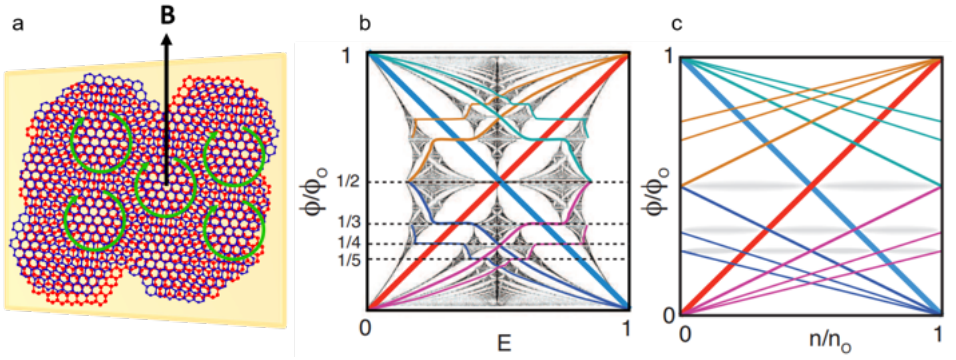

Fig. 5.1: Hofstadter spectrum and Wannier diagram. **a** Schematics of moiré superlattice and electron's motion in 2D under a perpendicular magnetic field B. **b** Calculated Hofstadter spectrum in a unit cell. **c** Wannier diagram produced from the Hofstadter spectrum.

Hofstadter spectrum in different systems

The minigaps in this fractal spectrum are considerable when the magnetic flux passing through the unit cell is comparable to the quantum flux or, in other words, the magnetic length l_B is comparable to the λ, the period of the lattice potential. Earlier people had fabricated lateral superlattices of 2D electron gas in GaAs/AlGaAs heterostructures to study this physics [75–77]. Although some signatures of the Hofstadter spectrum were observed in this system, the sample degradation due to nanofabrication and the difficulty of tuning the carrier density continuously hindered the complete reveal of the fractal energy spectrum.

The fractal Hofstadter spectrum was vividly realized in a microwave waveguide with a periodic arrangement of scatterers [78]. In this photonic system, the transmission matrix mimics the Hamiltonian of Bloch electrons in a magnetic field, and equivalently leads to the Harper equation and a fractal Hofstadter butterfly. Similar realizations of the Hofstadter Hamiltonian were also reported in optical lattices with ultracold atoms [79] and in superconducting qubits [80].

Being atomically thin, graphene provides an ideal platform to study 2D electronic phenomena. The first and the best experimental observation of the fractal phenomena was observed in a graphene/hBN superlattice due to their lattice mismatch. The fractal Hofstadter spectrum was realized in transferred graphene/hBN superlattices [53, 81–

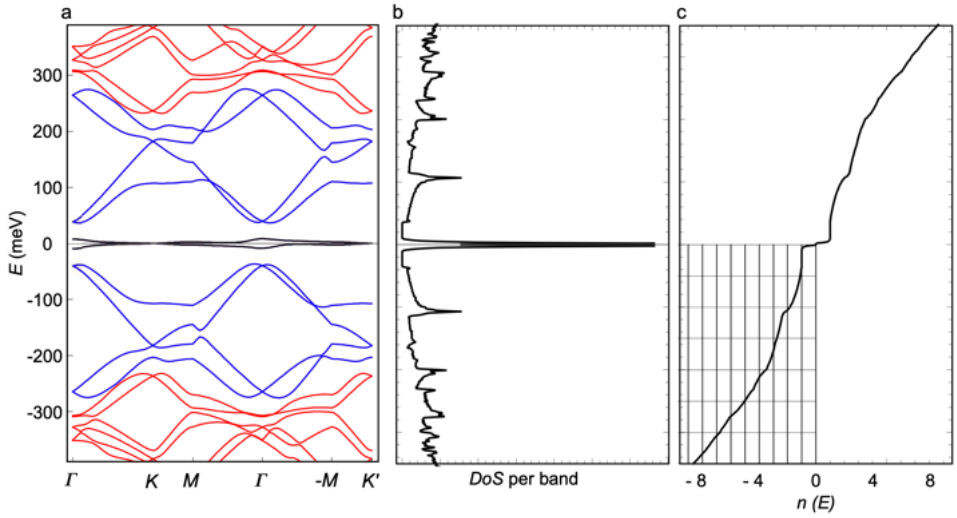

Fig. 5.2: BM model with common energy (E) axis. **(a)** The single-particle bands of the BM model for $\theta = 1.12°$ in zero flux. The nearly flat bands at charge neutrality are black, the lowest four connected passive bands are blue, and the sixth and higher bands are red. **(b)** Normalized density of states (arbitrary units). **(c)** Integrated DoS or filling $n(E)$ as a function of the energy. The 50 meV hatching in the bottom left corner is for visual ease of comparison with energies at integer filling of the bands. The filling is reported without the spin-valley degeneracy, so $n = 1$ corresponds to $\nu = 4$.

85], in epitaxial graphene/hBN superlattices [86], and in ABC-trilayer graphene/hBN superlattices [87].

Hofstadter spectrum in MATBG

Twisted bilayer graphene is an interesting and even more complicated system to study the fractal phenomena as it not only determines the period of the superlattice but also dictates the inter-layer coupling. Nesr the magic angle ($\theta = 1.1°$), electronic bands are extremely flat with a thickness of $\sim$ 10 meV with a strong correlation. The moiré unit cell period for magic angle is ($\sim$ 15 nm) such that one magnetic flux quantum per moiré unit cell ($\Phi/\Phi_0 = 1$) can be achieved around $B = 30$ T.

Here, we discuss the single particle spectrum of twisted bilayer graphene in a magnetic field computed using the Bistrizter-MacDonald

model. For completeness, we include the zero-magnetic field spectrum in Figure 5.2**(a)**, where we highlight the two flat bands near zero energy (black) and the four lowest passive bands above and below charge neutrality (blue). Figure 5.2**(b)** and **(c)** show the density of states (DoS) and filling $n(E)$ respectively. We compare some features of the low magnetic field resistance data to the zero flux band structure which can be understood from a Landau level approximation of the $k \cdot p$ spectrum. However in larger fields, a full Hofstadter calculation is necessary to determine the spectrum and topology.

The band structure of the BM model in 2π magnetic flux per unit cell was calculated in [88], where the authors developed a gauge-invariant formalism to study the single-particle spectrum, topology, and interacting states. By employing a judicious choice of basis states that are eigenstates of both magnetic translation operators (which commute at 2π flux), they were able to block-diagonalize the continuum Hamiltonian by momentum, allowing for calculations of band structures and Wilson loops. The momentum basis states at flux $\Phi = 2\pi$ read,

$$\Psi_{k,m}(r) = \frac{1}{\sqrt{N(k)}} \sum_{R_1,R_2 \in Z} e^{-ik\cdot R} T_1^{R_1} T_2^{R_2} w_m(r) \tag{5.6}$$

with the commutation relations,

$$T_1 T_2 = e^{i\Phi} T_2 T_1 \quad \text{and} \quad [T_1, H] = [T_2, H] = 0 \tag{5.7}$$

Here k is momentum and r is position, $w_m(r)$ is the wavefunction for the mth Landau level centered at the origin, and T_1, T_2 are the magnetic translation operators. Notably, the magnetic translation operators T_i commute at $\Phi = 2\pi$. So just like at zero field the spectrum is diagonalized into Bloch-like bands with density one electron per moiré unit cell. The mth momentum basis states are in essence linear combinations of the mth Landau level translated by all lattice vectors R, and appropriately normalized by $N(k)$. When expressed in this basis, the Bistritzer- MacDonald model in 2π flux becomes a relatively simple Hamiltonian involving ratios of Jacobi theta functions. The Landau level index m is chosen to range from 0 to n_{landau}, the Landau level cutoff. Increasing n_{landau} improves the accuracy of the eigenvalues and eigenvectors.

To treat twisted bilayer graphene at rational flux $\Phi = 2\pi p/q$, where p and q are co-prime integers, one may map the rational flux Hamilto-

nian to a 2π flux Hamiltonian by a redefinition of the lattice vectors, shrinking one lattice vector by a factor of p (at the cost of the Hamiltonian no longer being translation symmetric with respect to this smaller lattice vector) and extending the other by a factor of q. This modified unit cell encloses 2π flux, and so the results of [88] may be applied with only minor modifications. It is important to note that the resulting Hofstadter sub-bands have lower density. They have one electron per q moiré unit cells.

Because the Hamiltonians are block-diagonalized by momentum, they are relatively small in dimension, although the Hamiltonians are dense. It is not numerically taxing to build a large Hofstadter spectrum reaching as high as $q = 40$, with p ranging from 1 to q. Each Hamiltonian for a given momentum has dimension $\approx 4pn_{landau} \times 4pn_{landau}$, where n_{landau} is the Landau level cutoff. Even for small n_{landau}, for example 50, we find the gauge-invariant rational flux technique works very well and is quite accurate for most values of Φ. It is only for high q that the Hamiltonian loses accuracy, requiring an increase in n_{landau} to compensate. The Hamiltonian is diagonalized over a mesh of points in the magnetic Brillouin zone, yielding a Hofstadter spectrum. We neglect the Zeeman splitting, which is less than 2 meV.

Gaps in the Hofstadter spectrum correspond to single particle insulating states. Unlike 0 and 2π flux, at rational flux single-particle gaps occur also at fractional fillings. To see this, note that at rational flux $\Phi = 2\pi p/q$, the magnetic translation operators T_1, T_2 do not commute with one another. However, the operators,

$$[T_1, T_2{}^q] = 0 \quad \text{and} \quad [T_1, H] = 0 \quad \text{and} \quad [T_2{}^q, H] = 0 \tag{5.8}$$

do commute, implying the Hamiltonian can be diagonalized in a magnetic unit cell enlarged by a factor of q. Thus the magnetic Brillouin zone is reduced by a factor of q. At 0 and 2π flux, a filling of $\nu = 4$ (4 for spin and valley degeneracy) implies that one band is completely filled. At rational flux, a filling of $\nu = 4$ fills q Hofstadter bands; this is because the Brillouin zone is smaller, so a higher numbers of bands are filled to have the same electron density. We searched the Hofstadter spectrum for gaps greater than our chosen cutoff of 6 meV and selected those that occurred at precisely an integer number of Hofstadter bands away from charge neutrality.

5.2 Magneto-transport behaviour at high magnetic field

The moiré potential in MATBG gives rise to a set of renormalized flat bands in the mini Brillouin zone. These flat bands possess C_{2z}, C_{3z}, C_{2x} rotational symmetries and time reversal symmetry ($\mathcal{T}$) at zero magnetic field. At zero magnetic field, nontrivial band topology exists due to the $C_{2z}\mathcal{T}$ symmetry in the system. The specific symmetry and topology of the bands plays a great role in understanding the different emergent quantum phases in MATBG [89–91]. Hence, discovering novel flat band systems with different inherent symmetries has been a major goal in this field. As we discussed in the last section, at 2π magnetic flux, MATBG possess a set of new flat bands with different band topology and symmetry. In this section we will discuss the observation of flat band and related phenomena in detail at 2π magnetic flux.

5.2.1 Re-entrant correlated insulator at 2π magnetic flux

We measured the magneto transport behaviour of a magic angle device with a twist angle $\theta = 1.12° \pm 0.02°$ at a magnetic field as high as $B = 31$ T. The magnetic field (B_0) required to reach the full flux condition is given by,

$$B_0 = \frac{h}{e} \times \frac{1}{A} \tag{5.9}$$

where A is the unit cell area of the moiré superlattice, h is the Planck's constant and e is the electronic charge. For our device with the twist angle, $\theta = 1.12°$, the corresponding B_0 is 30.5 T. We studied the full Hofstadter spectrum from zero filed to B_0 in order to resolve the evolution of the flat band at different integer flux. At B_0 we observed re-entrant correlated insulators at certain integer fillings which are almost similar to the zero field correlated insulator. In this section we will discuss the characteristics of the re-entrant insulators in the presence of magnetic field and temperature.

Figure 5.3**(a)** represents the four terminal longitudinal resistance R_{xx} as a function of magnetic field B and filling factor ν. The carrier density n of the flat band is continuously tuned by the gate voltage

V_g applied to the graphite gate. Total carrier density of the band n is normalized by $n_S = 4n_0$, where n_S is the density of the fully filled spin and valley degenerate moiré bands and n_0 is the density per flavour. In this picture, the filling factor of the band ν is given by $\nu = n/n_0$.

In the $\nu - B$ phase space, dark red regions correspond to highly resistive states and dark blue regions correspond to low or zero resistive states. It demonstrates the continuous evolution of different states in the presence of the magnetic field. At zero magnetic field, the flat band hosts several correlated insulators (CI) at the integer fillings of $\nu = +2, +3, -2$ and band insulators (BI) at $\nu = \pm 4$ as observed in other studies as well. Another dark red region at $\nu = 0$ corresponds to the charge neutrality point (CNP) of the flat band.

As we keep increasing the magnetic field, all the correlated insulators start to become weaker and finally around $B \sim 8$ T, all of them completely disappear. This trend of the correlated insulators has been observed in multiple studies before. As we apply much higher magnetic field, the phase space is mostly dominated by the Landau levels emerging from different integer fillings, which we will discuss later. Strikingly, above $B = 24$ T, the CIs at $\nu = +2, +3$ reappear and grow continuously stronger until $B = 31$ T (Φ_0). While we could not measure the device at a B field well above Φ_0, due to experimental limitations, by continuity, all the CIs remain symmetric with respect to Φ_0 and behave similarly below Φ_0. Hence, in this study we will always discuss the phase space below Φ_0.

In this colour plot, R_{xx} contains more noise than low magnetic field phase space data. It happens due to the unstable device contacts at high magnetic field. The instability arises due to several factors at high magnetic field, such as,

1. In our final device structure, only the effective device channel is gated by the local graphite gate. However, there are some parts of the device which connect to the metal electrodes that are out of the graphite gate. The resistance of these parts contributes to the contact resistance of the device. In general the contact resistance ($R_c \sim 10k\Omega$) of the twisted bilayer graphene devices is an order of magnitude higher than normal graphene devices due to the flat band formation. With increasing magnetic field, the contact resistance increases due to the increase of CNP resistance of twisted bilayer graphene. For some devices, we have observed a contact resistance of $\sim 10M\Omega$ at a magnetic field above $B = 15$T.

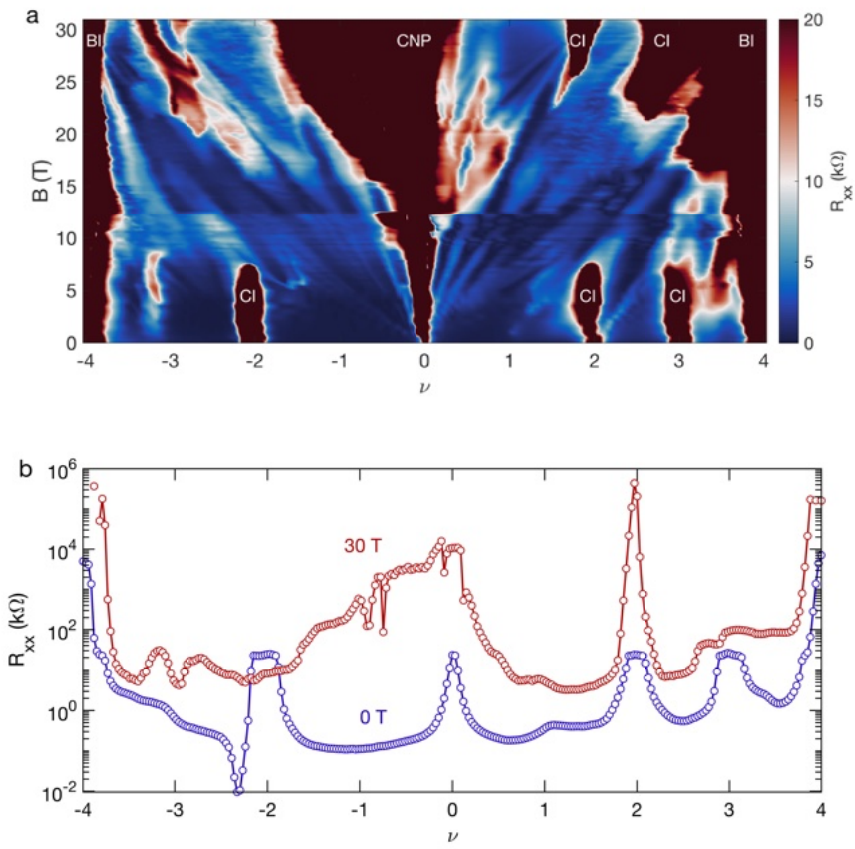

Fig. 5.3: Longitudinal resistance of the device at high magnetic field. **(a)** Color plot of the R_{xx} as a function of magnetic field B and carrier density ν. CI represents the correlated insulators and BI corresponds to the band insulators, CNP defines the position of the charge neutrality point. **(b)** Line plot of R_{xx} inside the flat band at $B = 0$ T and $B = 30$ T showing the high resistance peaks of correlated insulators at $\nu = +2$.

In this situation, it becomes almost impossible to bias the device with constant current.

To improve the contact resistance we have always applied a constant global silicon gate voltage in our devices for all the measurements at high magnetic field. The application of the global gate voltage brings the contact resistance far away from the CNP into the metallic region. The resistance of these parts generally does not increase with increasing magnetic field, thus making it more stable.

2. Another source of noise is the mechanical vibration at high magnetic field which incorporates electrical noise in our measured data. When we are operating above $B = 15$ T, the current passing through each coil of the magnet is of the order of tens of Mega Ampere ($10^6 - 10^7$ A) which also produces a lot of heating effect in the circuit. Although there are powerful water cooling systems, it is almost impossible to avoid the mechanical vibration while working at high magnetic field. Hence, we could not completely get rid of the electrical noise in our measurement.

Figure 5.3**(b)** represents the line plot of R_{xx} as a function of ν at $B = 0$ T and $B = 30$ T (full flux) at $T = 40$ mK. The $B = 0$ T trace is dominated by a well-known sequence of resistance peaks [26, 92]. The charge neutrality point (CNP) appears to be a gapless phase since R_{xx} is of the order of $10k\Omega$. We observed correlated insulators (CI) at $\nu = \pm 2, +3$ and band insulators (BI) at $\nu = \pm 4$. We have also observed a superconducting region (SC) near $\nu = -2$. In the $B = 30$ T trace, we observe an overall similar picture, which strikingly shows enhanced resistance peaks at $\nu = +2 + 3$: a first indication of re-entrant CIs. We will discuss the temperature dependence of these states in the later section. Nevertheless, some differences emerge. The CNP is now gapped with a resistance in the order of $R_{xx} \sim 10$ MΩ, and the gaps of the BIs at $\nu = \pm 4$ are enhanced. We also do not find signatures of superconductivity. We argue that the experimental parameters to observe SC are much more stringent than those for the observation of the CIs.

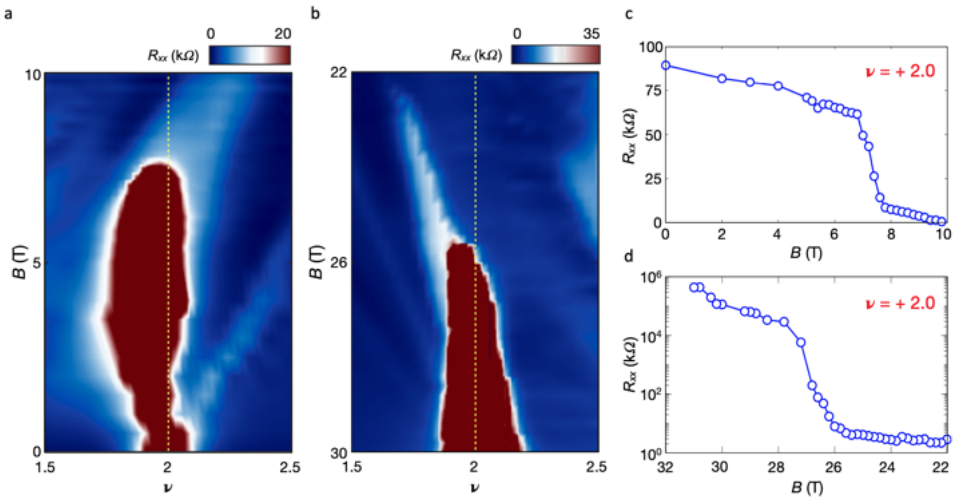

Fig. 5.4: Magnetic field dependence of the correlated insulators. **(a)** Color plot of the R_{xx} as a function of magnetic field B (upto B = 10 T) and carrier density ν. **(b)** Color plot of R_{xx} as a function of magnetic field B (from B = 30 T to 22 T) and carrier density ν close to full flux. **(c)** Evolution of the CI with magnetic field ranging from B = 0 T to 10 T. **(d)** Evolution of the $\nu = +2$ state with magnetic field near Φ_0. R_{xx} is plotted in logarithmic scale.

5.2.2 Magnetic field dependence of the correlated insulator

In this section, we will discuss the effect of perpendicular magnetic field on correlated insulators. As mentioned earlier, perpendicular magnetic field suppresses the resistance of the correlated insulator. As shown in Figure 5.4**(a)**, the correlated insulator at $\nu = +2$ CI is completely suppressed by a perpendicular magnetic field of $B = 8$ T. Figure 5.4**(c)** represents the line plot of R_{xx} as a function of B at $\nu = +2$ from B = 0 T to B = 10 T. The graph clearly describes that the CI is the strongest at zero field and it decreases almost linearly with increasing magnetic field. Finally, at $B \sim 8$ T, the resistance jumps from 75 kΩ to 5 kΩ and $\nu = +2$ state becomes a metallic state.

We observed qualitatively similar feature at the same filling, close to the full magnetic flux. Figure 5.4**(b)** is the colour plot of R_{xx} close to $\nu = +2$ and $\Phi = 2\pi$ from B = 22 T to 30 T. The highly resistive state visibly fades upon lowering the magnetic field away from the flux quantum Φ_0 = 31 T. R_{xx} has a maximum value at B = 31 T,

decreases with magnetic field, and finally obtains high conductance at $B = 26$ T as shown in Figure 5.4**(d)**. This same qualitative trend of the correlated insulator at $\nu = +2$ for both zero flux and Φ_0 suggests the two correlated insulators possess a similar origin. Due to experimental limitations, we could not apply an external magnetic field higher than Φ_0 or $B = 31$ T. Hence we have compared it with the CIs at lower magnetic field.

5.2.3 Temperature dependence of the correlated insulators

In the previous section, we have only discussed the magnetic field dependence of the $\nu = +2$ state and qualitatively assigned the state to be a correlated insulator. However, one of the most important feature of the correlated insulator is the temperature dependence. The temperature activated gaps of the correlated insulators at zero magnetic field are generally much smaller than the band insulating gaps. We have also measured the temperature dependence of R_{xx} at high magnetic field close to Φ_0.

Figure 5.5 summarises the temperature activation of different states inside the flat band, mainly the insulating states at $\nu = +2$ and $+3$ at $B = 28$ T. We plotted longitudinal resistance R_{xx} on a logarithmic scale as a function of filling factor ν for eight different temperatures ($T = 1.5$ K, 3 K, 4 K, 5 K, 7.5 K, 10 K, 12.5 K and 15 K) in Figure 5.5**(a)**.

The resistance (10 kΩ) of the device is much higher than the zero-field resistance, even in the metallic region of the flat band. This happens due to the higher contact resistance and the non-ideal 4 probe configuration of the device at high magnetic field. The resistance of the CNP is $\sim 10^6$ kΩ, indicating a gap opening. Apart from that, the resistance of the $\nu = +2$ state increases by one order of magnitude and the resistance of the $\nu = +3$ state becomes double by decreasing the temperature from $T = 15$ K to 1.5 K.

In order to calculate the size of these temperature activated gaps, we plotted the conductance (G_{xx}) in logarithmic scale as a function of $1/T$ for $B = 28$ T. The turquoise line plot is the temperature activation of $\nu = +2$ state and the neon pink is for $\nu = +3$ state. By doing Arrhenius fitting on this curve, we calculated that the gaps are $\Delta = 0.85$ meV and $\Delta = 0.17$ meV for $\nu = +2$ and $\nu = +3$ states,

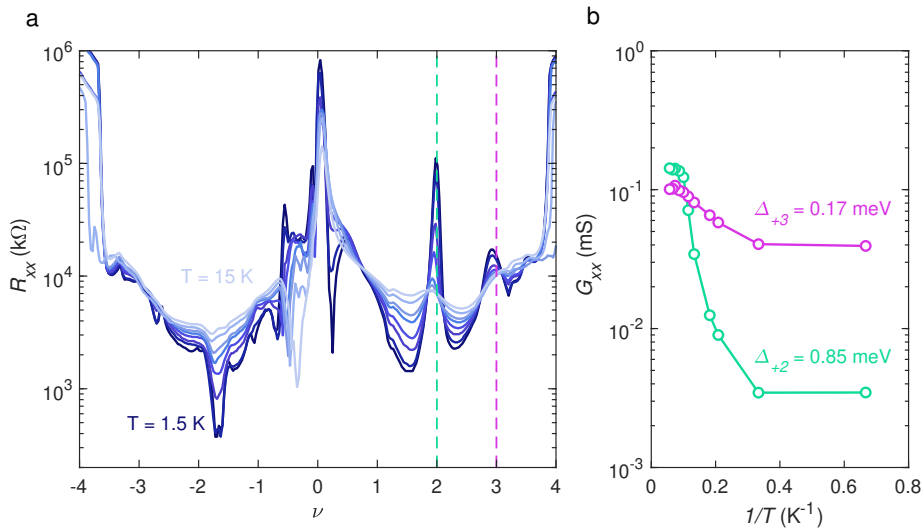

Fig. 5.5: Temperature dependence of the correlated insulators at B = 28 T. **(a)** R_{xx} as a function of ν in logarithmic scale at several temperatures from T = 1.5 K to 15 K. ν = +2 and +3 states are marked with dotted turquoise and neon pink lines respectively. **(b)** Conductance G_{xx} as a function of $1/T$ for ν = +2 and +3 states.

respectively.

5.2.4 Degeneracy of the flat band at one magnetic flux

Theoretically, it has been predicted that the flat band at one magnetic flux of the unit cell has different band symmetries and topology. At zero magnetic field, the band has four fold symmetry (spin and valley) at the CNP. However, this degeneracy is lifted at the half filling of the band due to the correlation. This results in a Chern insulator with Chern number $C = 2$ from the integer filling $\nu = \pm 2$. This scenario might differ as we increase the magnetic field and reach one magnetic flux per moiré unit cell.

In this section, we will discuss the emergence of the Chern insulator from the re-entrant correlated insulator at full flux. Figure 5.6**(a)** represents the colour plot of R_{xx} as a function of the magnetic field (B) from zero field to full magnetic flux and around the half filling

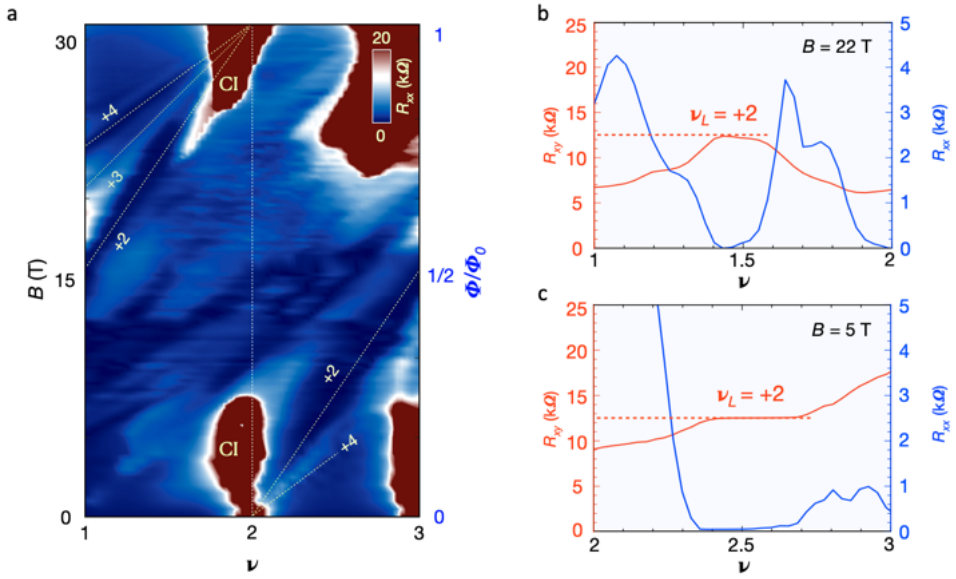

Fig. 5.6: Evolution of the LL from the flat bands at both zero flux and one magnetic flux. **(a)** Colour plot of R_{xx} as a function of ν and B measured around $\nu = 2$ at 40 mK. **(b)** and **(c)** R_{xx} and R_{xy} as a function of ν at $B = 22$ T and $B = 5$ T respectively, showing the full quantization for the $\nu_{LL} = +2$ LL gap.

of the flat band. At zero magnetic field we observed a set of Landau levels with filling factors $\nu_L = +2, +4$ emerging from the CI at $\nu = 2$. In previous studies, including ours, the LL with ν_L has been recognized as correlated Chern insulator with the Chern number $C = 2$. We have plotted both longitudinal resistance (R_{xx}) and transverse resistance (R_{xy}) close to $\nu = 2$ at $B = 5$ T in Figure 5.6**(c)** to show the quantization of this state. This shows clear quantum Hall signatures of $\nu_L = +2$ with $R_{xx} \sim 0\ \Omega$ and $R_{xy} \sim 12.5\ \text{k}\Omega$. We have used the magnetic field symmetrization technique of resistance to get the perfectly quantized states.

The nano-fabrication process always incorporates some misalignment in the Hall bar geometry of the MATBG devices. At a very high magnetic field this misalignment of the probes becomes a dominating factor and incorporates cross contribution to the longitudinal (R_{xx}) and Hall (R_{xy}) resistances. This prevents us from getting a perfectly isolated R_{xx} and R_{xy} measurement.

The magnetic field symmetrization technique was used to extract

these values with quantitative precision. Due to the magnetic field symmetrization property, the longitudinal resistances (R_{xx}) are symmetric under time reversal and are the same in positive or negative magnetic field, whereas the Hall resistances (R_{xy}) are anti-symmetric and change sign for positive versus negative magnetic field.

In order to get the exact value of these resistances, we measured the device in both the positive and negative polarities of the magnetic field ($+B$ and $-B$) and calculated R_{xx} and R_{xy} using these formulae:

$$R_{xx}(B) = [R_{meas}(+B) + R_{meas}(-B)]/2 \tag{5.10}$$

$$R_{xy}(B) = [R_{meas}(+B) - R_{meas}(-B)]/2 \tag{5.11}$$

Due to experimental difficulties, we could not measure the device in the negative polarity of magnetic field for the full B space up to B = -31 T. However, we were able to perform measurements for certain values of magnetic field. In Figure 5.6**(b)** and **(c)**, the Hall resistance R_{xy} was anti-symmetrized in order to get perfect quantization at ν_L = +2.

The CI is continuously suppressed with increasing B and vanishes at $B \sim 8$ T, where the phase diagram is dominated by LLs. Strikingly, above $B = 24$ T the $\nu = +2$ CI state reappears and grows continuously stronger up to Φ_0 as shown in Figure 5.6**(a)**. As mentioned above, we could not measure our device in B fields well above Φ_0 due to experimental limitations. However, by continuity, all the LLs that point away from the CNP above B_0, will point toward the CNP below B_0. Similar to zero flux, we also observed the emergence of a set of LLs from the $\nu = +2$ CI. The LLs with even fillings are more pronounced than the odd fillings. R_{xx} and R_{xy} are plotted as a function of ν at B = 22 T, showing perfect quantization in Figure 5.6**(c)**. Since the most dominant LL here is the $\nu_L = +2$, we also interpret this LL to be the correlated Chern insulator with $C = 2$, in direct analogy to the $B = 0$ T case.

5.3 Fermi Surface reconstruction at different integer fillings

In the presence of a superlattice electrostatic potential and perpendicular magnetic field, the two dimensional electron gas (2DEG) gives rise

to a self-similar recursive energy spectrum. In the case of graphene/hBN superlattices, this recursive fractal energy spectrum was observed within an accessible range of magnetic field ($B = 35$ T). Magic angle twisted bilayer graphene exhibits a similar type of behaviour at $B = 31$ T, where one magnetic flux quantum (Φ_0) passes through the moiré unit cell of the superlattice. We have discussed this in the previous section with clear re-entrant features of the correlated insulators. In this section we will present few evidence of the Fermi surface reconstruction at different integer filling of the flat band at 2π magnetic flux, which reconfirms the correlation driven band gap opening at those fillings.

In a metallic system, the Fermi surface is a surface in the reciprocal space which separates the occupied electronic states from the unoccupied states. The shape of the Fermi surface depends on the symmetry of the given lattice. Inside an insulator or a semiconductor, the Fermi level exists within the band gap and the Fermi surface does not exist in this scenario. Hence, in twisted bilayer graphene, the Fermi surface is reconstructed as we cross the mini band gap inside the flat band.

In transport measurements, the electronic Fermi surfaces have been measured by the quantum oscillation under an external magnetic field. This quantum oscillation is called Shubnikov-de Haas (SdH) oscillation and arises due to the Landau quantization. In this section, we will describe the reconstruction of the Fermi surface at high magnetic field, as it passes through different correlation induced mini band gaps.

5.3.1 New set of Landau levels originating from different integer fillings

Previously, we have discussed the re-entrance of the correlated insulators at one magnetic flux quantum per moiré unit cell at integer fillings $\nu = +2$ and $+3$ from the absolute resistance measurements and their temperature dependence. Here we will examine the full $\nu - B$ phase space of the flat band to describe the emergence of new set of LLs from different fillings of the flat band.

Figure 5.7**(a)** and 5.7**(b)** represent the full Landau fan diagrams of R_{xx} and R_{xy} as a function of ν and B for the entire magnetic field range ($B = 0$ T to 31 T). From different integer fillings, we observed a new set of LLs with different degeneracies. The schematics of these LLs have been laid out in Figure 5.7**(c)**.

At zero flux, a set of fully non-degenerate LLs emerge from the

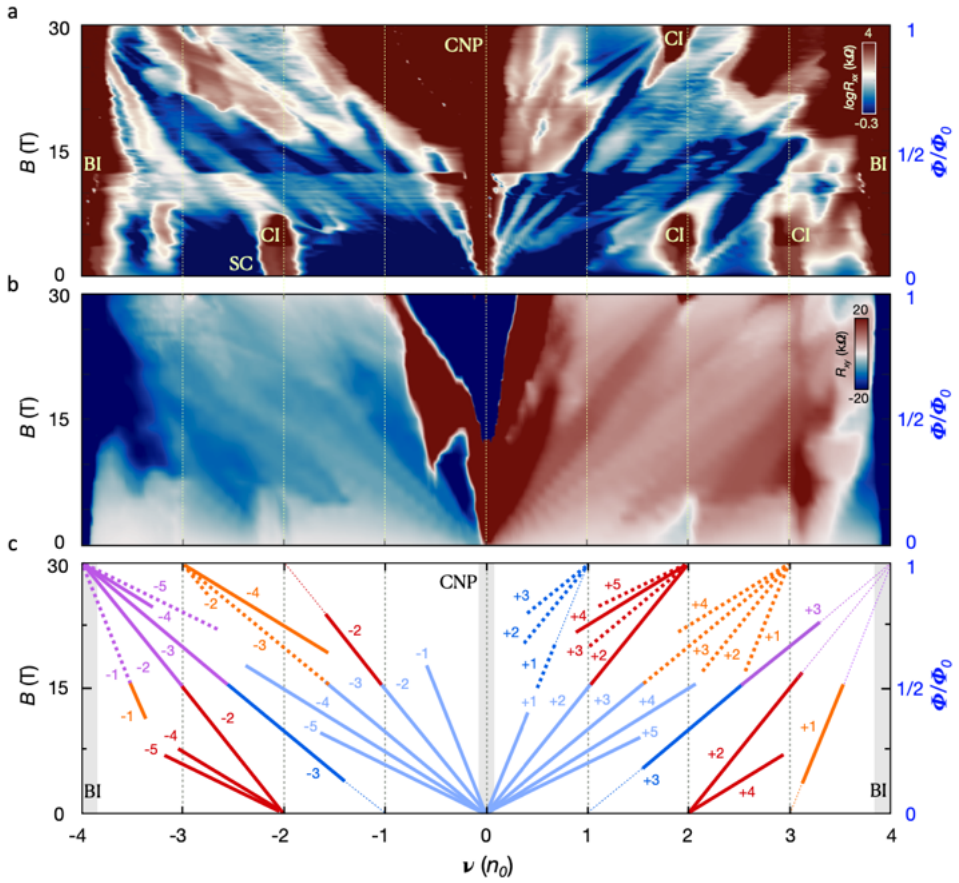

Fig. 5.7: Full phase space of the flat band. (a) and (b) show, respectively, the color plots of R_{xx} and R_{xy} as a function of B and ν, for the full magnetic phase space from $B = 0$ T to $B = 31$ T and ν from -4 to +4. (c) Schematics of all the LLs emerging from different fillings of the band from both zero flux and Φ_0. Light blue lines from the CNP indicate the LLs with $\nu_L = \pm 1$, ± 2, ± 3, ± 4, and ± 5. Dark blue lines indicate the LLs from $\nu = \pm 1$ at both zero flux and Φ_0. Dark red lines correspond to LLs from $\nu = \pm 2$ at both zero flux and Φ_0. Orange lines indicate the LLs that emerge from $\nu = \pm 3$ and purple lines correspond to LLs from $\nu = -4$. Solid lines mark well pronounced, quantized LLs, while dashed lines mark weaker, non-quantized levels.

CNP with the filling factors $\nu_L = \pm1$, ±2, ±3, ±4 and ±5 which are schematically shown in light blue lines in Figure 5.7**(c)**. However, from the half filling ($\nu = \pm2$), we only observed the LLs with degeneracy 2, illustrated in red lines. Interestingly, we have observed only oddly degenerate LLs originating from the odd integer fillings of the flat band. Quarter integer filling ($\nu = \pm1$) of the band gives rise to the LLs with filling factors $\nu_L = \pm3$, as shown in dark blue colours. Likewise, another set of LLs with filling factors $\nu_L = \pm1$ emerge from the 3/4th band filling ($\nu = \pm3$), which are drawn as orange lines in the schematics [34, 47, 68, 93].

At the full magnetic flux ($\Phi/\Phi_0 = 1$), we observed a completely new set of LLs emerging from the different integer fillings of the re-entrant flat band. This observation demonstrates the reconstruction of the Fermi surfaces at those fillings, ν. Surprisingly, all the Fermi surfaces from all the integer fillings have a fully lifted degeneracy. As shown in Figure 5.7**(c)**, we found the LLs with filling factors $\nu_L = +1, +2, +3$ arising from the integer filling $\nu = +1$. This filling at full flux is completely different from the zero field case and has a fully lifted degenerate mini band. $\nu = \pm2$ filling of the band gives rise to the LLs with the filling factors $\nu_L = \pm2$, ±3, ±4 and ±5. Finally, another set of LLs with the sequence $\nu_L = \pm1$, ±2, ±3 and ±4 originated from the filling $\nu = \pm3$. All these levels are schematically drawn with corresponding colours.

This suggests that for both odd and even integers the spin and valley degeneracies have been lifted at Φ_0 in contrast to zero flux. This can be explained by the breaking of $C_{2z}T$ symmetry by magnetic flux, which lifts the degeneracy of the quasiparticles on top of the CIs, although quantitative predictions have not been made so far at odd fillings [94, 95].

Furthermore, we also observed LLs which survive through the full range of magnetic field and connect two different integer fillings at zero flux and at Φ_0. Whereas [88] uses a strong coupling approach to analyze the ground states at Φ_0, more theoretical work is required to study the interactions within the Hofstadter sub-bands at intermediate flux.

The strong interaction at zero flux spontaneously breaks the $C_{2z}T$ symmetry and can give rise to several Chern bands at different odd integer fillings. At Φ_0, the $C_{2z}T$ symmetry is broken by the magnetic field, leading to different single-particle topology in the flat bands and

different degeneracies in the many-body charge excitations atop the CI states. The observed differences in the $B = 0$ T and $B = 30.5$ T LLs reflect the importance of symmetry and topology in determining the many-body phases. The observation of these LLs and the interaction-driven CIs confirms the existence of the (theoretically predicted) flat bands at Φ_0.

5.4 Comparison between the flat bands at high field and at zero field

The flat band in magic angle twisted bilayer graphene at zero field hosts multiple correlated phenomena which have been observed in several studies before. Our study confirms the existence of another flat band at one magnetic flux quantum, with several qualitative similarities. Nevertheless, some differences emerge between the two flat band systems.

Figure 5.3 clearly represents that the zero magnetic field flat band possess a strong superconducting dome at half filling of the band. However, the high magnetic field flat band did not show any superconductor despite having several correlated insulating states. Another stark difference is the size of the correlated insulators at the two different magnetic fields. We will discuss these differences in detail in this section.

5.4.1 Differences between the superconductors

We have observed a strong superconducting dome close to half-filling of the flat bands at zero magnetic field in the hole side. Figure 5.8**(a)** shows the longitudinal resistance R_{xx} as a function of temperature T and filling ν. The dark red region at ν = -2 confirms the well known correlated insulating state at half filling. When the band is slightly doped away from this insulating state, R_{xx} vanishes. The dark blue region (ν = -2.1 to -2.32) in Figure 5.8**(a)** corresponds to the SC dome. The typical temperature dependence of the resistance (R_{xx}) at the optimal doping of the SC dome (ν = - 2.26) shows a clear transition to a zero resistance state. In Figure 5.8**(b)** we calculated the transition temperature to be $T_c = 2$ K. Figure 5.8**(c)** shows the typical d.c. IV measurement of the superconductor. It has a very high

critical current, $I_c = 400$ nA, at the base temperature of our fridge ($T = 40$ mK) indicating the high quality of the device.

We also discuss the possibility of re-entrant superconductivity at Φ_0 flux, which we have not observed in this study even though the device possesses a superconducting region on the hole doped side of the $\nu = -2$ CI at $B = 0$ T. While the exact nature of superconductivity in MATBG is still not clear, it is established that the ultra-high density of states in the flat bands is a key ingredient for its occurrence, and some theories tie it directly to the CI states. In direct analogy to the re-entrant

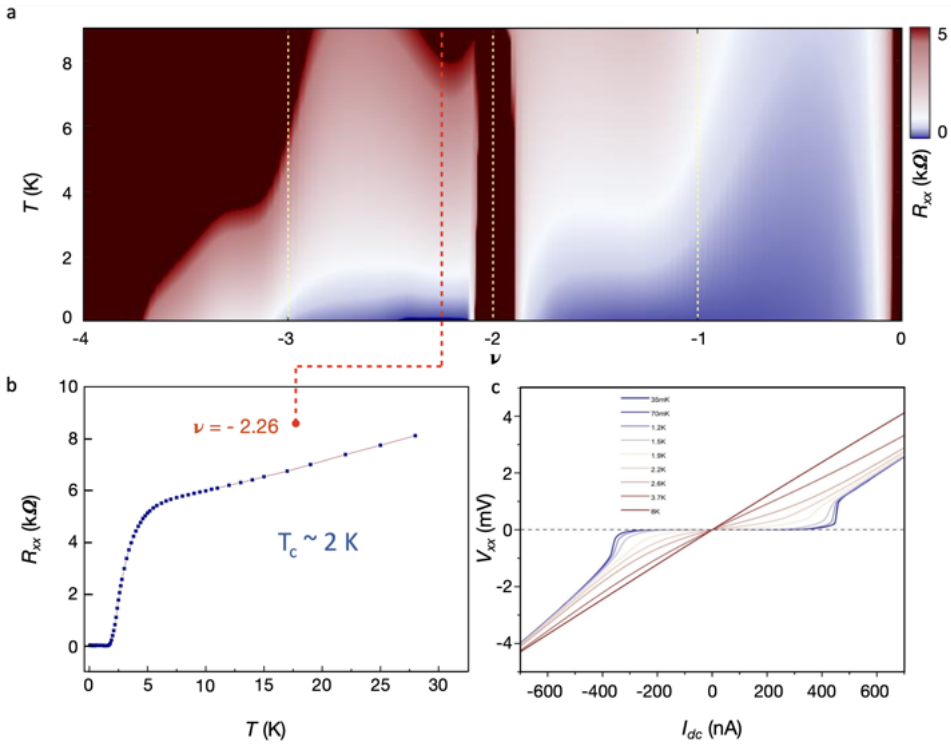

Fig. 5.8: Superconductivity at zero field. **(a)** Temperature dependence of R_{xx} as a function of ν for the hole side of the flat band. The dark red regions at $\nu = 0$, -2, -4 correspond to the charge neutrality point, a correlated insulator, and a band insulator, respectively. The dark blue region left of $\nu = -2$ shows the superconducting dome. **(b)** R_{xx} as a function of T for the optimal doping of the SC at $\nu = -2.26$, yielding a critical temperature $T_c = 2$ K. **(c)** DC current versus voltage plots for the SC at different temperatures from $T = 35$ mK to 8 K.

behavior of the CI, it is possible that the flat bands in full flux could host re-entrant SC phases. However, the experimental parameters for its observation might be much more rigid than for the CIs. As the critical B-field of the SC is only about $B_c \sim 50$ mT, it is several orders of magnitude smaller than that for the CIs, and achieving such measurement accuracy at such high fields is challenging. Such a small field can also be easily smeared out by twist-angle disorder, where at full flux a tiny twist angle inhomogeneity of $\triangle\theta = 0.05°$ will give rise to a variation of the full flux value by $\triangle B = 60$ mT, which is enough to fully suppress a SC state. We hence propose the continued exploration of re-entrant SC in MATBG with ultra-homogeneous devices.

5.4.2 Differences between the correlated insulators

At zero magnetic field, we have clearly observed correlated insulators at $\nu = \pm 2, +3$. We have characterized the temperature dependence of these states and calculated the activation gap from Arrhenius fitting. Figure 5.9**(a)** shows the conductance (G_{xx}) of the $\nu = +2$, +3 and -2 states, as a function of $1/T$ at zero magnetic field.

From the Arrhenius fitting, we calculated their gaps to be $\triangle = 0.22$ meV ($\nu = +2$), 0.09 meV ($\nu = +3$) and 0.21 meV (ν = -2) respectively. We have also observed correlated insulating states at B = 28 T. Figure 5.9**(b)** shows G_{xx} as a function of $1/T$ at 28 T for $\nu = +2$ and $\nu = +3$ states. Similarly, we calculated the thermal activation gap of these states to be $\triangle = 0.85$ meV ($\nu = +2$) and 0.17 meV ($\nu = +3$).

Therefore, the temperature activated gap of the integer filling $\nu = +2$ is almost 4 times higher at the full flux than the zero field case. Similarly, the $\nu = +3$ correlated insulating gap at full magnetic flux is also three times higher than the gap at zero field. Qualitatively, we can expect to have stronger correlation in the flat band at high magnetic field than the zero field flat band.

In summary, we discussed the observation of interaction-driven correlated insulating phases at one flux quantum per moiré unit cell in MATBG. Our experimental observations largely agree with our single-particle Hofstadter calculations, which predict the emergence of a set of electronic flat bands at full flux with different symmetry and topology than the zero-field flat bands. These bands are unstable to the

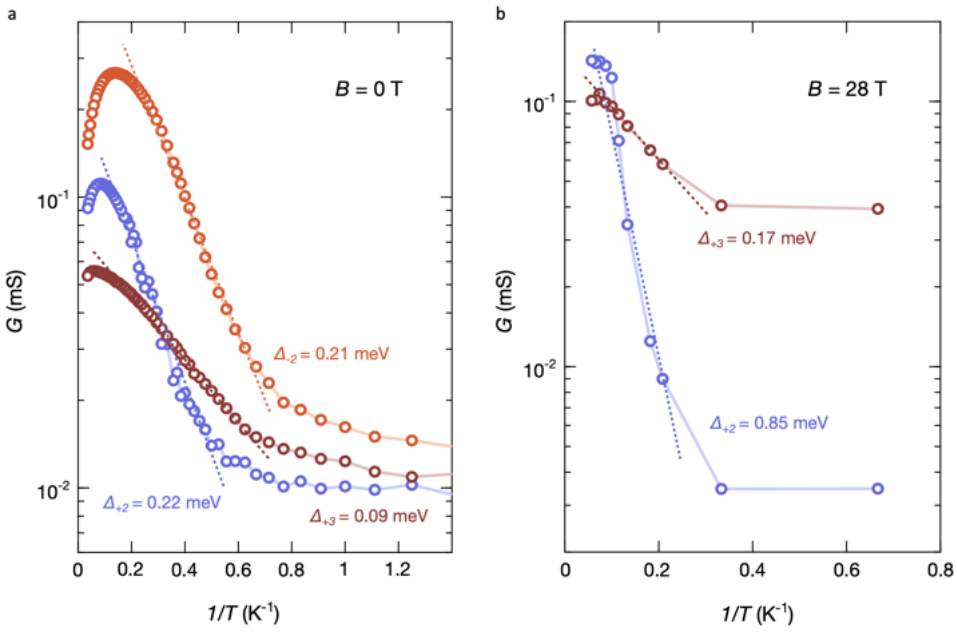

Fig. 5.9: Temperature dependence of the CIs. **(a)** Conductance (G_{xx}) as a function of $1/T$ for the correlated insulating states at ν = +2 (blue), +3 (wine red), and -2 (orange) at zero magnetic field. From the Arrhenius fit, the extracted temperature activated gaps are $\triangle$ = 0.22 meV, 0.09 meV and 0.21 meV, respectively. **(b)** G_{xx} as a function of $1/T$ for the insulating states at ν = +2 (blue) and v = +3 (wine red), at B = 28 T. Calculated thermal activation gaps of these states are $\triangle$ = 0.85 meV and 0.17 meV respectively. Dotted lines are the Arrhenius fitting of the line plots.

creation of correlated states by interactions.

Chapter 6

Higher Energy Dispersive Bands in Magic-angle Twisted Bilayer Graphene

The band structure calculation of magic angle twisted bilayer graphene (MATBG) comprises two connected nearly flat topological bands and a set of higher energy dispersive bands. The higher energy dispersive bands are separated from the flat bands by an energy gap of 50 meV. Different imaging techniques such as, low-energy electron microscopy (LEEM), scanning tunnelling microscopy (STM) and angle resolved photo-emission spectroscopy (ARPES) etc. can directly map the band dispersion of MATBG [96–99]. However, electronic transport measurements have not been able to verify the band structure so far.

In this chapter, we will discuss the effect of magnetic field on the higher energy dispersive bands of MATBG. These two lowest-lying higher energy dispersive bands can be modelled with a Rashba-like Hamiltonian. These two Rashba like dispersive bands give rise to two sets of Landau levels (LLs) while subjected to a magnetic field. In the first section of this chapter, we will discuss the LL crossings of these bands upto a magnetic field of $B = 8$ T. From the evolution of the Landau levels in the dispersive bands, we can show that our experimental results enable a parameter-free comparison to a newly derived **magic series** of level crossings in a magnetic field and provide constraints on the parameters of the Bistritzer–MacDonald MATBG Hamiltonian.

Later, we will discuss the effect of high magnetic field on these

dispersive bands and the single particle Hofstadter spectrum of the Rashba like bands.

6.1 Higher energy dispersive bands

In MATBG, the low energy continuum model of the Bistritzer-MacDonald Hamiltonian consists of three terms, two single layer Dirac Hamiltonian terms that describe the isolated graphene sheets and a tunneling term that describes the hopping between two layers [61]. The solution of this Hamiltonian including the corrugation terms gives rise to fourfold degenerate higher-energy bands that can be modelled with a Rashba-like Hamiltonian. Effectively, a two-band model to order $O(k^2)$ can transit from a Dirac point into quadratic free electron bands. In this section we will first discuss the higher energy band structure of MATBG by a Rashba Hamiltonian. After that we will derive the Landau levels emerging from these Rashba bands and the level crossings between them.

6.1.1 Dispersive bands of MATBG

The solution of the single particle continuum model of the Bistritzer-MacDonald Hamiltonian gives rise to a flat band with a width of $\sim$ 10 meV. In Figure 6.1, we have shown the band structure of a magic angle twisted bilayer graphene system with a relative twist angle of θ = 1.12° ±0.02° between the two layers of graphene. In the low energy limit, the band structure consists of a set of topologically non-trivial fourfold degenerate flat bands. These flat bands are isolated from the next dispersive bands by an energy gap of $\sim$ 50 meV. We have plotted the lower energy bands in Figure 6.1**(a)** in the $E-k$ diagram of the first Brillouin zone. The purple flat bands are separated from the light red dispersive bands. The dispersive bands are electron-hole symmetric. Figure 6.1**(b)** and Figure 6.1**(c)** represent the focused top and bottom part of the conduction and valence dispersive bands respectively. At the Γ point two dispersive bands touch each other almost linearly (upto an approximation) which is called the Dirac point, as shown by the blue points in Figure 6.1**(b)** and Figure 6.1**(c)**.

The Rashba effect, also called Bychkov-Rashba effect, is a momentum dependent splitting of spin bands in bulk crystals and low dimensional condensed matter systems. This has been observed in different

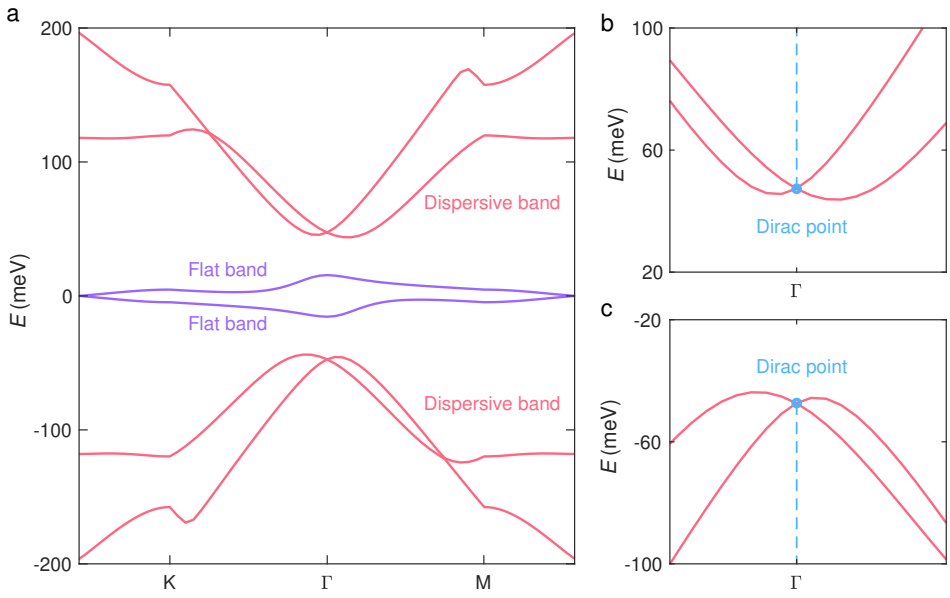

Fig. 6.1: Band structure of MATBG with a twist angle $\theta = 1.12°$. **(a)** Band structure at lower energy level upto $E = 200$ meV, with flat bands in purple colour and dispersive bands in light red colour in the first BZ. **(b)** Zoomed-in plot of the conduction dispersive bands showing the Rashba splitting with the Dirac point at Γ point. **(c)** Zoomed-in plot of the valence dispersive bands showing the Rashba splitting with the Dirac point at Γ point.

two dimensional heterostructures and surface states. This effect is similar to the splitting of particle and antiparticle bands in the Dirac Hamiltonian. The splitting is a combined effect of spin-orbit interaction and the asymmetry of the crystal potential, in particular, in the direction perpendicular to the two dimensional plane as applied to surfaces and heterostructures.

People have used the spin orbit coupling in different systems to have Rashba bands. One of its main uses is in the spintronics field. Rashba spin-orbit coupling enables electric control of spin states, promising enormous advances from conventional charge-based computing. Different 2D van der Waals hetero-bilayer systems are the potential candidates for this study [100, 101]. The strong spin-orbit coupling (SOC) in perovskite materials induces interesting electronic characteristics, such as Rashba band splitting due to the presence of heavy atoms [102]. The Rashba-type spin-orbit coupling in systems with inversion symmetry

breaking is particularly attractive for spintronics applications since it allows flexible manipulation of spin current by external electric fields [103].

In all the above mentioned systems spin-orbit coupling leads to the Rashba splitting of the electronic bands. However, spin-orbit coupling is almost negligible in graphene due to the light weight carbon atoms. The origin of the splitting comes from the asymmetric crystal terms. Although the origin of these two dispersive bands is different than the SOC, for quantitative analysis, we will model the two passive bands in the BM Hamiltonian with a two band Rashba-like model. In the next section, we will derive the Landau levels of these Rashba like bands and the level crossings between them.

6.2 Landau levels in the Rashba-like dispersive bands

In the two band Rashba-like model the Hamiltonian is given by,

$$H = \frac{k_x^2 + k_y^2}{2m}\sigma_0 + \lambda(k_x\sigma_1 + k_y\sigma_2) \tag{6.1}$$

This describes the low energy theory of a Dirac node with a velocity term λ which interpolates the free electron dispersion with effective mass m. We have set $\hbar = 1$ here. Later, we will discuss a perturbative derivation of the Rashba term from the BM Hamiltonian. We will canonically couple this model with a magnetic field and set the momentum terms as,

$$k_x \to p_x \equiv -i\partial_x + A_x \quad \text{and} \quad k_y \to p_y \equiv -i\partial_y + A_y \tag{6.2}$$

In this picture the canonical equation for the momentum is given by,

$$[p_x, p_y] = -i(\partial_x A_y - \partial_y A_x) = -iB \tag{6.3}$$

The raising and lowering terms are defined as,

$$a^\dagger = \frac{1}{\sqrt{2B}}(p_x - ip_y) \quad \text{and} \quad a = \frac{1}{\sqrt{2B}}(p_x + ip_y) \tag{6.4}$$

with the conditions,

$$[a, a^\dagger] = 1 \quad \text{and} \quad a^\dagger a = \frac{k_x^2 + k_y^2 - B}{2B} \tag{6.5}$$

In this picture, the vacuum state ($|0\rangle$) is given by, $|0\rangle = 0$. Hence, we can rewrite the Hamiltonian as,

$$H = \begin{pmatrix} \frac{B}{2m}(2a^\dagger a + 1) & \lambda\sqrt{2B}a \\ \lambda\sqrt{2B}a^\dagger & \frac{B}{2m}(2a^\dagger a + 1) \end{pmatrix} \tag{6.6}$$

In this Hilbert space, the Fock states can be written with respect to the raising and lowering operators as,

$$a|l+1\rangle = \sqrt{(l+1)}|l\rangle \quad \text{and} \quad a^\dagger|l\rangle = \sqrt{(l+1)}|l+1\rangle \tag{6.7}$$

The Landau level spectrum is derived by applying H on these Fock states,

$$H\begin{pmatrix} |l-1\rangle \\ |l\rangle \end{pmatrix} = \begin{pmatrix} \frac{B}{2m}(2(l-1)+1) & \lambda\sqrt{2Bl} \\ \lambda\sqrt{2Bl} & \frac{B}{2m}(2l+1) \end{pmatrix}\begin{pmatrix} |l-1\rangle \\ |l\rangle \end{pmatrix}, l \geq 1 \tag{6.8}$$

By diagonalizing the representations of the Hamiltonian on the Fock states, we find the Landau levels given by,

$$\begin{aligned} E_{+,l}(B) &= \frac{1}{m}\left(lB + \sqrt{\frac{B^2}{4} + \xi Bl}\right), l = 0, 1, ... \\ E_{-,l}(B) &= \frac{1}{m}\left(lB - \sqrt{\frac{B^2}{4} + \xi Bl}\right), l = 1, 2, ... \end{aligned} \tag{6.9}$$

where, $\xi = 2m^2\lambda^2$ is the coupling parameter.

We now discuss the degeneracy of each Landau level. In a finite sample of area $A = N\Omega$, where N is the number of moiré unit cells, each with area Ω, semi-classical quantization gives the total number of states $N = BA/2\pi = \Phi N/2\pi$ where, $\Phi = B\Omega$ is the flux through a single moiré unit cell.

We will find it useful to choose units where $\Omega = 1$, so that $B = \Phi$. Then the density of states per unit cell is $n = \Phi/2\pi$. If C Landau levels are filled, then each of the C levels contributes to the density of states and we recover the Streda formula $n = C\Phi/2\pi$, consistent with the fact that each Landau band carries a Chern number $C = 1$. If we plot the longitudinal resistance (R_{xx}) as a function of Φ and carrier density n, the Streda formula allows the gaps with the Chern number C to appear as the distinctive linear features. This is called the Landau fan diagram. In the case of a free particle with $\lambda = 0$, gaps of all the

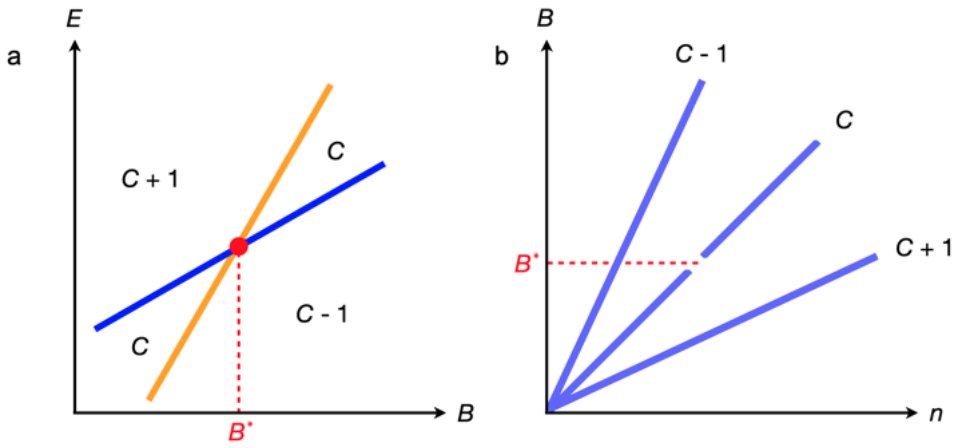

Fig. 6.2: Schematics of LL crossings. We illustrate how a level crossing in the Landau level spectrum affects the Landau fan. **(a)** We show two Landau levels each carrying Chern number $C = 1$ intersecting at a critical magnetic field B^*. For generic B, there will be gaps with Chern number $C - 1$, C, and $C + 1$. At exactly B^*, there are only $C + 1$ and $C - 1$ gaps because the C gap closes. **(b)** The Landau fan shows how the gaps of Chern number C change their carrier density n as the magnetic field is varied. The Streda formula guarantees linear trajectories with slope $1/C$ for a gap of Chern number C. However, at B^*, where the gap closes, we expect a break in the trajectory where the bulk conductivity is high. Under experimental conditions, this gap will be broadened into a finite region.

Chern numbers appear at every flux and never close (for small field below the Hofstadter regime). Hence, the lines in the Landau fan are never broken. We will now see that when λ is nonzero, these gaps close at different critical values of the magnetic field. At these points of gap closing, we expect to see low resistance peaks interrupting the lines of the Landau fan observed in the experiment, as shown in Figure 6.2.

In order to discuss the band crossings, we will make another scaling and consider $B = \xi b$ where b is a dimensionless field strength. Then we can rewrite the Landau levels as arising from two branches,

$$E_{\pm,l}(b) = \frac{\xi}{m}\left(bl \pm \sqrt{\frac{b^2}{4} + bl}\right), l = \begin{cases} 0, 1, ..., & \text{for} + \\ 1, ..., & \text{for} - \end{cases} \tag{6.10}$$

with all the parameters factored into the overall energy scale. As such, the critical b values where the Landau levels intersect are independent

of all the parameters of the Hamiltonian. The Landau levels and their level crossings are shown in Figure 6.4. In this case only three types of crossings can occur:

1. Intersections of the $E_{+,l}(b)$ and $E_{-,l'}(b)$ levels for $l' \geq l+2$. These crossings are denoted by $b_+(l,l')$.

2. Intersections of the $E_{-,l}(b)$ and $E_{-,l'}(b)$ levels for $l' \geq l+2$. These crossings are denoted by $b_-(l,l')$.

3. Intersections of the $E_{-,l}(b)$ and $E_0(b)$. These crossings occur at

$$b_\pm(l,l') = \frac{1}{l+l' \mp \sqrt{4ll'+1}} \quad \text{with} \begin{cases} l' \geq l+2, & + \\ l' \neq l, & - \end{cases} \tag{6.11}$$

This equation expresses the crossings in terms of the Landau level index. Using this expression, we will now determine the succession of level crossings which interrupt gaps of the Chern number C, as observed experimentally and discussed later. In the large b limit, Landau levels are given by,

$$E_{\pm,l}(b) = \frac{\xi}{m}(b(l \pm 1/2) \pm l + O(1/b)) \tag{6.12}$$

From this energy spectrum, we can easily deduce that,

$$E_{+,l}(b) - E_{-,l+1}(b) = 2l + 1 + O(1/b) \tag{6.13}$$

With respect to the energy of these levels we can order them as,

$$E_{-,1} < E_{+,0} < E_{-,2} < E_{+,1} < E_{-,3} < E_{+,2} < ..... \tag{6.14}$$

These levels are organised into parallel levels, $E_{+,l}$ and $E_{-,l+1}$. These parallel levels are gapped from each other and have the same slope to the leading order of b. We can organize the large b spectrum into two kinds of gaps, those between the parallel levels $E_{+,l}$ and $E_{-,l+1}$ (hence having an odd number of Landau levels below), and those separating neighboring pairs of parallel levels (hence having an even number of Landau levels below). Recall that $b = B/\xi$ is dimensionless, so the physical meaning of large b depends on the Rashba coupling. As we will show shortly, the critical value of b for which the largest b gap of

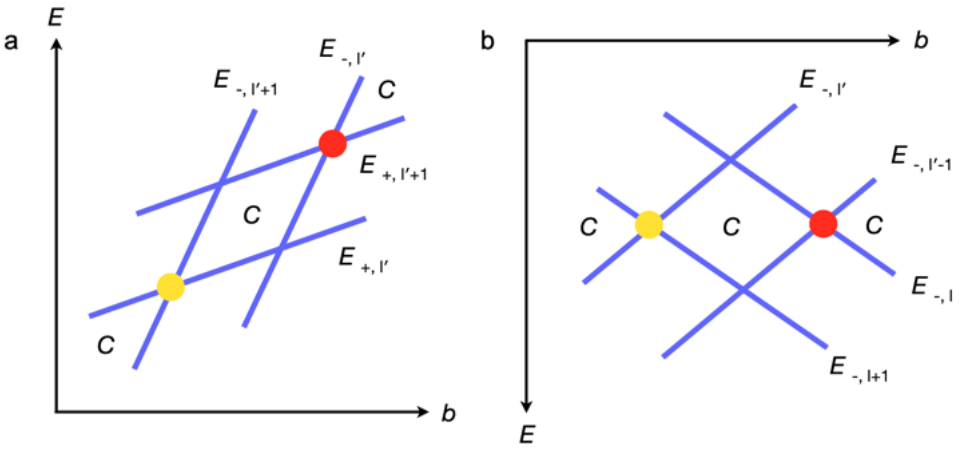

Fig. 6.3: Structure of gap closings. **(a)** The local structure of the next (smaller b) Chern number C gap closing, shown in orange, after the level crossing of $E_{-,l}$ and $E_{+,l+1}$, shown in red. **(b)** The local structure of the series of Chern number C gap closings that occur below $E = 0$. Note that the crossing are all between levels in the negative branch.

the Chern number C closes depends on C. For $C = 4$, Figure 6.4 gives $b \sim 2.5$ (we will shortly give an exact expression).

We now want to determine where these gaps first close as b is decreased from infinity. We first consider the even Chern number gaps of $C = 2l + 1, l = 0, 1, ..$ between $E_{+,l}(b)$ and $E_{-,l+2}(b)$. The two levels $E_{+,l}(b)$ and $E_{-,l+2}(b)$ are not parallel and the gap closes when they intersect at $b_+(l, l+2)$. Rewriting this crossing in terms of $l = (C-2)/2$, we find that the initial gap closing (indexed from zero) for $C = 2, 4, 6, ...$ is given by,

$$b_{C,0} = \frac{1}{C - \sqrt{C^2 - 3}} \quad \text{for} \quad C \geq 2, \text{even} \tag{6.15}$$

We now consider the odd Chern number gaps of $C = 2l + 1, l = 1, 2, ...$ in between $E_{-,l+1}$ and $E_{+,l}$. Because these levels are parallel, the gap closing happens in a manner different to the case of even C. The parallel $E_{-,l+1}$ and $E_{+,l}$ levels will both be crossed by the neighboring levels of different slopes, respectively $E_{+,l-1}$ and $E_{-,l+2}$, but these crossings do not close the $C = 2l + 1$ Chern gap. Only when $E_{+,l-1}$ and $E_{-,l+2}$ cross at $b_+(l - 1, l + 2)$, the $C = 2l + 1$ gap closes.

Writing $b_+(l-1, l+2)$ in terms of the Chern number yields,

$$b_{C,0} = \frac{1}{C - \sqrt{C^2 - 8}} \quad \text{for} \quad C \geq 3, \text{odd} \tag{6.16}$$

The case of $C = 1$ may be analyzed separately, but we will not need to do so because the $C = 1$ gap closings appear very close to the band gap where very large resistance obscures the theoretical gap closings.

With the large b gap closings understood, we will extend these formulae to the cascade of additional gap closings that occur at smaller b. We will first consider the successive gaps that close due to a crossing with a level from the positive branch. The upper and lower levels are from the positive branch $E_{+,l+1}$ and $E_{+,l}$ respectively. This happens because the positive branch is monotonically increasing in l. Here we have assumed that $l \geq 0$ so $E_{+,l}$ is an allowed level.

The right and left levels $E_{-,l\,'+1}$ and $E_{-,l\,'}$ are from the negative branch and their ordering is determined by noting that $E_{-,l}(b)$ is monotonically increasing in l when $E_{-,l}(b) > 0$. Because we assume $l \geq 0$ and $E_{+,l}(b) \geq 0$ for all nonzero b, then crossings of $E_{-,l\,'+1}(b)$ with $E_{+,l}(b)$ occur for $E_{-,l\,'+1}(b) > 0$.

Hence we see that, if there is a gap closing for the Chern number C at $b_+(l+1, l\,')$, the next gap closing will occur at $b_+(l, l\,'+1)$. By repeating this argument starting with the $m = 0$ gaps deduced above, we find that the m^{th} gap for $C = 2l+2$ occurs at $b_+(l-m, l+2+m)$ for $m \leq l$ and the m^{th} gap closing for $C = 2l+1$ occurs at $b_+(l-1-m, l+2+m)$ for $m \leq l-1$. Writing the crossings in terms of the Chern number, we find,

$$b_{C,m\leq\lfloor(C-2)/2\rfloor} = \begin{cases} \frac{C+\sqrt{C^2-(2m+1)(2m+3)}}{(2m+1)(2m+3)}, & C = 2l+2, m = 0, 1, ..., l \\ \frac{C+\sqrt{C^2-(2m+2)(2m+4)}}{(2m+2)(2m+4)}, & C = 2l+1, m = 0, 1, ..., l-1 \end{cases} \tag{6.17}$$

After crossing the $E_{+,0}$ level, all the further gap closings happen when different levels from the negative branch intersect as shown in Figure 6.3. Let's consider the Chern number C gap closing of $E_{+,0}$ and $E_{-,l}$. The level crossings in terms of the Chern number and $b_{C,m\leq\lfloor(C-2)/2\rfloor}$ is referred to as the magic series. This is called the magic series due to the unique series number of the magnetic field where the level crossings happen. We have overlaid this magic series with our experimental

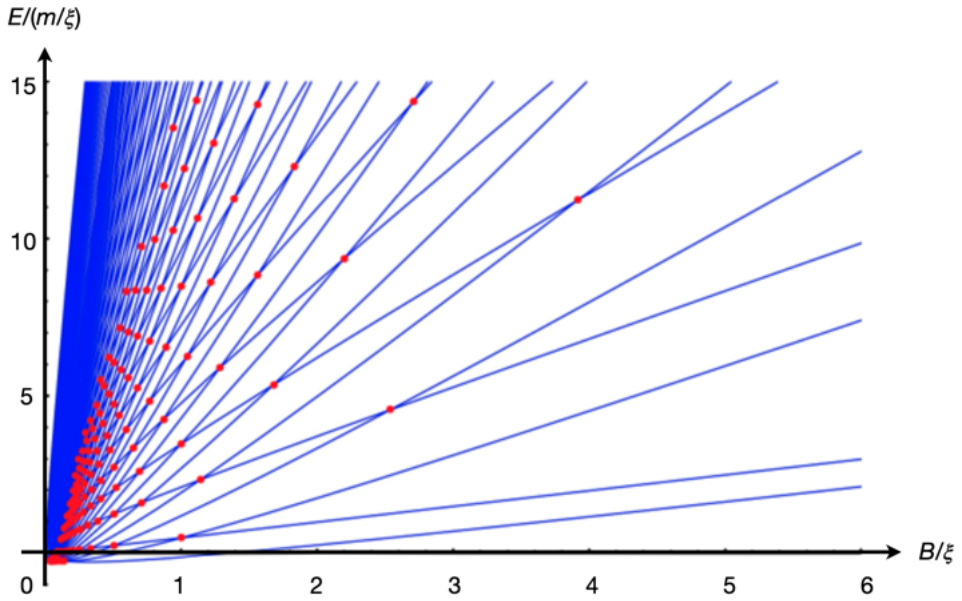

Fig. 6.4: Calculated Landau level spectrum. It illustrates the Landau levels of the Rashba Hamiltonian, and indicate the level crossings with red dots. These level crossings appear in magic series as mentioned in the text.

data and compared them in order to understand the band structure as described in this exact theoretical calculation.

The magic series allow us to determine all the gaps $m = 0, 1, ..$ in the Chern number C of the Landau fan. As noted earlier, all the parameters of the Rashba Hamiltonian are factored out into an overall energy scale and magnetic field scale. Hence, all the ratios of the terms in the magic series are parameter-independent, allowing for extremely stringent tests of the Rashba approximation. Remarkably, we find very good agreement with the experimental data, which we will discuss in detail later.

6.3 Landau levels of the dispersive bands in MATBG

We have tuned the carrier density beyond the flat bands and studied the dispersive bands in the presence of an external magnetic field. In this regime we studied the longitudinal resistance R_{xx} as a function of

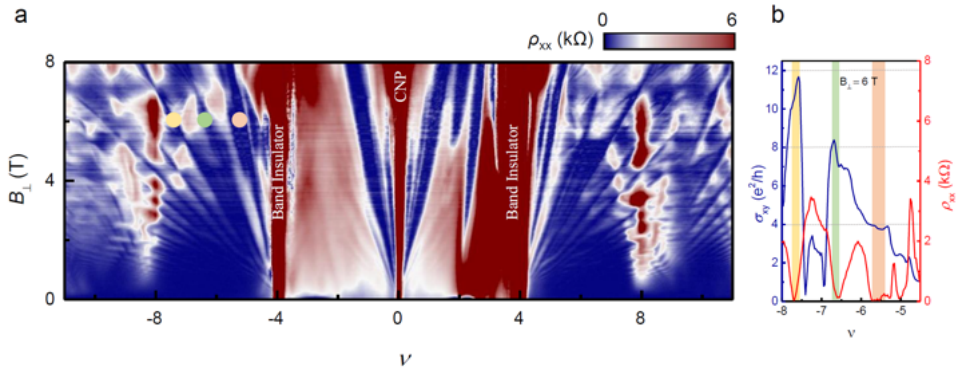

Fig. 6.5: Full magnetic field phase diagram of both the flat bands and higher energy dispersive bands at 30 mK. **(a)** Longitudinal resistance (color plot) as a function of filling factor, ν and magnetic field, B. **(b)** σ_{xy} and ρ_{xx} as a function of ν shows clear quantization of Chern states outside the flat band.

B which reveals a rich fourfold degenerate LL spectrum. Figure 6.5**(a)** represents the full magnetic field phase space of a MATBG device with a twist angle $\theta = 1.04°$. The flat band consists of the Chern insulators at different integer fillings as discussed in Chapter 4. Apart from that, we also observed two new sets of LLs emerging from the edge of the bands at the integer filling $\nu = \pm 4$. One set of LLs from one of the dispersive bands is interrupted by another set of LLs originating from another band. We have clearly observed many crossings of the Landau level gaps at lower magnetic field ($B < 4$ T) as reported in other systems as well [104–106].

In Figure 6.5**(a)**, dark blue lines fanning out from $\nu = \pm 4$ correspond to the LLs. To confirm the degeneracy of these states, we have also measured the Hall resistance R_{xy} at $B = 6$ T. Figure 6.5**(b)** shows both the longitudinal resistance (ρ_{xx}) and Hall conductivity σ_{xy} of the dispersive band in the hole side at $B = 6$ T. Light orange, green and yellow regions mark the clear quantized plateaus of the Hall conductivity (σ_{xy}) at $4e^2/h$, $8e^2/h$ and $12e^2/h$ respectively. These regions correspond to three LLs marked by the same corresponding colours in 6.5**(a)**. This specific sequence of the LLs indicates the fourfold degeneracy of the dispersive bands.

In the next section, we will discuss the crossings of these Landau levels, in which the degeneracy of these levels will play a significant role.

6.4 LL crossings in the dispersive bands

We exactly solved the Rashba Hamiltonian in the presence of B field and obtained the LLs as discussed in section 6.2, which are in excellent quantitative agreement with the experimental findings.

Figure 6.6**(a)** reveals a set of LLs each carrying a Chern number $C = \pm 4$. These set of LLs are interpolated from the Dirac node of the dispersive bands towards the quadratic free electron regime. As clearly visible, many of these LLs undergo a series of crossings. In order to understand the crossings better, we have plotted R_{xx} as a function of C and $1/B_{\perp}$ in Figure 6.6**(b)**. Each of the LL (nth) with a particular Chern number gets interrupted by another LL ((n+1)th) at a particular magnetic field value, B^*. The LL with Chern number C = -16 evolves with the magnetic field and at a particular value of B, which is marked by red square, it closes by the interruption of the LL with C = -24. As we keep increasing the magnetic field, the same LL gap continues. For several LLs with C = -24, -28, the LL gaps are interrupted multiple times. We count different generations of the crossings for each LL from high to low value of $B_{\perp}$. We extract the B^* values for all the LL crossings (from Figure 6.6**(b)**) and normalize these to the $B^*_{|24|,3}$ field which is the third crossing of the LL at $C = \pm 24$ (for both electrons and holes, respectively). We plotted this data as a function of $|C|$ with our theoretically calculated values shown in Figure 6.6**(c)**. This allows us to extract an estimate of the Rashba coupling parameter ξ as discussed in section 6.2. Moreover, we find that the ratios between all the B^* values are independent of all the parameters of the low-energy Hamiltonian and therefore present a stringent, parameter-free test of the physics. We call this the **magic-series**. The two corrugation parameters w_0 and w_1 of the Bistritzer–MacDonald Hamiltonian are constrained by the measured Rashba coupling $\xi = 0.186/\Omega$ (h = 1 and $\Omega = \sqrt{3}/2(13.5\text{nm})^2$ is the area of the moiré unit cell), presenting a direct estimation of the physical parameters of MATBG. Neglecting the particle–hole symmetry breaking, we find that the ranges $0.7 \leq w_0/(v_F k_D/\sqrt{3}) \leq 0.80$ and $0.95 \leq w_1/(v_F k_D)/\sqrt{3}$ are in good agreement with the measurements of the Rashba coupling, where v_F is the Fermi velocity and k_D is the moiré wavevector.

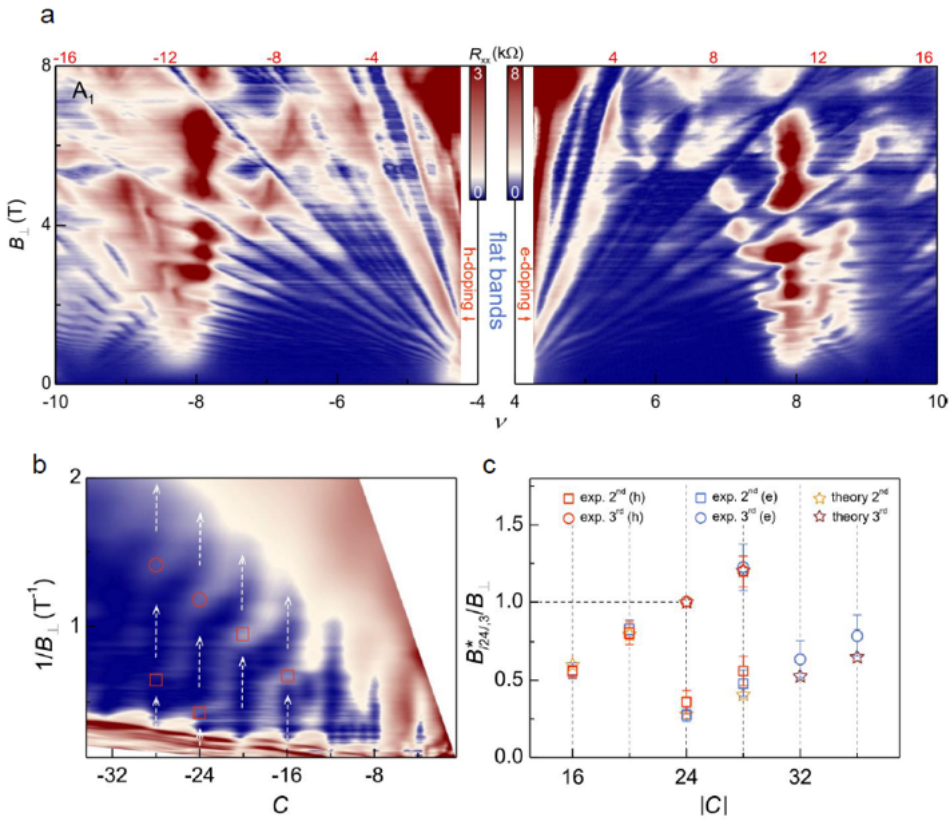

Fig. 6.6: LL crossings in higher-energy dispersive bands. **(a)** Colour plot of R_{xx} versus ν and $B_\perp$ measured at $T = 30$ mK, where the Chern numbers of the most dominant LL gaps are marked. **(b)** Colour plot of R_{xx} versus C and $1/B_\perp$ (with data from the hole side of **(a)**), showing interrupting trajectories of the different LL gaps. Corresponding gap closings are marked. **(c)** Comparison of the experimentally observed LL gap closings (exp. 2nd, exp. 3rd) and the theoretically predicted (Theory 2nd, Theory 3rd), normalized to $B^*_{|24|,3}$, the field of the third-generation gap closing of the $C = \pm 24$ LL gaps (for electrons and holes, respectively). The error bars are defined by the full-width at half-maximum values of R_{xx} versus $1/B_\perp$ peaks where the LL crossings occur.

6.4.1 Estimation of the corrugation parameters

Our measurement of ξ from the experimental data imposes constraints on the corrugation parameters w_0 and w_1 which determine the band structure of the Bistritzer-MacDonald Hamiltonian. In principle, we

can use the Bistritzer-MacDonald band structure to numerically determine $\xi(w_0.w_1)$. Our measurement of ξ places a strong constraint on the allowed values of w_0 and w_1. However, first, we must discuss the approximations made in applying the Rashba-like Hamiltonian. Importantly, the Bistritzer-MacDonald Hamiltonian only has $C3$ symmetry, whereas the Rashba Hamiltonian has full rotational symmetry. Generically, we expect additional low-order terms to correct the Rashba Landau level spectrum by breaking the full rotational symmetry to three-fold symmetry. However, the excellent fit of data to the magic series leads us to believe that such symmetry-breaking terms are small, at low chemical potential in the higher-energy bands. This also guides our constraint of w_0 and w_1.

To extract the effective ξ from the band structure of the Bistritzer-MacDonald Hamiltonian, we study the $B = 0$ properties of the Rashba Hamiltonian. The band structure is given by,

$$E(k) = \frac{|k|^2}{2m} \pm \lambda|k|) \tag{6.18}$$

from which we note that, $|k| = 0$ and $|k| = 2m\lambda = \xi^2/2$ have the same energy, $E(k) = 0$. Hence the $E(k) = 0$ equienergy contour gives the value of ξ. For $C3$ symmetric perturbations, to the Hamiltonian, the average $|k|$ along the contour gives an effective value of ξ, and the deviation of the contour gives an estimate of the perturbation. We observed that the trigonal warping is stronger with decreasing w_1, leading us to expect $w_1 > 0.95$. In this regime, ξ smoothly varies as a function of w_0. On the electron side at filling $\nu = +4$, we find $\xi \sim 0.18$ leading us to estimate $0.70 \leq w_0 \leq 0.80$. On the hole side at $\nu =$ -4, we find $\xi \sim 0.135$ indicating a breaking of particle-hole symmetry as is expected. For simplicity, we have not incorporated particle-hole breaking in the Bistritzer-MacDonald Hamiltonian. Hence the values of w_0 and w_1 that we estimated are valid up to (small but non-negligible) particle-hole symmetry breaking effects.

Magnetic field dependence of R_{xx} in the higher energy dispersive bands allows us to observe the crossings of different set of LLs which present a direct estimation of the corrugation factor of the BM Hamiltonian. For the first time, this experimental observation allows us to calculate the higher energy dispersive bands of MATBG which matches the theoretically predicted band structure.

6.5 Higher magnetic field Hofstadter spectrum of dispersive bands

The higher energy dispersive bands in MATBG have prominent characteristics of Landau level crossings at low magnetic field. However, the high magnetic field behaviour is mostly dominated by the Hofstadter spectrum. Since these higher energy dispersive bands have larger bandwidth than flat bands, it becomes more amenable to study the single particle Hofstadter spectrum in this range. In this section we will discuss the Hofstadter picture of the dispersive bands from zero magnetic field to one magnetic flux quantum per moiré unit cell (Φ_0). We have discussed how the flat band evolves in the presence of an external magnetic field as we increase the field by one magnetic flux quantum in Chapter 5. In this chapter we have learned that the higher energy dispersive bands are very important to understand and verify the ground state flat bands in MATBG. So far, we have only discussed the behaviour of these bands at a lower magnetic field ($B < 8$T).

In this section we will numerically calculate the single particle Hofstadter spectrum of the Dispersive bands until Φ_0.

6.5.1 Full Hofstadter spectrum

The higher lattice periodicity ($\lambda \sim 15$ nm) of MATBG allows us to study the full Hofstadter spectrum within an accessible magnetic field. In Figure 6.7 we have plotted the available energy states for flux $2\pi p/q$ where 2π flux = 31 T for the energy range $E = \pm 250$ meV. The flat bands remain gapped for all flux, while the passive bands develop a complex structure with many gaps larger than 6meV [107]. Near the zero energy regime, the Coulomb interaction ($\sim$ 20 meV) dominates over the kinetic energy, suppressing any single-particle signatures inside the flat band. Our primary observation is that the single-particle bands undergo significant restructuring from 0 to 2π flux. At 2π flux, the original Brillouin zone is restored and the bandwidth of the flat bands is very similar to the zero flux bands. However, the dispersive bands can be described by the single particle Hamiltonian. We emphasize that our calculations are exact within the BM model, and do not rely on $k \cdot p$ approximations near the Fermi surfaces. In Figure 6.7 the Chern numbers of the largest gaps are computed using Wilson loops and the Streda formula.

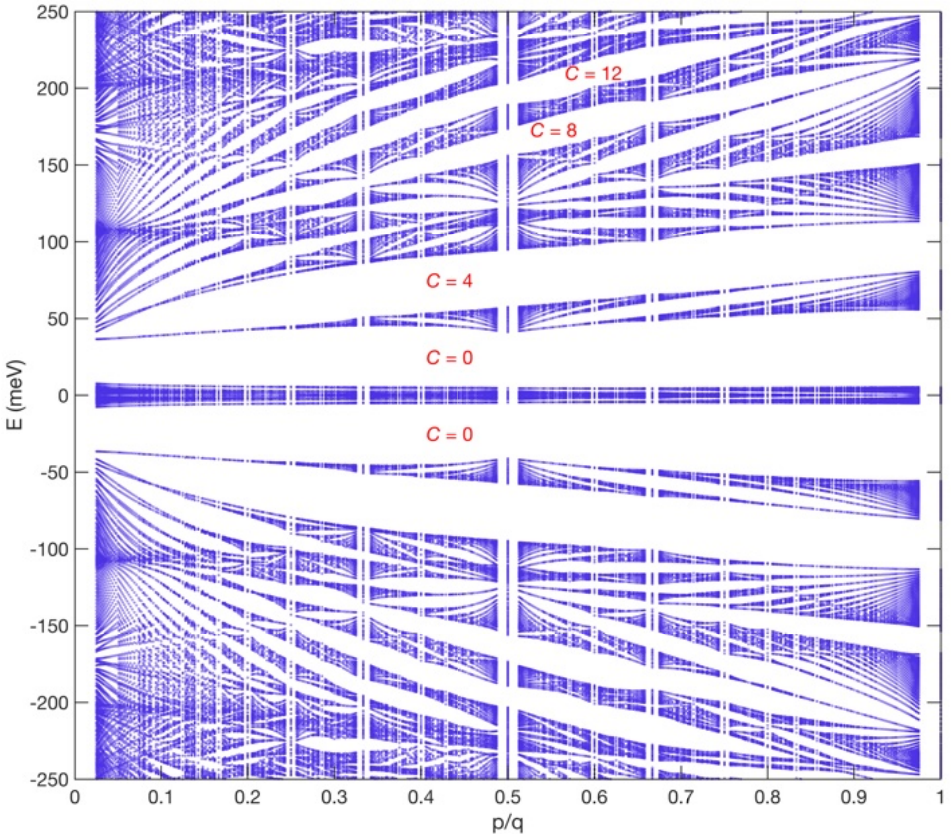

Fig. 6.7: Full Hofstadter spectrum of MATBG with a twist angle θ = 1.12°. This illustrates the bands with Hofstadter gaps and Chern numbers for the energy range $E = \pm 250$ meV.

In Figure 6.8, only the positive energy side of the Hofstadter spectrum has been plotted as a function of the magnetic flux (Φ/Φ_0) and energy (E). This Hofstadter spectrum is converted into the Wannier diagram by using the Diophantine equation, as shown in Figure 6.8**(b)**. This Wannier diagram is the direct comparison with our experimentally obtained Landau level data.

In the next section, we will compare this theoretically predicted model with our experimental data.

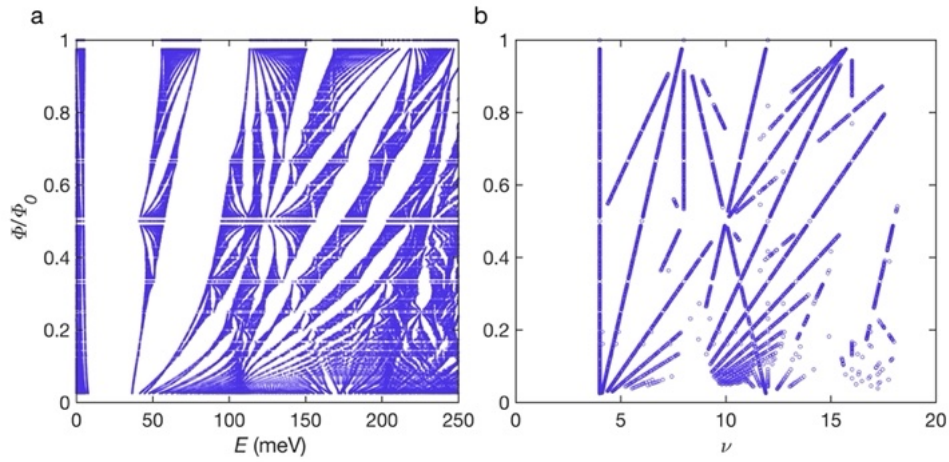

Fig. 6.8: Hofstadter spectrum and Wannier diagram for the positive energy limit. **(a)** Hofstadter spectrum with LL gaps in the positive energy scale. **(b)** Wannier diagram of the same energy scale.

6.5.2 Comparison between the theory and the experiment

To access the full Hofstadter spectrum of the dispersive bands, we tuned the carrier density $\nu > 4$ and increased the magnetic field upto Φ_0. Figure 6.9**(b)** shows the color plot of R_{xx} as a function of the normalized magnetic flux and ν. The strongest LLs, observable as lines with slope $1/\nu_L$, are schematically laid out in Figure 6.9**(c)** with corresponding (ν, ν_L), where we find some agreements (but also some disagreements) between the single-particle theory and observed LLs.

The second through fifth bands of the BM model, counting from CNP, form an elementary band representation and are forced to be connected by symmetry. Hence, no gap is expected in the resistance data [Figure 6.9**(b)**] between $\nu = 4$ and $\nu = 20$ at 0 flux, although there is a Dirac point at $\nu \sim 12$ leading to a low density of states. This can be seen in Figure 6.9**(b)** from the deep blue conducting regions near $B = 0$, which are punctuated by the less conductive (lighter blue) regions near $\nu = 4$.

The full-density Bloch bands at zero flux split into Hofstadter sub-bands upon applying a magnetic flux, giving rise to gaps at fractional fillings. The Chern number C of the gaps is given by the Streda formula: $N = pC|q|$, where N is the number of Hofstadter sub-bands that

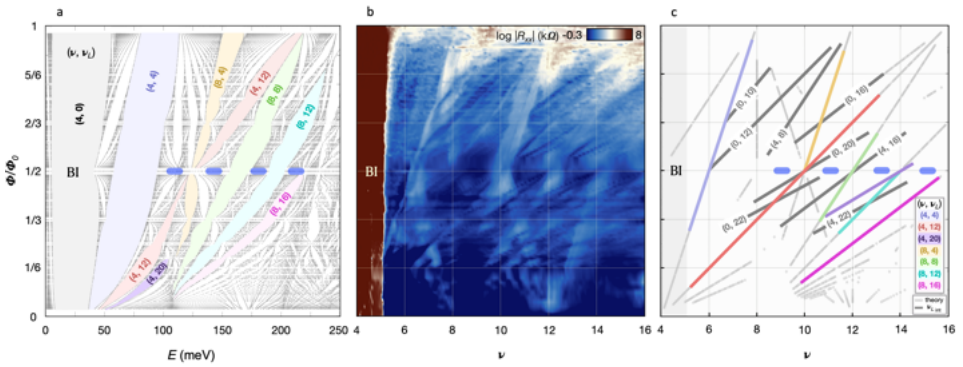

Fig. 6.9: **(a)** Calculated Hofstadter spectrum of the BM model for positive energy as a function of the magnetic flux Φ through the moiré unit cell. Different solid gray (4, 0), blue (4, 4), red (4, 12), yellow (8, 4), green (8, 8), cyan (8, 12), magenta (8, 16) and purple (4, 20) regions correspond to the evolution of dominant LL gaps. They are marked with the band filling and filling factor (ν, ν_L) of the LL. **(b)** Color plot of logR_{xx} as a function of B and ν for high range of carrier density up to $\nu = 16$. **(c)** Schematics of (b) and the comparison with (a), where gray circles mark the theoretically predicted gaps from (a) and colored lines mark the strongest LLs in (b). The observed LLs from (b) are plotted with the same color code as the corresponding LLs in (a). Dark gray lines correspond to LLs, which are not predicted from the Hofstadter calculations. These levels are the result of strong interactions in the system (ν_{Lint}). The horizontal blue bars denote metallic regions in (a) matching the high conductance regions (dark blue regions) observed in (b).

have been filled, as measured from CNP. At fractional filling ($N \neq 0|q|$) C must be nonzero. When interactions, spin-orbit coupling, and the Zeeman effect are neglected, all bands are fourfold degenerate because of the spin and valley degeneracy.

There are three main features observed in the Wannier diagram at the integer fillings $\nu = 4$, 8 and 12 in between the flux filling from $\Phi = 0$ to $\Phi \sim 0.5\Phi_0$ as shown in Figure 6.9**(c)**. Near $\nu = 4$, we predict and observe LLs with a positive slope emerging from the band edge which can be attributed to the low-energy Rashba point in the passive bands of the zero flux BM model [34].

The LLs which are connected to $\nu = 8$ are more interesting. Although there is no band edge at $\nu = 8$ in the BM model, the mag-

netic field breaks the C_{2x} and $C_{2z}T$ symmetries that force the second and third bands to be connected. Thus, we can understand the LLs pointing to $\nu = 8$ as indicating a nascent band edge which is revealed by flux in precise agreement with Figure 6.9**(a)**, which demonstrates strong gaps originating from $\nu = 8$ with Chern numbers $C = 4$, 8, 12 and 16. We expect increased R_{xx} in the regions where LLs of different slopes cross [34]. This is observed in Figure 6.9**(b)** near $\nu = 10$ where the (8, 4) and (12, -4) LLs collide near $0.5\Phi_0$. Additionally, at $0.5\Phi_0$ flux, we observe very clean, highly conducting regions in Figure 6.9**(b)** between the Chern gaps at $\nu = 8$, 10, 12, 14, and 16, corresponding to the metallic regions in the Hofstadter spectrum marked by light blue bars in Figure 6.9**(b)** and 6.9**(c)**.

There is also another set of LLs with Chern number $C = 10$, 18, 22 (which are not divisible by 4) which cannot be described by the single particle picture and rely on interactions to break the spin-valley degeneracy. These LLs originate from the strongly interacting flat bands at zero flux and appear to remain competitive many-body states even at large flux and high fillings. There are also LLs with $\nu_L = 8$, 16 (divisible by 4) and 22 from $\nu = 4$ which do not appear in our single particle calculations. Further work is necessary to characterize these states.

Chapter 7

Effect of Electrostatic Screening on MATBG

Strongly correlated electronic systems host multiple emergent phenomena and different types of interactions. Doping an interaction driven phase often gives rise to further correlated phases. The examples include the fractional quantum Hall states that arise due to doping the composite Fermion sea in a partially filled Landau level [108] and a superconducting state that arises from the doping of a correlated Mott insulator [109]. Particularly, the coexistence of unconventional superconductivity and a correlated insulating phase in heavy fermion systems and pnictides led to the idea that the insulating phase can be the main dictator of the superconductivity in these systems. However, previous attempts to control electron–electron interactions in other crystalline correlated systems were impeded by small atomic orbital sizes and strong sensitivity to doping [110].

The coexistence of the correlated insulator and superconductivity in MATBG [26, 27, 92, 111] led to an immediate question about their relationship in the ground state. Since we can control these phases independently in this system, it gives us access to study the microscopic mechanism responsible for each of these states. Initial experiments have shown that the correlated insulators appear at different integer fillings of the flat band and the superconductivity emerges upon slight doping of these insulators. The coexistence of these orders was considered as an indication that they are directly related and they arise from a common mechanism, similar to the scenarios that have been proposed for the cuprates. However, in a few cases, superconductivity

appears in a wider range of the band filling, covering the entire range of the density between two correlated insulators at different ν. This observation suggests that the superconductivity is a competing phase with the correlated insulator.

In this chapter, we will discuss the interplay between these two states by tuning the electron-electron interaction by changing the separation between the graphene and metallic layers [112, 113].

7.1 Mott-Hubbard model in a 2D lattice

The Hubbard model is an approximate model which mainly describes the electronic states in conductors and insulators. According to this theory, when the electrons are tied to the atoms in a lattice, they mainly experience two types of force, one is the attractive potential from the neighbouring atoms, called hopping energy (t) and another is the potential term for the on-site energy (U). The Hubbard model correctly predicts the existence of Mott insulators, materials that are insulating due to the strong repulsion between electrons, even though they satisfy the usual criteria for conductors, such as having an odd number of electrons per unit cell.

7.1.1 Onsite energy and kinetic energy

The condition for the appearance of correlated insulators is a large ratio of the onsite Coulomb energy U and the kinetic energy t, i.e.

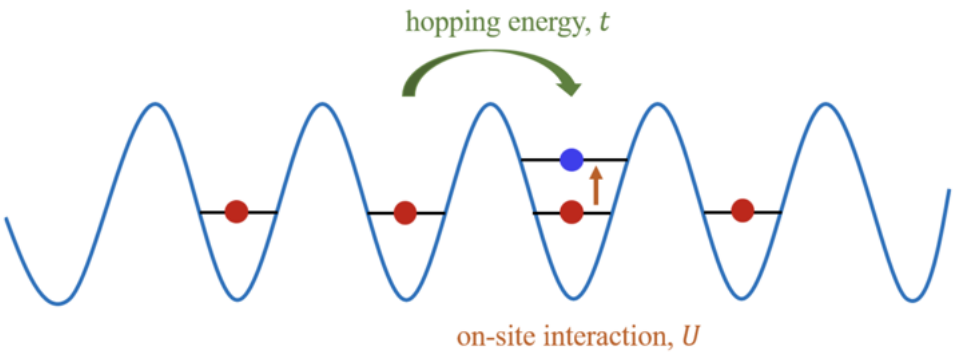

Fig. 7.1: Schematics of the Hubbard model in an one dimensional chain of atoms.

$U/t \gg 1$. In MATBG, t can be increased by tuning θ away from θ_m, which increases the width of the flat bands. The energy U can be controlled independently by changing the dielectric environment. If the distance w between MATBG and a metallic layer is made smaller than the moiré unit cell size, $w < \lambda = 15$ nm, polarization charges will screen out the Coulomb interactions on that scale and suppress U.

7.2 Screening of Coulomb interactions in MATBG structure

Different correlated states in MATBG strongly depend on the distance between the graphene layer and the screening layer, graphite. We have measured different magic angle devices with different screening parameters. We find a strong suppression of the correlated insulators when metallic graphite screening layers are placed closer than 10 nm from the MATBG plane, separated from it by insulating multi-layers of hexagonal boron nitride (hBN), and with θ tuned slightly away from 1.1° by $\pm 0.05^\circ$. Rather than being weakened, superconductivity persists in the absence of the correlated insulators, taking over the phase space vacated by the correlated insulators and spanning wide doping regions without interruption. These observations suggest that the insulating and superconducting orders, rather than sharing a common origin, compete with each other. This observation calls into question a simple analogy with the cuprates.

In this section, we will discuss the theoretical model of the Coulomb screening in a twisted bilayer graphene heterostructure.

There are three different mechanisms that contribute to electric polarization responsible for screening. One is due to the intrinsic (interband and intraband) polarizability of the graphene band structure itself, the second one is due to the dielectric permittivity of hBN and the third one is due to image charges on the surface of the graphite gate. In this model, we will treat the graphite gate as an ideal conductor, setting electrostatic potential equal zero on the graphite surface. The ideal conductor approximation is justified because the typical screening length in graphite (~ 1 nm) is much smaller than the hBN spacer thicknesses used in our devices.

We consider the twisted bilayer graphene layer positioned at $z = 0$ and the hBN spacer of width w located beneath it at $-w \leq z \leq 0$. We

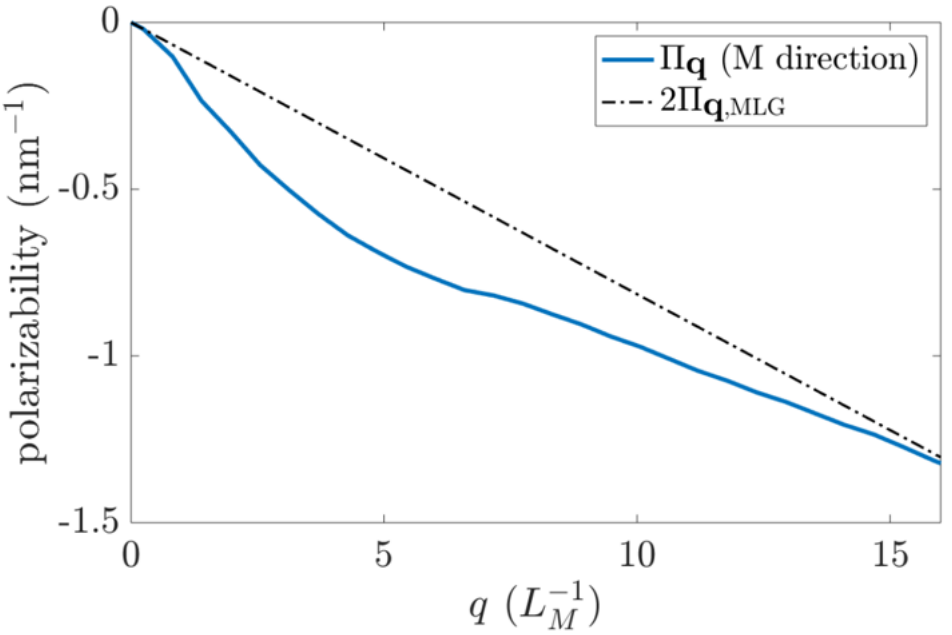

Fig. 7.2: Numerically calculated static polarizability Π_q (blue curve) compared with the prediction for two decoupled graphene monolayers at large q.

then expand the potential of a point charge positioned in the MAG plane, $\Phi(r, z)$, as a sum of Fourier harmonics varying in constant $-z$ planes with coefficients that depend on z,

$$\Phi(r, z) = \sum_q \phi_q(z) e^{iq \cdot r} \tag{7.1}$$

Poisson's equation, written in terms of the quantities $\phi_q(z)$, reads,

$$(\partial_z \kappa(z) \partial_z - \kappa(z) q^2) \phi_q(z) = -4\pi (e + \phi_q(z) \Pi_q) \delta_z \tag{7.2}$$

In this equation, $\kappa(z)$ is the dielectric permittivity of hBN, which is considered to be $\kappa_{hBN} \approx 3.5$ for $-w \leq z \leq 0$ and 1 elsewhere. Π_q is the intrinsic static polarizability of twisted bilayer graphene.

By solving the 3D Poisson's equation for an ideal conductor boundary condition on the graphite surface, we get $\phi_q(z = -w) = 0$. From the solution, we determine the potential in the graphene plane,

$$\phi_q(z = 0) = \frac{4\pi e}{q(1 + \kappa_{hBN} \coth qw) - 4\pi \Pi_q} \tag{7.3}$$

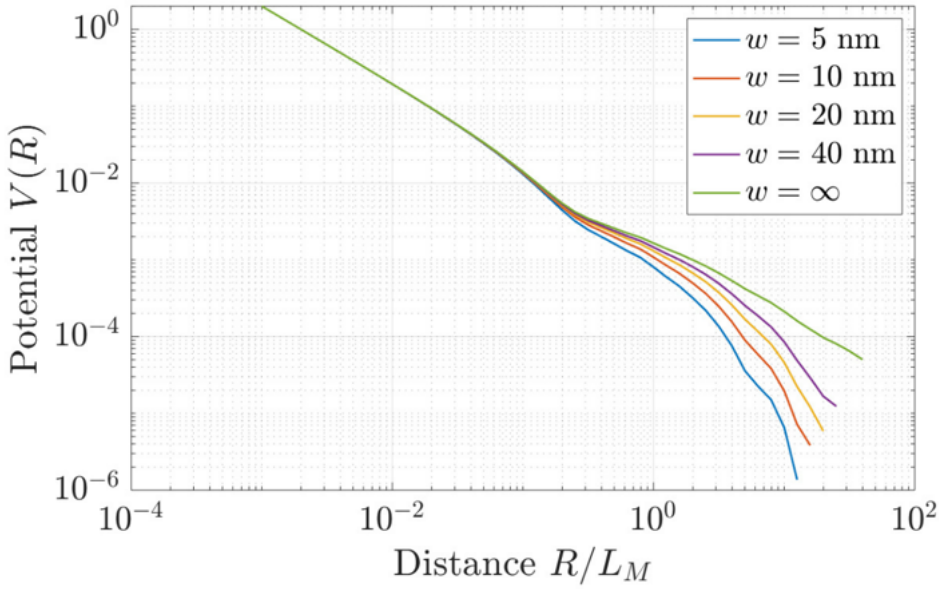

Fig. 7.3: Electron-electron interaction in MAG screened by graphite substrate. Shown is the dependence $V(R)$ vs. R for several different values of the hBN spacer thickness.

We numerically calculate the polarizability of tBLG using the electron bands obtained from the continuum model [114], within the random phase approximation. To suppress the screening effects due to the polarization of the flat bands, we put the Fermi level outside these bands. We then approximate Π_q to be isotropic and equal to its value for q in ΓM direction in the Brillouin zone. For very large q ($q \gg \frac{1}{L_M}$ where L_M is the moiré superlattice period), the quantity Π_q matches the polarizability value of two electrically decoupled stacked monolayer graphene layers,

$$\Pi_q \simeq 2\Pi_{q,MLG} = -\frac{qe^2}{2\hbar v_F} \tag{7.4}$$

where $v_F = 10^6$ m/s.

By taking an inverse Fourier transform, the screened interaction of two point charges e at distance R is obtained as,

$$V(R) = e^2 \int_0^\infty dq \frac{2J_0 qR}{1 + \kappa_{hBN} \coth qw - 4\Pi_q q} \tag{7.5}$$

Here, $J_n(x)$ is the Bessel function of the first kind. This gives a power law falloff, $V(R) \propto \frac{1}{R}$ for $R << w$ and a dependence that

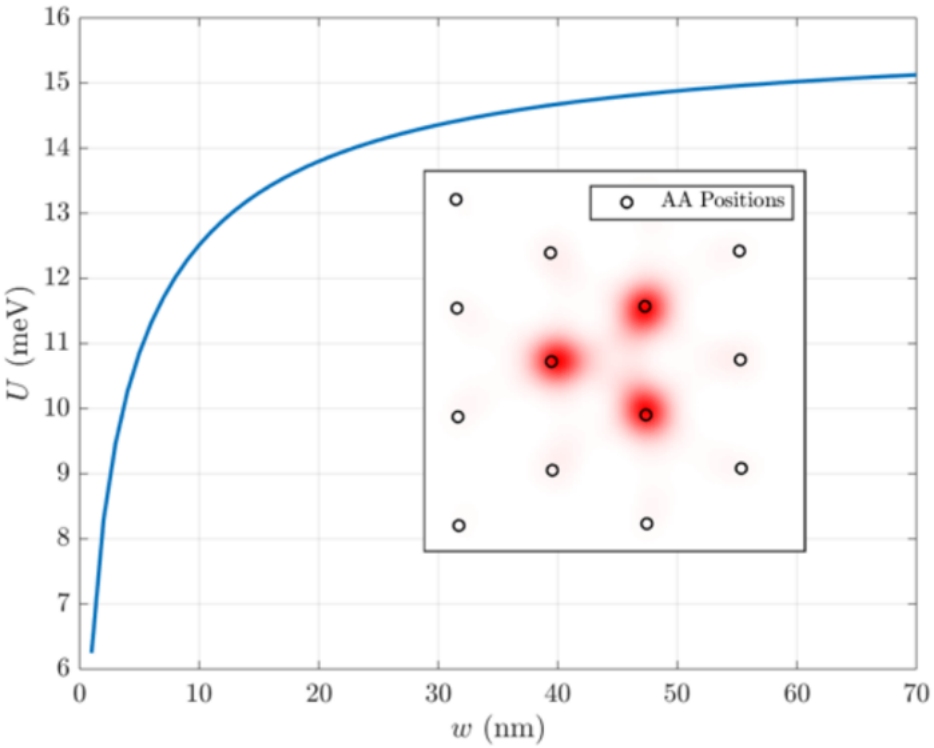

Fig. 7.4: The Hubbard interaction dependence U vs. hBN thickness w, for realistic Wannier functions obtained numerically for the MAG Hamiltonian using the continuum model (shown in the inset). Each Wannier function has three lobes located at AA positions of the moiré superlattice.

decays more rapidly at distances $R > w$. There is also a characteristic decrease in the potential in a bulge shaped feature at distances of the order of L_M, arising due to the difference between Π_q and $2\Pi_{q,MLG}$.

Next, we analyze the polarization charge density on the graphite surface, $\sigma(r)$, when an electron is localized on a tBLG Wannier orbital, $W(r)$. In order to do so, first, using the solution of Poisson's equation, Eq. 7.2, and Gauss' law, we can get the polarization charge on the graphite surface due to a point charge at $r = 0, G(r)$,

$$G(r) = -\int_0^\infty qdq \frac{\kappa_{hBN} J_0(qr)}{2\pi \sinh qw(1 + \kappa_{hBN} \coth qw - 4\pi\Pi_q/q)} \tag{7.6}$$

where r is the lateral distance on the surface of graphite from the point

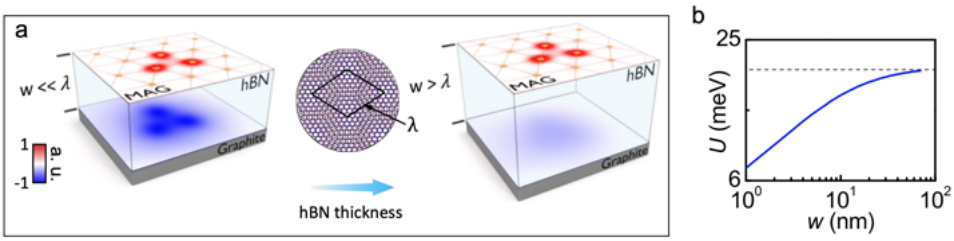

Fig. 7.5: **(a)** Wannier orbitals (red) in MATBG are screened by image charges on the graphite surface (blue), where λ is the moiré lattice constant and w is the hBN spacer thickness. **(b)** Calculated onsite Coulomb energy U versus w for $\theta = 1.05°$ (dashed line marks the unscreened value).

beneath the point charge. Then, we have,

$$\sigma(\mathbf{r}) = \int d^2\mathbf{r}\,' G(|\mathbf{r} - \mathbf{r}\,'|)|W(\mathbf{r}\,')^2| \tag{7.7}$$

The onsite Hubbard interaction, U, describes the energy cost of adding an electron to one of the Wannier orbitals that already holds one electron. Its dependence on the hBN thickness, w, can demonstrate the impact of screening on the Mott insulator. Using the potential V(R) in 7.5, U can be calculated as,

$$U = \int_0^\infty d^2\mathbf{x} d^2\mathbf{x}\,' |W(\mathbf{x})^2||W(\mathbf{x}\,')^2|V(|x - x\,'|) \tag{7.8}$$

The Wannier functions have a typical spatial extent of the order of L_M. Therefore, when the hBN thickness w is smaller than L_M, the screening effects discussed above result in a dramatic suppression of the Hubbard interaction. This behavior is illustrated in Figure 7.4.

Hence, the screening effect is a strong function of the distance between graphene and the metallic graphite layers. We have observed that as we keep decreasing this distance, the screening effect becomes a dominant parameter which decreases the Coulomb interaction between particles and changes the phase space of tBLG substantially.

If the distance w between MATBG and a metallic layer is made smaller than the moiré unit cell size, $w < \lambda \approx 15$ nm, polarization charges will screen out the Coulomb interactions on that scale and suppress U. In Figure 7.5**(a)** we have shown the schematics of the polarization charge for two different scenarios with different hBN thicknesses w. In the first case, w is much smaller than the moiré periodicity

λ, and the image charges are much closer than the second case. Hence the screening effect is stronger in the first case than in the second case. In Figure 7.5**(b)** we have plotted the U as a function of w. When the hBN thickness (w) is higher than $\sim$ 30 nm, we can neglect the screening effect in the system.

In the next section, we will elaborate this effect in different devices with different hBN thicknesses and with slightly different twist angles.

7.3 Comparison between different phase diagrams of MATBG

In the previous section, we have discussed the theoretical model for the Hubbard interaction ans how it changes with different screening lengths. However, another crucial parameter which determines the phase space of MATBG is the twist angle. The band width of MATBG, which dictates the correlation between particles is a strong function of the twist angle. Hence, we also have to consider the twist angle dependence of the phase space apart from the hBN thickness.

7.3.1 Different devices

We have measured three different devices (D1, D2 and D3) with parameters, $w_1 = 7$ nm, $\theta_1 = 1.15°$ (D1), $w_2 = 9.8$ nm, $\theta_2 = 1.04°$ (D2) and $w_3 = 12.5$ nm, $\theta_3 = 1.10°$ (D3).

The bottom hBN thickness is obtained from atomic force microscopy (AFM) measurements. Figure 7.6 demonstrates a set of MATBG heterostructures that have been used to fabricate the devices. The upper panel shows an optical image of the final graphite/hBN/MATBG/hBN stack. We find that the heterostructures exhibit high structural homogeneity and do not show visible bubble formations, which are known to locally distort the twist angle and charge carrier density. These observations are further confirmed by the AFM scans shown in the insets. The AFM scans are also used to extract the topography of the fabricated stacks where we find hBN thicknesses of $w \sim 7.0$ nm (D1), 9.8 nm (D2) and 12.5 nm (D3).

The difference in bottom dielectric thickness is further confirmed by measurement of the capacitance between the graphite and the MATBG layers. Extracted from the quantum oscillations map, we find that the

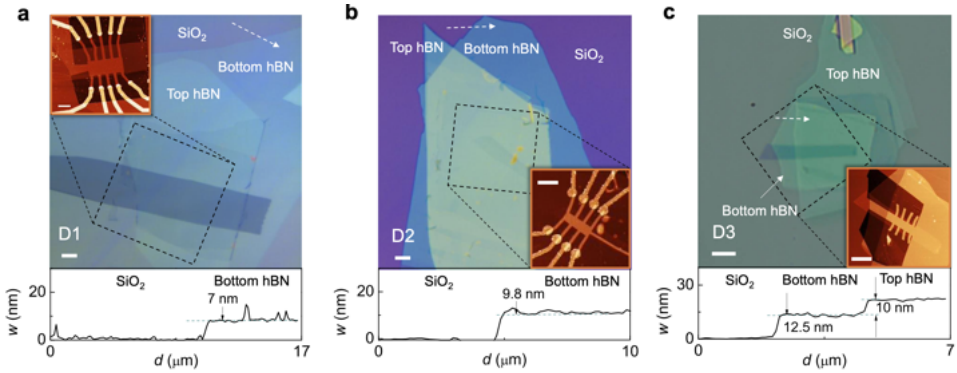

Fig. 7.6: AFM and optical images for samples D1(**(a)**), D2(**(b)**), and D3(**(c)**) The main panels are optical images of final stacks, from which all three devices were fabricated. The insets demonstrate AFM scans of the final devices etched into multi-terminal Hall bar geometries. Dashed black squares show AFM image areas. Bottom hBN thickness measurements are shown on the lower panel graphs. Height profiles are taken along the white dashed arrow lines. Scale bars are 5 μm.

back gate capacitance is 355 nF/cm^2 for D1, 260 nF/cm^2 for D2 and 221 nF/cm^2 for D3, This also matches with the extracted AFM height profiles.

7.3.2 Phase space of three devices

We used four terminal resistivity measurements (ρ_{xx}) to characterize the transport behaviour of the three devices mentioned above. The carrier density (n) was tuned by the graphite gates. The total carrier density, n was normalized by n_S, the density of the fully filled band, which defines the band filling factor, $\nu = n/n_S$.

The resistivity of each device is measured as a function of the band filling factor for a temperature range from $T = 40$ mK to 3 K. Figure 7.7 shows the colour plot of the resistivity ρ_{xx} as a function of filling factor, ν for several temperatures from $T = 40$ mK upto $T = 3$ K. Dark red regions correspond to highly resistive states and dark blue regions signify the zero or very low resistive states.

Notably, device D1, which has the thinnest w and a θ that is only slightly higher than the magic angle, demonstrates a phase diagram that is very different from those of all previously reported MATBG devices. This device does not show any insulating state at $\nu = \pm 2$. Its

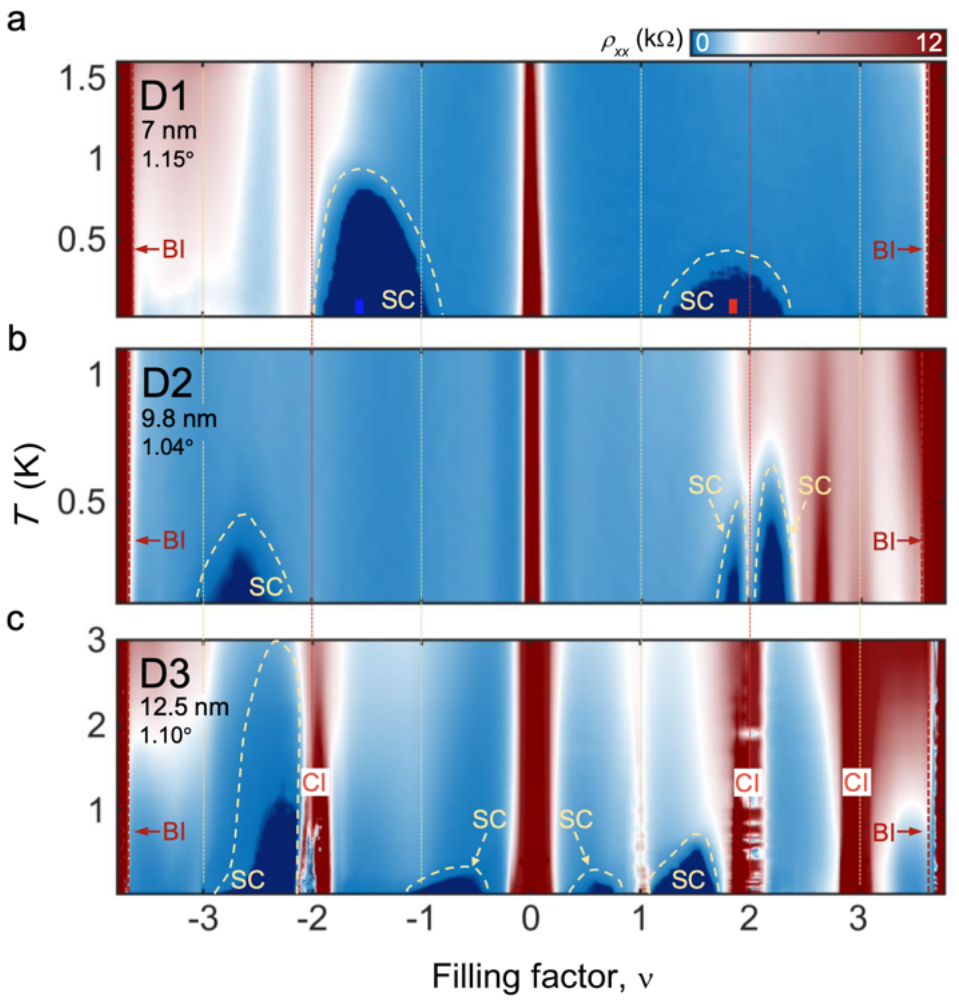

Fig. 7.7: Colour plot of ρ_{xx} as a function of ν and temperature T for three different devices, D1, D2 and D3. Signatures of correlated insulators (CI) are completely absent in devices with the thinnest w (D1 and D2), while superconductivity (SC) persists and T_c values remain virtually unaffected. BI stands for band insulator.

resistivity ρ_{xx} has metallic behaviour near and at the integer fillings and the absolute value of resistance never exceeds few kΩ. This observation suggests that there is no Fermi surface reconstruction at $\nu = \pm 2$ which is also evident from the lack of a new set of quantum oscillations originating from this point at perpendicular magnetic field. However, we have observed two broad superconducting domes at $\nu = \pm 2$. On

the electron side the superconducting dome is very strong and wide, taking the vacated space of the absent insulator at $\nu = +2$. We have also measured the superconducting transition temperature (T_c) of both the SCs from the typical 50% value of their normal state resistances. The T_c of these states is $T_c = 920$ mK and 420 mK for the SC at the valence and conduction band respectively. The primary distinguishing feature of this phase space is the absence of any correlated insulating state while having two strong superconducting domes at $\nu = \pm 2$.

This is in direct contrast to the phase space of the device D3. Device D3 has the thickest hBN with $w = 12.5$ nm and a twist angle which is exactly the magic angle ($\theta = 1.10°$). It shows prominent insulating peaks at all the integer fillings of the flat band. All the insulators are strongly dependent on the temperature. From the quantum oscillation behaviour, we have observed that a new sequence of oscillations originate from each of the integer fillings, which suggest a new Fermi surface reconstruction and the opening of mini gaps, induced by the correlation. Here the superconductivity domes directly flank the correlated insulators at integer fillings. These superconductors are similar to the previous studies. The T_c of these SCs vary from 150 mK to 3 K.

Since, this device is twisted exactly at magic angle, correlation is much stronger than other devices, hence the presence of all the insulators is explained. We argue that the band width of this device plays a prominent role here compared to D1 and D2.

Device D2, with an intermediate $w = 9.8$ nm value and a $\theta = 1.04°$, slightly smaller than θ_m, displays features present in both D1 and D3. Although it does not display correlated insulators in the valence band, it shows a single superconducting dome with a $T_c \approx 400$ mK. In the conduction band it features a non-activated resistance peak at $\nu = +2$, suggesting an underdeveloped correlated insulator, and two superconductivity domes flanking it, with $T_c \approx 500$ mK and $T_c \approx 650$ mK. All the three devices have a small insulating gap at charge neutrality point. It remains, however, unclear whether interaction or trivial band effects break the symmetry at the CNP.

The superconductivity in all the three devices was confirmed by a multitude of tests, including measurements of zero resistance and Fraunhofer interference patterns.

7.4 Interplay between correlated insulators and superconductors

In the previous section, we have shown that the correlated insulators and superconductors appear independently in the phase space depending on the hBN thickness w and the twist angle θ unlike the cuprates.

In Figure 7.8**(a)**, ρ_{xx} is plotted for the flat band in log scale for several temperatures from $T = 20$ mK to 5 K. Device D3 has all the resistance peaks at different integer fillings, and SCs flanking out of these states sending the resistance to zero. The lower panel in Figure

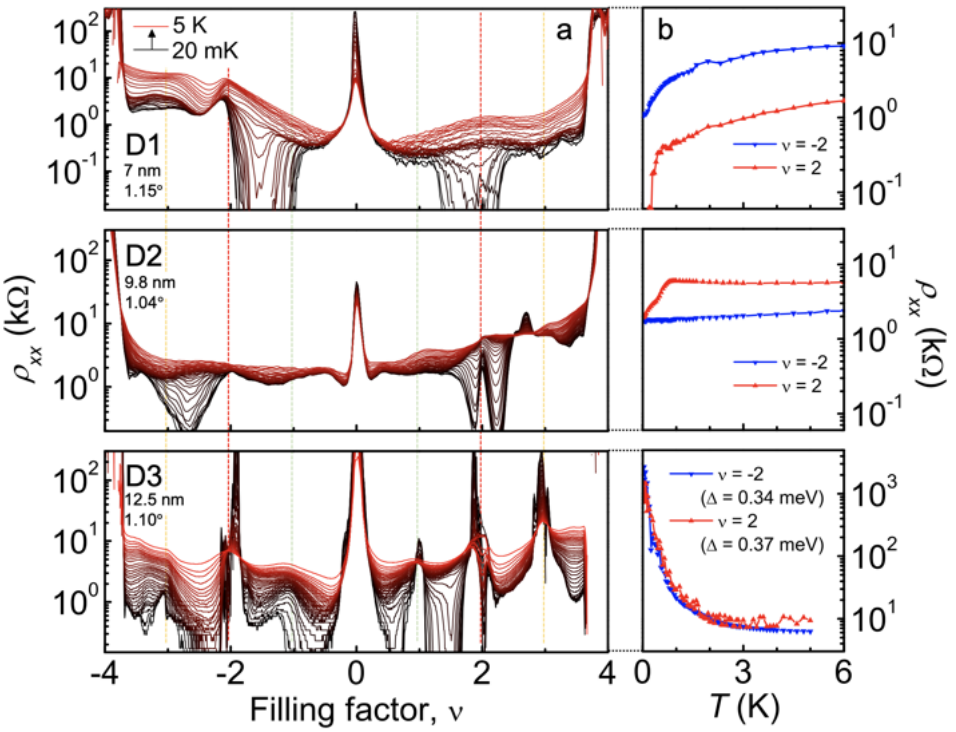

Fig. 7.8: The dependence of the superconductivity and correlated insulating phases on temperature and density. **(a)** Line cuts of resistivity ρ_{xx} versus filling factor ν, of devices D1, D2, D3, for different temperatures T from 20 mK to 5 K. **(b)** ρ_{xx} versus T for moiré band fillings of $\nu = \pm 2$ for each device. Although D1 and D2 show metallic behaviour in both valence and conduction bands, D3 shows strongly thermally activated behaviour, consistent with strong correlated insulating order.

7.8**(b)** represents the temperature dependence of the $\nu = \pm 2$ states. From the temperature activated behaviour ($\rho_{xx} \sim e^{\Delta/2k_BT}$) we calculated the gaps to be $\Delta = 0.37$ meV for the $\nu = +2$ state and $\Delta = 0.34$ meV for the $\nu = -2$ state.

Device D1 did not show any resistance peak except the CNP at $\nu = 0$. Although low temperature behaviour clearly shows two zero resistive states at $\nu = \pm 2$. The upper panel in Figure 7.8**(b)** corresponds to the temperature dependence of the $\nu = +2$ (red curve) and the $\nu = -2$ (blue curve) states. The half filling state in the conduction band has a clear superconducting transition and the valence band half filling state is at the edge of the SC dome.

Device D2 displays intermediate characteristics between D1 and D3. On the hole side, we did not observe any insulating behaviour at $\nu = -2$, as shown in the middle panel of 7.8**(a)**. It has a metallic behaviour as we have plotted the temperature dependence in Figure 7.8**(b)**. The electron side as well does not possess clear insulating behaviour. It has a non-activated resistance peak at $\nu = +2$, which is interrupted by two superconducting domes.

Overall, these findings clearly show that superconductivity can exist independent of correlated insulating states in MATBG, indicating that these phases are in competition with one another rather than sharing a common microscopic origin. Whereas insulating states are quenched in D1 and D2, the corresponding superconducting T_c values remain almost unaffected, falling in the same $T_c \approx 500$ mK – 1.5 K range that was previously reported for devices with similar twist angles, but in the presence of strong insulators. Because both the screening and bandwidth effects affect U/t, it is difficult to completely disentangle these effects from the data sets at present available. Comparison with the limited data from literature, however, indicates that screening may be a dominant effect in D1 ($\theta \approx 1.15°$) and D2 (1.04°), because these are the only reported devices that do not show any signatures of correlated insulating states so close to the magic angle of 1.1°.

These findings have certain implications regarding the origin of SC state in MATBG. The observed resilience of superconductivity upon suppression of the insulating phase is consistent with the two phases competing rather than being intimately connected. Such competition would be hard to reconcile with a common microscopic mechanism of the two phases as suggested by an analogy with cuprates. Instead, it appears that Coulomb interactions drive the formation of the corre-

lated insulators, whereas superconductivity arises from a more conventional mechanism. However, the anomalous character of superconductivity in MATBG, occurring at record low carrier densities, suggests that the electron-phonon mechanism, if present, is enhanced by the high density of states and electron correlation effects.

Chapter 8

Strange Metallicity in MATBG

From the time of its discovery, MATBG has been a constant debate regarding the origin of the different correlated quantum phenomena. Along with the other properties such as, correlated insulator, superconductor etc. strange metallicity is also an important phenomena that has been observed in this system. The observation of strange metallicity helps us to understand the electronic mechanism of the ground state of the system. In the previous studies, people have reported the temperature dependence of the resistivity of a series of twisted devices with a range of twist angle from $\theta = 0.75^\circ$ to $\theta = 2^\circ$ [115]. This study shows a linear temperature dependence (T) of the resistivity (ρ) over a wide range of temperature, hinting a dominant electron-phonon coupling in the system.

In another study [116], people have reported a T-linear resistivity over a small range of densities near the correlated insulators. This behaviour has also been observed in other strongly correlated systems such as ruthenates [117, 118], cobaltates [119, 120] etc. This behaviour in heavy fermion system is often termed as strange metallic state.

In this chapter, we will discuss the temperature dependence of a MATBG device in which all the correlated insulators are suppressed due to the screening by the metallic gate. The T-linear resistivity expands upto a very low temperature and also continues over a wide range of carrier densities. This typical behaviour is coined as the strange metal phase. The observation of this phase is also assisted by magneto-resistance measurements.

8.1 Resistivity in Landau's Fermi liquid theory

The electronic behaviour in a solid can be described by the Landau's Fermi liquid theory which predicts that the electrons in a solid can be treated as well-defined fermions despite their interactions. These electrons are called the quasiparticles with charge e, spin $1/2$ and mass m^*. This theory describes the normal behaviour of most of the metals at sufficiently low temperatures [121]. At low temperature, the heat transfer of the quasiparticles is given by their ability to transfer charge. This is given by a universal relation, called the Wiedemann-Franz (WF) law [122]. The WF law is one of the basic properties of a Fermi liquid, reflecting the fact that the ability of a quasiparticle to transport heat is the same as its ability to transport charge, provided it cannot lose energy through collisions. Empirically observed by Wiedemann and Franz in 1853, this law connects the electrical conductivity σ and the thermal conductivity κ of a metal by a universal constant,

$$\frac{\kappa}{\sigma T} = \frac{\pi^2}{3}\left(\frac{k_B}{e}\right)^2 \equiv L_0 \tag{8.1}$$

where T is the absolute temperature, k_B is the Boltzmann's constant and $L_0 = 2.45 \times 10^{-8} W\Omega K^{-2}$ is the Sommerfeld's value for the Lorentz ratio, $L = \kappa/\sigma T$.

The linear power of temperature in equation 8.1 comes from the linear temperature dependence of the fermionic specific heat, through the relation between heat transport and heat capacity. In kinetic theory,

$$\kappa = \frac{1}{3} cvl \tag{8.2}$$

where, c is the specific heat of the carriers, v is the average velocity and l is their mean free path.

If the mean free path l is considered to be independent of the temperature, the heat conduction has same temperature dependence as the specific heat when $T \to 0$. So, according to equation 8.1, it is also linear in T for electrons.

In this picture, the resistivity of the solid is given by,

$$\rho = \rho_0 + AT^2 \tag{8.3}$$

where ρ_0 is the residual resistivity attributed to the impurity scattering, and the second term A is the contribution of the electron-electron scattering.

In the next section, we will thoroughly present the resistivity of different twisted bilayer devices upto a very low temperature and discuss their behaviour in the light of Landau's Fermi liquid theory.

8.2 Temperature dependence of resistivity in MATBG

We have measured the detailed transport behaviour of eight devices with twist angles, D1 ($\theta = 1.04°$), D2 ($\theta = 1.10°$), D3 ($\theta = 1.03°$), D4 ($\theta = 1.02°$), D5 ($\theta = 1.30°$), D6 ($\theta = 1.40°$), D7 ($\theta = 1.50°$) and D8 ($\theta = 1.05°$) upto a very low temperature of $T = 40$ mK. In this study, we focused on the device D1 with ultra-close metallic screening layers in order to reveal the low temperature metallic states [36, 123]. As discussed in the previous chapter, all the correlated insulating states are suppressed by the screening effect, making the metallic states prominent upto a very low temperature in this device. We have measured the device over a broad range of parameter space with the carrier density tuned across the entire flat band and temperatures range from $T = 40$ mK to $T = 20$ K. This device contains superconducting domes both in conduction and valence bands even in the absence of the correlated insulators. We have noticed that the devices with twist angles close to magic angle θ_m, have linear T resistivity [115, 116] above $T > 1$ K and continues until $T = 40$ mK. This can not be explained by the electron-phonon coupling.

We have also investigated the magnetic field dependence of the resistivity. Resistivity (ρ) varies linearly with the magnetic field (B) inside the flat band, which is a typical signature of the strange metal behaviour. However, near the band edges, Fermi-liquid behaviour is restored and we found $\rho \sim (T^2, B^2)$. This Fermi liquid behaviour is also observed for the higher twist angle ($\theta > 1.3°$) devices.

In this section we will separately discuss the transport behaviour of both magic angle devices and higher twist angle devices in order to distinguish the differences between them.

8.2.1 Devices with twist angle close to magic angle

We have measured several devices with twist angle close to magic angle which show similar behaviour. Figure 8.1**(a)** represents four terminal longitudinal resistivity (ρ) of device D1 as a function of the band filling factor ($\nu(n_0)$). The black curve corresponds to $T = 40$ mK and top most light grey curve corresponds to $T = 20$ K. We have observed insulating behaviour at $\nu = 0$ (CNP) and at $\nu = \pm 4$ (BI).

Another insulating state was observed close to the band filling $\nu = +3$. Additionally, three SC domes were observed close to the half filling of both conduction and valence bands ($\nu = \pm 2$). In this device, the the separation between the metallic screening layer and graphene is smaller than the Wannier orbital size (~ 15 nm). Due to the screening effect all the correlated insulators at $\nu = \pm 2$ are suppressed leaving the entire valence band metallic except the SC dome.

This isospin Pomeranchuk effect was also observed, where the resistance peaks at $\nu = \pm 1$ are more pronounced at elevated T [124, 125]. The simple phase space of this device without any interruption of the correlated states allows us to thoroughly study the metallic ground state of the system.

We have focused on the evolution of the temperature dependence of the derivative of the resistivity ($(\partial\rho/\partial T)_\nu$) with respect to the band filling factor in Figure 8.1**(b)**. Typical insulating states are observed at CNP and at the band edges at $\nu = \pm 4$.

The details of this behaviour are illustrated in Figure 8.1**(c)** which presents the resistivity versus temperature for successive filling factors. Starting from the insulating regime at the charge neutrality point, metallicity is recovered at $\nu \approx -0.15$, which first shows a super-linear temperature dependence below $T < 15$ K and then saturates into a linear dependence [126]. With increased doping, the onset of the linear dependence is quickly shifted to lower temperatures. Starting from $\nu \approx 2$, the T-linear regime extends down to the base temperature and remains T-linear until a second super-linear regime is found for $\nu < -3.5$. This strange metal phase is only interrupted by a superconducting transition observed around half filling.

In order to understand the temperature dependence of the resistivity with actual power dependence, we have plotted $\rho(T) - \rho_0$ on a log-log scale in Figure 8.2. This allows us to trace down the resistivity over more than three orders of magnitude. We analysed the resistivity

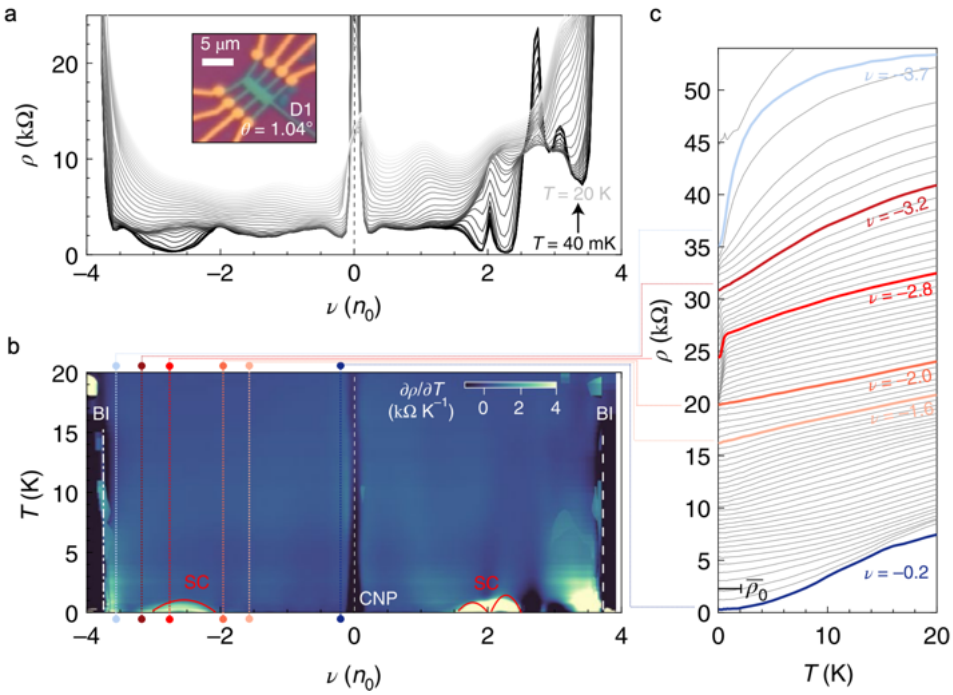

Fig. 8.1: Temperature dependence of the resistivity. **(a)** Resistivity (ρ) as a function of filling factor ($\nu(n_0)$) for several temperatures ranging from $T = 40$ mK (black curve) to $T = 20$ K (light grey). Inset shows the optical image of the device with twist angle $\theta = 1.04°$. **(b)** Colour plot of $\partial\rho/\partial T$ as a function of $\nu(n_0)$. Charge neutrality point (CNP), band insulator (BI) and superconducting domes (SC) are marked. Several line cuts along the dotted lines are plotted in **(c)**. **(c)** Temperature dependence of the resistivity in the hole doped side of the flat band. Dark blue line corresponds to the density near CNP, light orange to maroon colour curves are close to the SC dome at $\nu = -2$ and sky blue line corresponds to the curve near BI.

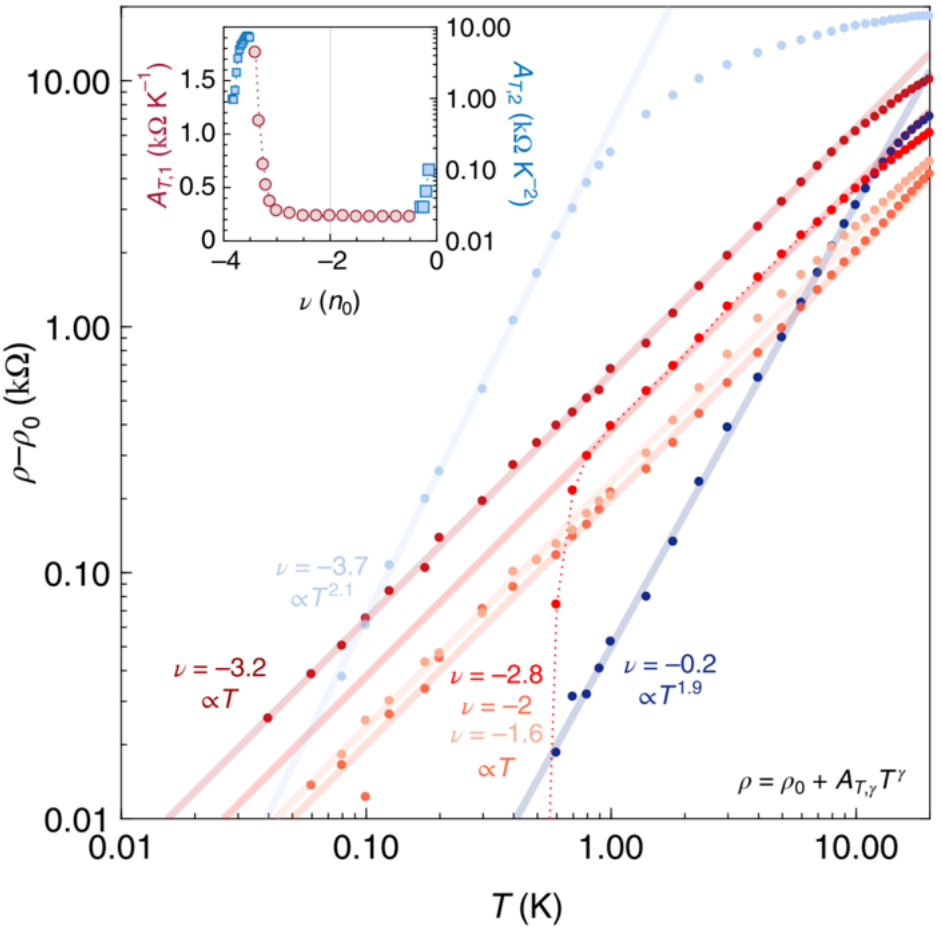

Fig. 8.2: Log-log plot of $(\rho(T) - \rho_0)$ versus T for the highlighted filling factors in 8.1 in the same colour. Power-law fits of the low T dependence are shown by straight lines. An evolution from a quadratic $\rho \propto T^2$ dependence near CNP and full filling, to a linear $\rho \propto T$ dependence inside the flat band region was seen. The inset shows the evolution of the pre-factor $A_{T,\gamma}$ upon doping both for the linear-in-T resistivity (left y axis) and the T-squared resistivity (right y axis).

by fitting it with $\rho(T) = \rho_0 + A_{\gamma,T}T^{\gamma}$. Where, $A_{\gamma,T}$ is the prefactor, γ is the exponent of the power dependence of the resistivity and ρ_0 is the residual resistance at T= 0. Each of the curve is fitted with $A_{\gamma,T}T^{\gamma}$ which results into a linear line in the log-log plot. In this analysis, γ is directly given by the slope of the line $\gamma = \partial[\ln(\rho(T) - \rho_0)]/\partial[\ln(T)]$. We have found that close to CNP ($\nu = -0.2$) and near BI ($\nu = -3.7$), $\gamma = 2 \pm 0.1$, which clearly shows the super-linear dependence of resistivity, i.e. $\rho \propto T^2$. However, inside the flat band, for the filling factor range $-3.7 < \nu < -0.2$, we have observed $\gamma \approx 1$ pointing towards the linear dependence of resistivity, $\rho \propto T$. This T-linear resistivity extends from the base temperature of 40 mK to 10 K without any interruption and it saturates above this temperature.

Similarly, we have also measured the temperature dependence of four more devices which are close to magic angle and exhibits similar behaviour. Figure 8.3 represents the temperature evolution of resistivity for four devices with twist angles $\theta = 1.10°$ (D2), $\theta = 1.03°$ (D3), $\theta = 1.02°$ (D4) and $\theta = 1.30°$ (D5). Devices D2 and D3 both showed a succession of low temperature superconducting and correlated insulating states in the center of the flat band region. These states make the metallic ground state hardly accessible. Yet, one remains able to see in D3 that the resistivity scales super linearly with temperature near the charge neutrality point and a T linear term develops in the core of the flat band (although here interrupted at low T by several phase transitions). This behaviour was also observed in devices D4 and D5 although these devices were not tracked below $T = 1.6$ K.

In both devices, we observed a clear evolution from a low temperature superlinear (parabolic) resistivity near charge neutrality into a T-linear resistivity extending down to the lowest temperatures in the center of the flat band. With further doping, the slope of this linear resistivity increased until a superlinear resistivity at low temperature was recovered.

We have summarized the behaviour of the magic angle devices (mainly device D1) in a schematics in Figure 8.4**(a)**.

The phase space, as illustrated in the schematics is mainly divided into two parts. Near the charge neutrality point and the band edges, resistivity is a quadratic function of the temperature ($\rho \propto T^2$). We associate this with the typical Fermi liquid behaviour of the carriers due to strong electron-electron scattering. Near the band edges, carrier concentration decreases and electron-electron scattering becomes a

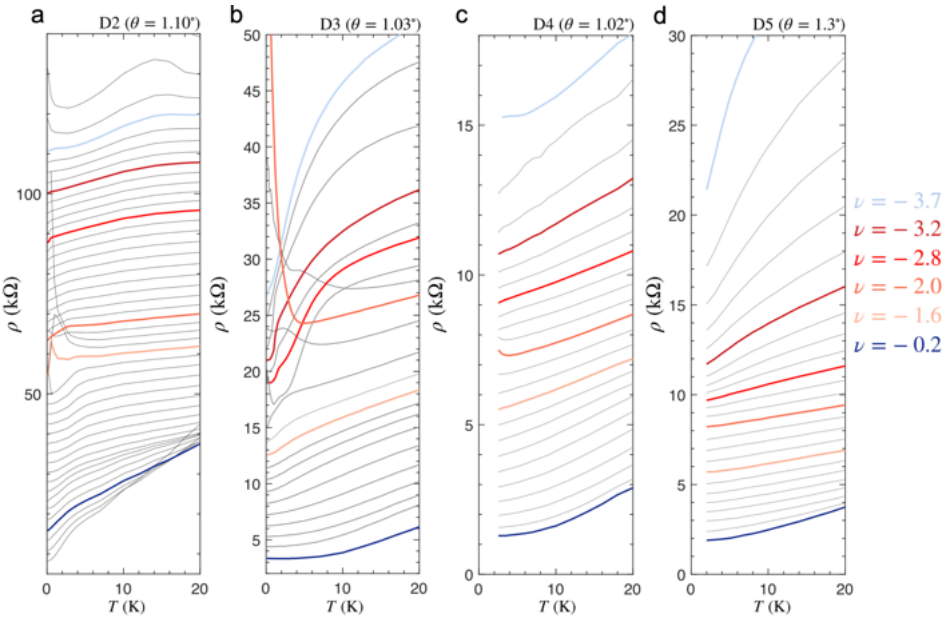

Fig. 8.3: Resistivity as a function of the temperature for several filling factors. **(a)** Device D2 with $\theta = 1.10°$. **(b)** Device D3 with $\theta = 1.03°$. **(c)** Device D4 with $\theta = 1.02°$. **(d)** Device D5 with $\theta = 1.30°$. Highlighted plots correspond to the filling factors as marked on the right. Linear-T resistivity behaviour was observed in all of these four devices.

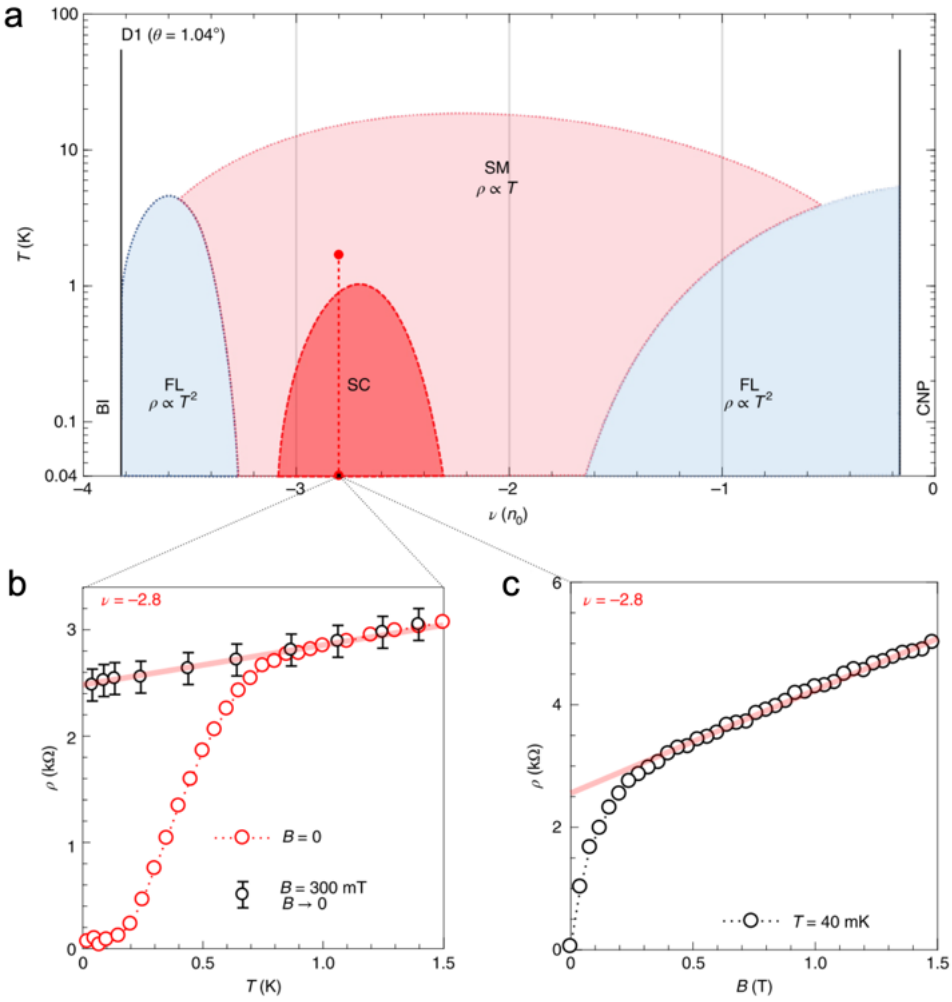

Fig. 8.4: Phase diagram of device D1. **(a)** Typical schematics of the (ν, T) phase space of the valence band of D1. SC is illustrated by the red dome in the middle of the SM phase inside the flat band. FL behaviour is observed close to the band edges (both near CNP and BI). **(b)** ρ as a function of the temperature for $\nu = -2.8$ at $B = 0$ and at $B_c = 300$ mT. Error bars correspond to the 95% confidence bound on the linear fit of the MR. **(c)** Evolution of the $\rho(T)$ as a function of the B at a $T = 40$ mK. A linear ρ is recovered by suppressing the SC upto $B = 1.5$ T. Red solid curve shows the linear MR.

dominant process in the transport. However, as we move further away from the band edges and reach inside the flat band, we observed two phase transition from quadratic T dependence to linear T dependence of the resistivity. This non Fermi liquid phase transition happens for a filling factor $-3.5 < \nu < -2$. Thus, it is tempting to identify the latter state as a strange metal above a quantum-critical phase, wherein the finite T metallic properties are dominated by critical fluctuations [127–132]. This behaviour can be explained by the famous Planckian scattering in strange metal phase in which the scattering rate is defined by the universal Planckian limit $1/\tau = k_B T/\hbar$. In this scenario, the scattering rate is uniquely defined by the Planckian limit and does not depend on the type of scattering in the system [133]. This type of T - linear resistivity was observed in other systems such as $La_{2-x}Sr_xCuO_4$ (LSCO) and $Bi_2Sr_2CaCu_2O_{8+x}$ (Bi2201) [134] down to $T \to 0$. This type of behaviour was associated with the reconstruction of the Fermi surface [135] and had been observed both at and far away from the critical point.

In the schematics of the phase diagram in Figure 8.4**(a)**, we have observed a broad superconducting dome close to the half filling of the hole-doped flat band which is illustrated by the red dome in the middle of the light red coloured strange metal phase ($\rho \propto T$) region. We could recover the strange metal phase by applying an out-of-plane magnetic field to the superconducting state. Figure 8.4**(b)** shows a line cut across the dotted red line in the phase space for $\nu = -2.8$. At zero magnetic field the superconducting transition happens at a temperature $T_c = 250$ mK as shown by the red scattered plot. However, application of a small magnetic field of $B_c = 300$ mT, we could recover the linear resistivity behaviour. This linear behaviour continues until a magnetic field of $B = 1.5$ T when we measured at $T = 40$ mK as plotted in Figure 8.4**(c)**. The recovery of the strange metal phase upon applying a small magnetic field has been observed in many strongly correlated systems before which are both superconducting and non-superconducting [136, 137].

8.2.2 Devices with twist angle far away from magic angle

Our report makes a convincing case that strong electronic correlations in the flat bands of MATBG drive the emergence of the low tem-

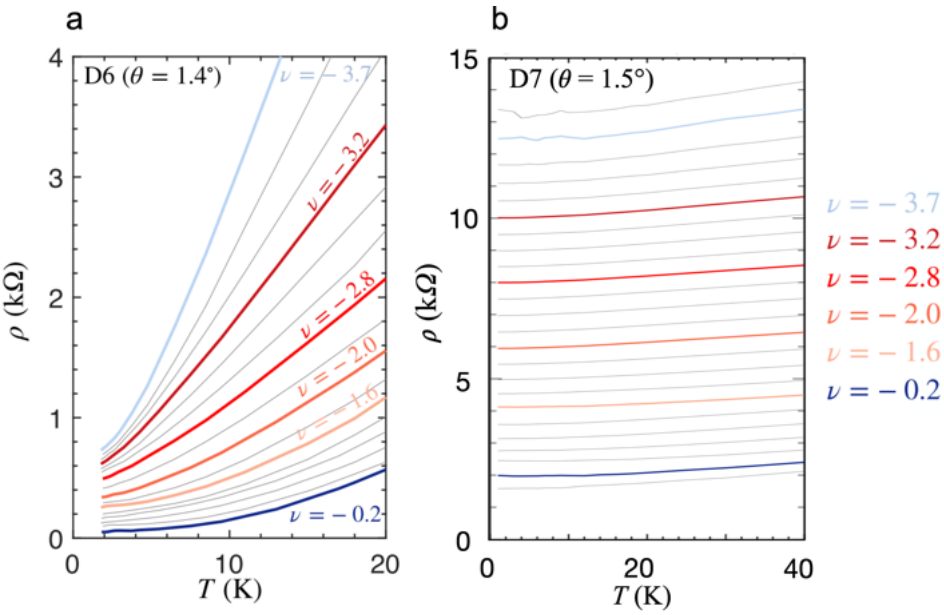

Fig. 8.5: **(a)** Resistivity (ρ) as. A function of T for several dopings in hole doped flat band of D6. Coloured line plots correspond to the same filling factor as described for D1 in the previous section. **(b)** Same ρ vs T plot with the highlighted coloured plots for the given ν for device D7.

perature linear resistivity in quantum critical scenario. To check this intricate connection, we explore in more detail other devices with twist angles that deviate from the magic angle. We studied couple of devices which have twist angle slightly higher than the magic angle (θ_m). In this section we will mainly focus on two devices, namely D6 ($\theta = 1.4°$) and D7 ($\theta = 1.5°$). Both devices D6 and D7 do not show any liner T resistivity in the entire hole doped flat band region. They have a quadratic T dependence of ρ.

Due to the higher twist angle of these devices, bandwidths are much higher than a typical MATBG, hence the correlation is weaker in these systems. They do not show signs of quantum critical behaviour, as it is highlighted in Figure 8.5. This shows ρ as a function of T for the same filling factors as discussed for D1 in the previous section. In contrast, we did not observe any linear T dependence for both the devices D6 and D7. Instead, we find a parabolic temperature dependence across the entire hole doped band.

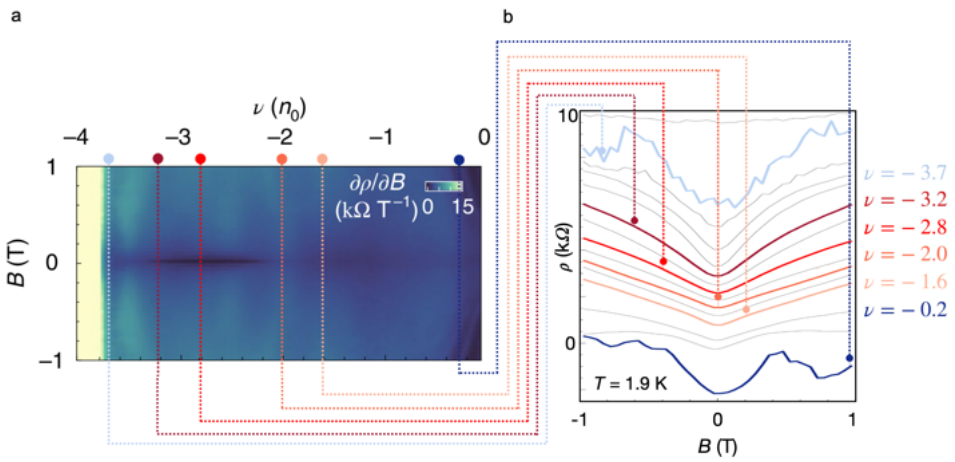

Fig. 8.6: **(a)** Colour plot of $\partial\rho/\partial B$ as a function of ν and B. **(b)** ρ as function of the B for several filling factors highlighted by the same colour as discussed in the T dependence.

The devices twisted further away from the magic angle show a T^2 - dependence, i.e. typical Fermi liquid behaviour, across their entire band at low temperatures. This suggests that electronic correlations in the Fermi liquid ground state are also enhanced near the magic angle.

8.3 Magnetic field dependence of resistivity

Besides the temperature dependence of the resistivity, another signature characteristics of the strange metal phase is the B - linear magnetoresistance. This behaviour has been observed in many superconducting and heavy fermion system and this delivers more evidence of the existence of the critical fluctuation interacting with the metallic ground state of the system. Figure 8.6**(a)** shows a colour plot of the numerical derivative of the resistivity ($\partial\rho/\partial B$) as a function of the filling factor ν and B for the same hole doped region of the flat band in device D1.

Several line cuts are plotted in Figure 8.6**(b)**, along the filling factors as discussed in the temperature dependence section in order to have a direct comparison between $\rho(T)$ and $\rho(B)$. WE have also performed a similar analysis of the power law dependence of the ρ by

fitting the parameter $\rho(B) = \rho_0 + A_{\gamma,B}B^{\gamma}$ in the log-log scale of ρ vs. B. The power dependence γ was calculated from the slope of this fitting curve, given by the equation,

From this analysis, we have observed a very similar behaviour as the T dependence. Near the CNP ($\nu = -0.2$) and BI ($\nu =$ -3.7), $\gamma \approx 2$ and inside the flat band ($-3.7 < \nu < -0.2$), we observed a linear B dependence, i.e. $\gamma \sim 1$.

8.4 Strange metal in MATBG

These findings make a clear case that MATBG possesses a Planckian limited T linear resistivity that extends down to a very low temperatures of 40 mK and occurs alongside a quantum B linear magnetoresistance. Such behaviour is incompatible with a Fermi liquid picture and conventional electron phonon scattering. The Fermi liquid behaviour is observed throughout the entire moiré band at non magic angles, by contrast, in MATBG it is pushed to the flat band edges. We therefore conclude that a strange metal phase exists, arising from a quantum critical region spanning a range of dopings including but not limited to those where the Fermi surface reconstructs and where quantum fluctuations dominate the metallic ground state of MATBG.

Chapter 9

Conclusion and Outlook

In this thesis, we have studied the transport behaviour of electrons in magic angle twisted bilayer graphene system. The experimental discovery of flat bands in MATBG started a new research field, called twistronics. These flat bands are proved to be a rich platform to study multiple strongly correlated phenomena. Strong interactions in these flat bands give rise to fascinating states of matter such as superconductivity, correlated insulator, magnetism etc. However, the exact mechanisms of these states are still not established as they are very challenging to study theoretically. Different approaches have been made in order to understand the ground state mechanism in MATBG. Similarly, we have applied an external magnetic field to study the phase space of this system and to understand what it can infer about the ground states. We have also increased the applied magnetic field to study the full Hofstadter spectrum of the twisted bilayer graphene superlattice.

We have discussed a detailed fabrication process of our magic angle twisted bilayer graphene devices in Chapter 3. Starting with the mechanical exfoliation of 2D materials on silicon oxide substrates, we described the process of making van der Waals heterostructures in multiple steps with great details. We have also pointed out few precautionary measures during the stacking process to increase the yield of devices.

Then we have moved to the experimental results. We have started by studying the detailed magnetoresistance behaviour of MATBG devices upto an external magnetic field of $B = 8$ T at a very low temper-

ature of $T = 40$ mK in Chapter 4. Before going into the experimental details, we have represented the theoretical construction of the Chern insulator in two dimensional lattice systems. In the first section of Chapter 4, we have started with the basic formalism of the Landau levels in two dimensional electron gas in the presence of an external magnetic field. We have continued with computing the Berry phase and Berry connection of the system and moved to calculate the Chern number of the bands from there. We have then calculated the formation of a Chern insulator in a honeycomb lattice which is similar to the Chern insulator in twisted bilayer graphene (TBG). After discussing a more general picture, in the next section we moved to TBG and elaborated different degeneracies and symmetries in this system. Correlation in MATBG breaks certain symmetries and open up the mini band gaps inside the flat bands. Due to the opening of these mini gaps, we observed separate Chern bands at different integer fillings of the flat band, which has been discussed in this section.

After this brief theoretical discussion, we moved to the experimental details in MATBG. We started with the basic characterization of our devices by measuring the temperature dependence of the resistivity. From the band insulating peaks and correlated insulating peaks at low temperature ($T < 20$ K), we determined if a device is twisted or not. We have calculated the twist angle of the devices by multiple ways from the magnetic field dependence of the longitudinal resistance (R_{xx}) and Hall resistance (R_{xy}). After the measurement of twist angle we selected the devices with twist angles close to magic angle for further measurements in dilution fridge down to $T = 40$ mK. The basic measurements of a magic angle device were discussed in the next section where we have observed superconductivity, correlated insulators and magnetic states inside the flat band. We have then moved on to studying the magnetic field dependence of three devices A1 ($\theta = 1.04°$), A2 ($\theta = 1.03°$) and A3 ($\theta = 1.10°$). We studied both longitudinal and Hall resistances of these devices at a lower magnetic field upto $B = 8$ T. We have observed quantized R_xy upon applying a small magnetic field at different integer fillings of the flat band which corresponds to Chern insulator with the Chern number given by the quantization. From several devices, we have also constructed a general schematics of the phase space of MATBG with Chern insulators, superconductors and correlated insulators marked in it. Furthermore in the last section of Chapter 4, we have calculated the gap of Chern insulators which vary

a lot from typical Landau levels gaps and generally much bigger than LL gaps.

In summary, our data provided a new and detailed view of the high B field phase diagram of MATBG and demonstrate its underlying topologically non-trivial properties. The topological nature of the flat bands in MATBG observed in this study has implications for the potential understanding of the superconducting phase, which needs to be understood on the basis of the ground states found here further, this could be considered as topological superconductivity. To further comprehend the microscopic mechanisms driving the Chern insulator and interactions between the various quantum states (Chern insulator, superconductor and orbital magnet), one possible direction is to control the correlated states by inducing dielectric screening or spin-orbital coupling in higher quality devices in further experiments.

After thoroughly studying the low magnetic field characteristics of MATBG in Chapter 4, we moved on to studying the high magnetic field Hofstadter spectrum of the flat band in Chapter 5. Moiré superlattices when placed in a sufficiently high magnetic field give rise to a fractal behaviour called Hofstadter spectrum. The periodicity of the moiré superlattice in MATBG is almost 3000 times bigger than the lattice period of graphene which makes the required magnetic field to reach one magnetic flux (Φ_0) in MATBG be much smaller. For a typical magic angle device the required magnetic field to reach Φ_0 is $B_0 = 25\theta^2 \sim 30$ T. In the first section of Chapter 5, we have started with the basic theoretical formalism of the Hofstadter spectrum in moiré system and then moved on to the observation of this phenomena in other 2D systems and finally discussed the spectrum in MATBG.

In the next section of Chapter 5, we demonstrated a detailed magneto-transport behaviour of a magic angle device upto a magnetic field of $B = 31$ T, sufficiently high to reach the Φ_0 in this device. Analysing the full magnetic field phase space, for the first time we observed re-entrant correlated insulator at integer fillings of the flat band close to the Φ_0. This observation experimentally verified the theoretical predictions that MATBG possesses flat band at Φ_0. We have also measured the temperature dependence and magnetic field dependence of the insulating states in order to compare them with the zero-field insulators and found out that the temperature activation gap size of the insulators at Φ_0 is bigger than the zero-field insulators. However, the magnetic

field dependence had a similar trend for both insulators at zero field and at Φ_0. The flat bands close to Φ_0 have a different symmetry and degeneracy than the zero-field flat bands and we have verified this by closely looked into the Landau levels that originated from different integer fillings. From the emerging LLs at different integer fillings we have illustrated the Fermi surface reconstruction and opening of mini band gaps at different integer fillings of the flat band at Φ_0.

In summary, we reported the first observation of interaction driven correlated insulating phases at one flux quantum per moiré unit cell in MATBG. Our experimental observations largely agreed with our single particle Hofstadter calculations, which predicted the emergence of a set of electronic flat bands at full flux with different symmetry and topology than the zero-field flat bands. These bands are unstable to the creation of correlated states by interactions.

Flat band in MATBG draws a lot of attention in the last few years as it gives rise to multiple correlated phenomena which are otherwise absent in a single system. However, the higher order dispersive bands in MATBG are also interesting and worth studying for. In Chapter 6 we have demonstrated the magneto-transport behaviour of the higher energy dispersive bands in MATBG. We started with the discussion of the band structure which has a Rashba-like structure and then we moved on to the discussion of Landau levels in these bands as we applied an external magnetic field. In Rashba-like bands, two sets of LLs emerge from each of the band and the cross each other at a particular magnetic field. We have calculated the Landau level crossings in this system and by fitting a parameter free term in the BM Hamiltonian and found a magic series of magnetic field (B^*) where the level crossings happened. We have then compared this theoretical model with our high quality experimental data and observed an excellent match between them. Our measurement of the experimental level crossings imposed constraints on the corrugation parameters which determine the band structure of the BM Hamiltonian. Our data provided a direct experimental verification of the theoretically calculated higher energy dispersive bands in MATBG for the first time.

We then moved on to studying the high magnetic field Hofstadter spectrum of these dispersive bands upto a magnetic field of Φ_0. The higher energy dispersive bands have higher bandwidth and are responsive to the single particle Hofstadter analysis. We have calculated a

series of LLs that emerged from the dispersive bands and experimentally tuned the carrier density beyond the flat bands ($\nu > 4$) to study these LLs. By carefully compared our experimental data with the theoretically predicted Chern numbers (C), we concluded that there are several LLs which matched perfectly with the single particle Hofstadter model. However, another set of LLs emerge from these bands which were not found in the single particle picture. We concluded that these levels can not be described by the single particle Hofstadter picture and needs interaction terms to explain.

In Chapter 7, we have studied the effect of Coulomb screening on the flat bands and on the correlated phenomena in MATBG. In both cuprates and in MATBG people have always observed the superconductor near an insulating state. The coexistence of these two phases immediately raise a question about their microscopic origin and interplay between them. It is well known that the electrostatic screening has a direct effect on the correlation in a system and in MATBG this screening can be tuned by changing the distance between graphene layers and the metallic gate. In the first section of Chapter 7, we have discussed the Mott-Hubbard model in a 2D lattice and compared the role of onsite energy (U) and hopping energy (t) in a lattice. We then moved on to calculate the screening in MATBG by considering the image charge problem with respect to the local gate. We found that the screening is effective when the distance (w) between the graphene layers and the gate is lesser than the typical Wannier orbital size (~ 15 nm) of the system.

Experimentally, we have measured the thorough temperature dependence of three devices D1, D2 and D3 with $\theta_1 = 1.15°$, $w_1 = 7$ nm, $\theta_2 = 1.04°$, $w_2 = 9.8$ nm and $\theta_3 = 1.10°$, $w_3 = 12.5$ nm respectively. By comparing the temperature dependent phase space of these three devices we found that device D1 which had the thinnest hBN and a θ slightly away from the magic angle demonstrated a phase space which is very different than other devices. In this device, we did not observe any correlated insulator at any integer filling of the flat band. However, there were two broad superconducting domes at $\nu = \pm 2$. In device D3, which had a thickest hBN and the twist angle is exactly magic angle, we observed all the correlated insulators at all the integer fillings and also we observed superconductor upon slightly doping away from the insulators. But device D2 showed an intermediate behavior in which

we have observed superconductors at $\nu = \pm 2$. Although it did not show any insulating state at the valence band, it had a non-activated resistance peak at $\nu = +2$, suggesting an underdeveloped correlated insulator.

Hence, in Chapter 7, we have demonstrated the screening effect on the phase space of three devices with slightly different twist angles and different hBN thicknesses. The observed resilience of superconductivity upon suppression of the insulating phase is consistent with the two phases competing rather than being intimately connected. Such competition would be hard to reconcile with a common microscopic mechanism of the two phases as suggested by an analogy with cuprates. However, a detailed and controlled study of the screening, keeping the twist angle same is required, in order to understand this mechanism better.

The temperature dependence of the resistivity inside the flat band gives us a lot of important information about the coupling mechanisms, either electron-electron or electron-phonon coupling in the system. Besides other correlated phenomena, we observed strange metallicity in MATBG. In Chapter 8 we have discussed the detailed temperature dependence of resistivity of twisted bilayer graphene devices over a wide range of twist angles from $\theta = 0.75^\circ$ to $\theta = 2^\circ$. We have mainly focused on a device with twist angle $\theta = 1.04^\circ$ and a screening layer placed closed than the Wannier orbital. Due to the screening effect, the correlated states are suppressed and we observed prominent metallic states upto a very low temperature. We observed that the devices with twist angle close to magic angle had a T-linear resistivity upto a very low temperature of $T = 40$ mK and as we moved towards the CNP of BI, the resistivity had quadratic dependence of T. Our observation also included a B-linear resistivity upon suppressing the superconducting state above B_c. However, for devices with twist angles away from magic angle, we did not observe any T-linear resistivity, rather the resistance showed a superlinear or quadratic dependence on both B and T ($\rho(T^2, B^2)$).

These findings make a clear case that MATBG possesses a Planckian-limited T-linear resistivity that extends down to unprecedentedly low temperatures of 40 mK and occurs alongside a quantum B-linear magnetoresistance. Such behaviour is incompatible with a Fermi-liquid picture and conventional electron-phonon scattering. The Fermi-liquid behaviour is observed throughout the entire moiré band at non-magic

angles, by contrast, in MATBG it is pushed to the flat band edges. We therefore concluded that a strange metal phase exists, arising from a quantum-critical region spanning a range of dopings including but not limited to those where the Fermi surface reconstructs and where quantum fluctuations dominate the metallic ground state of MATBG.

9.1 List of Publications

- **Das, I.**, Shen, C., Jaoui, A., Herzog-Arbeitman, J., Chew, A., Cho, C. W., Watanabe, K., Taniguchi, T., Piot, B. A., Bernevig, B. A. and Efetov, D. K. Observation of Re-entrant Correlated Insulators and Interaction-Driven Fermi-Surface Reconstruction at One Magnetic Flux Quantum per Moiré Unit Cell in Magic-Angle Twisted Bilayer Graphene. *Phys. Rev. Lett.* **128**, 217701 (2022).

- **Das, I.**, Lu, X., Herzog-Arbeitman, J., Song, Z., Watanabe, K., Taniguchi, T., Bernevig, B. A. and Efetov, D. K. Symmetry-broken Chern Insulators and Rashba-like Landau level crossings in magic-angle bilayer graphene. *Nature Physics* **17**, 710-714 (2021).

- Jaoui, A., **Das, I.**, Di Battista, G., Diez-Mérida, J., Lu, X., Watanabe, K., Taniguchi, T., Ishizuka, H., Levitov, L. and Efetov, D. K. Quantum critical behaviour in magic-angle twisted bilayer graphene. *Nature Physics* **18**, 633 (2022).

- Stepanov, P., **Das, I.**, Lu, X., Fahimniya, A., Watanabe, K., Taniguchi, T., Koppens, F. H., Lischner, J., Levitov, L. and Efetov, D. K. Untying the insulating and superconducting orders in magic-angle twisted bilayer graphene. *Nature* **583**, 375-378 (2020).

- Lu, X., Stepanov, P., Yang, W., Xie, M., Aamir, M. A., **Das, I.**, Urgell, C., Watanabe, K., Taniguchi, T., Zhang, G., Bachtold, A., MacDonald, A. H. and Efetov, D. K. Superconductors, orbital magnets and correlated states in magic-angle bilayer graphene. *Nature* **574**, 653-657 (2019).

9.2 Future directions

In this thesis, we have only explored the moiré superlattices of graphene, a 2D hexagonal lattice of carbon atoms and observed many rich correlated phenomena. Based on the recent developments of this moiré system, there is now a new field of research, called **twistronics**, in particular **magic-angle twistronics**, aiming at exploiting this novel degree of freedom to its extremes. This field is expanding quickly and absorbing many great scientists. It shall be expected that soon in the future we will have a more detailed complete understanding of the magic angle phenomenology.

Following the first result on the observation of superconductivity in MATBG, there are plenty of other experiments, both studying the superconductivity [36, 92, 138], as well as other interesting phenomena resulting from the flatness and topology of the bands, including a strange metal phase [37] and quantum anomalous Hall effect in the hBN aligned devices [139, 140]. All of these discoveries make MATBG a rich system with strong correlation and with nontrivial band topology.

On the theory side, there have been hundreds of papers that investigate a variety of topics, from the origin of the magic angles, to possible mechanisms of the superconductivity, and its number is still quickly growing [141–145]. However, while experimental evidence generally points towards a strongly correlated superconductivity, the true origin of this phase is still heavily debated by the theorists.

Surprisingly, despite its elusive origin, superconductivity in MATBG is already finding itself potential applications, faster than many other frontier materials in condensed matter physics. One of the main approach is to make Josephson junction out of these superconducting states. There has been already few experiments performed in this system [146–148] to explore the Josephson junction effect on the superconductivity. However, multiple studies can be performed in order to understand the microscopic mechanism of the superconductivity.

Another direction is to study the thermal properties of MATBG. It is recently proposed [149] that the small heat capacity of MATBG might make it suitable as a single-photon detector, in particular in mid-infrared to terahertz frequencies. There are already initial results on the thermal properties of the superconductor in MATBG [150]. However, there remains a lot of opportunities in this field to be explored

in the future.

As the direct extension of the work done in this thesis, we have several directions of research that can be performed in the future.

- One of the interesting topics concerns the Coulomb screening of the correlation inside the flat band of MATBG. In all the studies [36, 138], the screening layers have been varied in different devices with slightly different twist angles. However, one of the main parameters that dictates the correlation in this system is the band width of the flat band. The band width is a strong function of twist angle in MATBG. Hence, studying the screening effect in multiple devices with slightly different twist angles is not quantitatively conclusive. We can now fabricate a single device with a single twist angle on a substrate which has a very high dielectric constant. For this purpose, we will use $SrTiO_3$ (STO) substrate which has much higher dielectric constant than hBN [151–153]. We will fabricate our MATBG devices on top of this substrate. One part of the device will not be covered with hBN and be directly gated through the dielectrics of STO and another part will be covered with hBN and will be gated through the graphite gate. Due to the different dielectric environment in STO and hBN, we expect to see a variation in correlation of the charge carriers in these two parts. Hence, the overall phase space of a single twisted bilayer graphene device is expected to be different depending on the dielectric environments.

- In this thesis, we have explored the high magnetic field behaviour of MATBG devices and observed the re-entrance of the flat band at a magnetic field corresponds to one magnetic flux quantum per moiré unit cell. This result is evidenced by the observation of a set of correlated insulators at different integer fillings of the flat band. However, an immediate question arises about the existence of superconductivity in this flat band similar to the scenario as zero-field. We will fabricate MATBG devices with high homogeneity, so that the relative change in twist angle does not alter the magnetic field required to reach one magnetic flux quantum per moiré unit cell. This is important as the critical magnetic filed of the superconductor in MATBG is quite small ($H_c \sim 50 - 70$ mT) in general. We will perform magnetoresistance measurements on these highly homogeneous MATBG

devices upto $B = 36$ T.

Bibliography

1. L. D. Landau, E. M. L. *Statistical Physics, Second Revised and Enlarged Edition* 2nd ed. (Pergamon Press, 1969).
2. Peierls, R. Quelques propriétés typiques des corps solides. fr. *Annales de l'institut Henri Poincaré* **5,** 177–222 (1935).
3. Mermin, N. D. Crystalline Order in Two Dimensions. *Phys. Rev.* **176,** 250–254 (1 1968).
4. Novoselov, K. S., Geim, A. K., Morozov, S. V., Jiang, D., Zhang, Y., Dubonos, S. V., Grigorieva, I. V. & Firsov, A. A. Electric Field Effect in Atomically Thin Carbon Films. *Science* **306,** 666–669 (2004).
5. Geim, A. K. & Novoselov, K. S. The rise of graphene, 11–19 (2010).
6. Castro Neto, A. H., Guinea, F., Peres, N. M. R., Novoselov, K. S. & Geim, A. K. The electronic properties of graphene. *Rev. Mod. Phys.* **81,** 109–162 (1 2009).
7. Manzeli, S., Ovchinnikov, D., Pasquier, D., Yazyev, O. V. & Kis, A. 2D transition metal dichalcogenides. *Nature Reviews Materials* **2,** 1–15 (2017).
8. Saito, Y., Nojima, T. & Iwasa, Y. Highly crystalline 2D superconductors. *Nature Reviews Materials* **2,** 1–18 (2016).
9. Gibertini, M., Koperski, M., Morpurgo, A. F. & Novoselov, K. S. Magnetic 2D materials and heterostructures. *Nature nanotechnology* **14,** 408–419 (2019).
10. Qian, X., Liu, J., Fu, L. & Li, J. Quantum spin Hall effect in two-dimensional transition metal dichalcogenides. *Science* **346,** 1344–1347 (2014).

11. Zhang, Y., Tan, Y.-W., Stormer, H. L. & Kim, P. Experimental observation of the quantum Hall effect and Berry's phase in graphene. *nature* **438,** 201–204 (2005).

12. Novoselov, K. S., Geim, A. K., Morozov, S. V., Jiang, D., Katsnelson, M. I., Grigorieva, I., Dubonos, S. & Firsov, a. Two-dimensional gas of massless Dirac fermions in graphene. *nature* **438,** 197–200 (2005).

13. Meyer, J. C., Geim, A. K., Katsnelson, M. I., Novoselov, K. S., Booth, T. J. & Roth, S. The structure of suspended graphene sheets. *Nature* **446,** 60–63 (2007).

14. Nelson, D., Piran, T. & Weinberg, S. *Statistical mechanics of membranes and surfaces* (World Scientific, 2004).

15. Wallace, P. R. The Band Theory of Graphite. *Phys. Rev.* **71,** 622–634 (9 1947).

16. Geim, A. K. & Grigorieva, I. V. Van der Waals heterostructures. *Nature* **499,** 419–425 (2013).

17. Novoselov, K. S., Mishchenko, A., Carvalho, A. & Neto, A. H. C. 2D materials and van der Waals heterostructures. *Science* **353,** aac9439 (2016).

18. Haigh, S. J., Gholinia, A., Jalil, R., Romani, S., Britnell, L., Elias, D. C., Novoselov, K. S., Ponomarenko, L. A., Geim, A. K. & Gorbachev, R. Cross-sectional imaging of individual layers and buried interfaces of graphene-based heterostructures and superlattices. *Nature materials* **11,** 764–767 (2012).

19. Pizzocchero, F., Gammelgaard, L., Jessen, B. S., Caridad, J. M., Wang, L., Hone, J., Bøggild, P. & Booth, T. J. The hot pick-up technique for batch assembly of van der Waals heterostructures. *Nature communications* **7,** 1–10 (2016).

20. Dean, C. R., Young, A. F., Meric, I., Lee, C., Wang, L., Sorgenfrei, S., Watanabe, K., Taniguchi, T., Kim, P., Shepard, K. L., *et al.* Boron nitride substrates for high-quality graphene electronics. *Nature nanotechnology* **5,** 722–726 (2010).

21. Xue, J., Sanchez-Yamagishi, J., Bulmash, D., Jacquod, P., Deshpande, A., Watanabe, K., Taniguchi, T., Jarillo-Herrero, P. & LeRoy, B. J. Scanning tunnelling microscopy and spectroscopy of ultra-flat graphene on hexagonal boron nitride. *Nature materials* **10,** 282–285 (2011).

22. Bolotin, K., Sikes, K., Jiang, Z., Klima, M., Fudenberg, G., Hone, J., Kim, P. & Stormer, H. Ultrahigh electron mobility in suspended graphene. *Solid State Communications* **146,** 351–355 (2008).

23. Feldman, B. E., Krauss, B., Smet, J. H. & Yacoby, A. Unconventional Sequence of Fractional Quantum Hall States in Suspended Graphene. *Science* **337,** 1196–1199 (2012).

24. Sata, Y., Moriya, R., Masubuchi, S., Watanabe, K., Taniguchi, T. & Machida, T. N and p type carrier injections into WSe2 with van der Waals contacts of two-dimensional materials. *Japanese Journal of Applied Physics* **56,** 04CK09 (2017).

25. Ajayan, P. M., Kim, P. & Banerjee, K. Two-dimensional van der Waals materials. *Physics Today* **69,** 38–44 (2016).

26. Cao, Y., Fatemi, V., Demir, A., Fang, S., Tomarken, S. L., Luo, J. Y., Sanchez-Yamagishi, J. D., Watanabe, K., Taniguchi, T., Kaxiras, E., *et al.* Correlated insulator behaviour at half-filling in magic-angle graphene superlattices. *Nature* **556,** 80–84 (2018).

27. Cao, Y., Fatemi, V., Fang, S., Watanabe, K., Taniguchi, T., Kaxiras, E. & Jarillo-Herrero, P. Unconventional superconductivity in magic-angle graphene superlattices. *Nature* **556,** 43–50 (2018).

28. Jindal, A., Jangade, D., Kumar, N., Vaidya, J., Das, I., Bapat, R., Parmar, J., Chalke, B., Thamizhavel, A., Deshmukh, M. & Aldrich, S. Growth of high-quality Bi 2 Sr 2 CaCu 2 O 8+ whiskers and electrical properties of resulting exfoliated flakes. *Scientific Reports* **7,** 3295 (2017).

29. Biscaras, J., Bergeal, N., Kushwaha, A., Wolf, T., Rastogi, A., Budhani, R. C. & Lesueur, J. Two-dimensional superconductivity at a Mott insulator/band insulator interface LaTiO3/SrTiO3. *Nature communications* **1,** 1–5 (2010).

30. Chang, C.-Z., Zhang, J., Feng, X., Shen, J., Zhang, Z., Guo, M., Li, K., Ou, Y., Wei, P., Wang, L.-L., *et al.* Experimental observation of the quantum anomalous Hall effect in a magnetic topological insulator. *Science* **340,** 167–170 (2013).

31. Tamegai, T., Yamada, R., Ooi, S., Shibauchi, T., Murayama, C. & Mori, N. Effects of hydrostatic pressure and oxygen doping on the vortex phase diagram in Bi2Sr2CaCu2O8+y. *Physica C: Superconductivity and its Applications* **282-287,** 2029–2030 (1997).

32. Barns, R. & Laudise, R. Stability of superconducting YBa2Cu3O7 in the presence of water. *Applied physics letters* **51,** 1373–1375 (1987).

33. Andrei, E. Y., Efetov, D. K., Jarillo-Herrero, P., MacDonald, A. H., Mak, K. F., Senthil, T., Tutuc, E., Yazdani, A. & Young, A. F. The marvels of moiré materials. *Nature Reviews Materials* **6,** 201–206 (2021).

34. Das, I., Lu, X., Herzog-Arbeitman, J., Song, Z., Watanabe, K., Taniguchi, T., Bernevig, B. A. & Efetov, D. K. Symmetry-broken Chern insulators and Rashba-like Landau-level crossings in magic-angle bilayer graphene. *Nature Physics* **17,** 710–714 (2021).

35. Das, I., Shen, C., Jaoui, A., Herzog-Arbeitman, J., Chew, A., Cho, C.-W., Watanabe, K., Taniguchi, T., Piot, B. A., Bernevig, B. A. & Efetov, D. K. Observation of Reentrant Correlated Insulators and Interaction-Driven Fermi-Surface Reconstructions at One Magnetic Flux Quantum per Moiré Unit Cell in Magic-Angle Twisted Bilayer Graphene. *Phys. Rev. Lett.* **128,** 217701 (21 2022).

36. Stepanov, P., Das, I., Lu, X., Fahimniya, A., Watanabe, K., Taniguchi, T., Koppens, F. H., Lischner, J., Levitov, L. & Efetov, D. K. Untying the insulating and superconducting orders in magic-angle graphene. *Nature* **583,** 375–378 (2020).

37. Jaoui, A., Das, I., Di Battista, G., Dıez-Mérida, J., Lu, X., Watanabe, K., Taniguchi, T., Ishizuka, H., Levitov, L. & Efetov, D. K. Quantum critical behaviour in magic-angle twisted bilayer graphene. *Nature Physics,* 1–6 (2022).

38. Goerbig, M. & Montambaux, G. *Dirac fermions in condensed matter and beyond* 25–53 (Springer, 2017).

39. Haldane, F. D. M. Model for a Quantum Hall Effect without Landau Levels: Condensed-Matter Realization of the "Parity Anomaly". *Phys. Rev. Lett.* **61,** 2015–2018 (18 1988).

40. McCann, E. Asymmetry gap in the electronic band structure of bilayer graphene. *Phys. Rev. B* **74,** 161403 (16 2006).

41. Dresselhaus, M. S. & Dresselhaus, G. Intercalation compounds of graphite. *Advances in Physics* **51,** 1–186 (2002).

42. Moon, P. & Koshino, M. Energy spectrum and quantum Hall effect in twisted bilayer graphene. *Phys. Rev. B* **85,** 195458 (19 2012).

43. Trambly de Laissardière, G., Mayou, D. & Magaud, L. Localization of Dirac electrons in rotated graphene bilayers. *Nano letters* **10,** 804–808 (2010).

44. Suárez Morell, E., Correa, J. D., Vargas, P., Pacheco, M. & Barticevic, Z. Flat bands in slightly twisted bilayer graphene: Tight-binding calculations. *Phys. Rev. B* **82,** 121407 (12 2010).

45. Lopes dos Santos, J. M. B., Peres, N. M. R. & Castro Neto, A. H. Continuum model of the twisted graphene bilayer. *Phys. Rev. B* **86,** 155449 (15 2012).

46. Mele, E. J. Commensuration and interlayer coherence in twisted bilayer graphene. *Phys. Rev. B* **81,** 161405 (16 2010).

47. Uri, A., Grover, S., Cao, Y., Crosse, J. A., Bagani, K., Rodan-Legrain, D., Myasoedov, Y., Watanabe, K., Taniguchi, T., Moon, P., *et al.* Mapping the twist-angle disorder and Landau levels in magic-angle graphene. *Nature* **581,** 47–52 (2020).

48. Zou, L., Po, H. C., Vishwanath, A. & Senthil, T. Band structure of twisted bilayer graphene: Emergent symmetries, commensurate approximants, and Wannier obstructions. *Phys. Rev. B* **98,** 085435 (8 2018).

49. Kim, C.-J., Sánchez-Castillo, A., Ziegler, Z., Ogawa, Y., Noguez, C. & Park, J. Chiral atomically thin films. *Nature nanotechnology* **11,** 520–524 (2016).

50. Slater, J. C. & Koster, G. F. Simplified LCAO Method for the Periodic Potential Problem. *Phys. Rev.* **94,** 1498–1524 (6 1954).

51. Rozhkov, A. V., Sboychakov, A. O., Rakhmanov, A. L. & Nori, F. Single-electron gap in the spectrum of twisted bilayer graphene. *Phys. Rev. B* **95,** 045119 (4 2017).

52. Cao, Y., Luo, J. Y., Fatemi, V., Fang, S., Sanchez-Yamagishi, J. D., Watanabe, K., Taniguchi, T., Kaxiras, E. & Jarillo-Herrero, P. Superlattice-Induced Insulating States and Valley-Protected Orbits in Twisted Bilayer Graphene. *Phys. Rev. Lett.* **117,** 116804 (11 2016).

53. Wang, L., Meric, I., Huang, P. Y., Gao, Q., Gao, Y., Tran, H., Taniguchi, T., Watanabe, K., Campos, L. M., Muller, D. A., Guo, J., Kim, P., Hone, J., Shepard, K. L. & Dean, C. R. One-Dimensional Electrical Contact to a Two-Dimensional Material. *Science* **342,** 614–617 (2013).

54. Kim, J., Kim, F. & Huang, J. Seeing graphene-based sheets. *Materials Today* **13,** 28–38 (2010).

55. Blake, P., Hill, E. W., Castro Neto, A. H., Novoselov, K. S., Jiang, D., Yang, R., Booth, T. J. & Geim, A. K. Making graphene visible. *Applied Physics Letters* **91,** 063124 (2007).

56. An, J. Y. & Kahng, Y. H. Optical observation of single layer graphene on silicon nitride substrate. *AIP Advances* **8,** 015107 (2018).

57. Hattori, Y., Taniguchi, T., Watanabe, K. & Kitamura, M. Enhancement of the contrast for a hexagonal boron nitride monolayer placed on a silicon nitride/silicon substrate. *Applied Physics Express* **15,** 086502 (2022).

58. Musumeci, C. Advanced Scanning Probe Microscopy of Graphene and Other 2D Materials. *Crystals* **7** (2017).

59. Frisenda, R., Navarro-Moratalla, E., Gant, P., Pérez De Lara, D., Jarillo-Herrero, P., Gorbachev, R. V. & Castellanos-Gomez, A. Recent progress in the assembly of nanodevices and van der Waals heterostructures by deterministic placement of 2D materials. *Chem. Soc. Rev.* **47,** 53–68 (1 2018).

60. Caldwell, J. D., Anderson, T. J., Culbertson, J. C., Jernigan, G. G., Hobart, K. D., Kub, F. J., Tadjer, M. J., Tedesco, J. L., Hite, J. K., Mastro, M. A., *et al.* Technique for the dry transfer of epitaxial graphene onto arbitrary substrates. *ACS nano* **4,** 1108–1114 (2010).

61. Bistritzer, R. & MacDonald, A. H. Moiré bands in twisted double-layer graphene. *Proceedings of the National Academy of Sciences* **108,** 12233–12237 (2011).

62. Song, Z., Wang, Z., Shi, W., Li, G., Fang, C. & Bernevig, B. A. All Magic Angles in Twisted Bilayer Graphene are Topological. *Phys. Rev. Lett.* **123,** 036401 (3 2019).

63. Bernevig, B. A. *3. Hall Conductance and Chern Numbers* 15–32 (Princeton University Press, Princeton, 2013).

64. Young, A. F., Dean, C. R., Wang, L., Ren, H., Cadden-Zimansky, P., Watanabe, K., Taniguchi, T., Hone, J., Shepard, K. L. & Kim, P. Spin and valley quantum Hall ferromagnetism in graphene. *Nature Physics* **8,** 550–556 (2012).

65. Nomura, K. & MacDonald, A. H. Quantum Hall Ferromagnetism in Graphene. *Phys. Rev. Lett.* **96,** 256602 (25 2006).

66. Liu, J., Liu, J. & Dai, X. Pseudo Landau level representation of twisted bilayer graphene: Band topology and implications on the correlated insulating phase. *Phys. Rev. B* **99,** 155415 (15 2019).

67. Wu, S., Zhang, Z., Watanabe, K., Taniguchi, T. & Andrei, E. Y. Chern insulators, van Hove singularities and topological flat bands in magic-angle twisted bilayer graphene. *Nature materials* **20,** 488–494 (2021).

68. Nuckolls, K. P., Oh, M., Wong, D., Lian, B., Watanabe, K., Taniguchi, T., Bernevig, B. A. & Yazdani, A. Strongly correlated Chern insulators in magic-angle twisted bilayer graphene. *Nature* **588,** 610–615 (2020).

69. Saito, Y., Ge, J., Rademaker, L., Watanabe, K., Taniguchi, T., Abanin, D. A. & Young, A. F. Hofstadter subband ferromagnetism and symmetry-broken Chern insulators in twisted bilayer graphene. *Nature Physics* **17,** 478–481 (2021).

70. Tarnopolsky, G., Kruchkov, A. J. & Vishwanath, A. Origin of Magic Angles in Twisted Bilayer Graphene. *Phys. Rev. Lett.* **122,** 106405 (10 2019).

71. Lian, B., Song, Z.-D., Regnault, N., Efetov, D. K., Yazdani, A. & Bernevig, B. A. Twisted bilayer graphene. IV. Exact insulator ground states and phase diagram. *Phys. Rev. B* **103,** 205414 (20 2021).

72. Tschirhart, C., Serlin, M., Polshyn, H., Shragai, A., Xia, Z., Zhu, J., Zhang, Y., Watanabe, K., Taniguchi, T., Huber, M., *et al.* Imaging orbital ferromagnetism in a moiré Chern insulator. *Science* **372,** 1323–1327 (2021).

73. Claro, F. & Wannier, G. Magnetic subband structure of electrons in hexagonal lattices. *Physical review B* **19,** 6068 (1979).

74. Rammal, R. Landau level spectrum of Bloch electrons in a honeycomb lattice. *Journal de Physique* **46,** 1345–1354 (1985).

75. Geisler, M. C., Smet, J. H., Umansky, V., von Klitzing, K., Naundorf, B., Ketzmerick, R. & Schweizer, H. Detection of a Landau Band-Coupling-Induced Rearrangement of the Hofstadter Butterfly. *Phys. Rev. Lett.* **92,** 256801 (25 2004).

76. Albrecht, C., Smet, J. H., von Klitzing, K., Weiss, D., Umansky, V. & Schweizer, H. Evidence of Hofstadter's Fractal Energy Spectrum in the Quantized Hall Conductance. *Phys. Rev. Lett.* **86,** 147–150 (1 2001).

77. Albrecht, C., Smet, J. H., Weiss, D., von Klitzing, K., Hennig, R., Langenbuch, M., Suhrke, M., Rössler, U., Umansky, V. & Schweizer, H. Fermiology of Two-Dimensional Lateral Superlattices. *Phys. Rev. Lett.* **83,** 2234–2237 (11 1999).

78. Kuhl, U. & Stöckmann, H.-J. Microwave Realization of the Hofstadter Butterfly. *Phys. Rev. Lett.* **80,** 3232–3235 (15 1998).

79. Aidelsburger, M., Atala, M., Lohse, M., Barreiro, J. T., Paredes, B. & Bloch, I. Realization of the Hofstadter Hamiltonian with Ultracold Atoms in Optical Lattices. *Phys. Rev. Lett.* **111,** 185301 (18 2013).

80. Roushan, P., Neill, C., Tangpanitanon, J., Bastidas, V. M., Megrant, A., Barends, R., Chen, Y., Chen, Z., Chiaro, B., Dunsworth, A., Fowler, A., Foxen, B., Giustina, M., Jeffrey, E., Kelly, J., Lucero, E., Mutus, J., Neeley, M., Quintana, C., Sank, D., Vainsencher, A., Wenner, J., White, T., Neven, H., Angelakis, D. G. & Martinis, J. Spectroscopic signatures of localization with interacting photons in superconducting qubits. *Science* **358,** 1175–1179 (2017).

81. Hunt, B., Sanchez-Yamagishi, J. D., Young, A. F., Yankowitz, M., LeRoy, B. J., Watanabe, K., Taniguchi, T., Moon, P., Koshino, M., Jarillo-Herrero, P. & Ashoori, R. C. Massive Dirac Fermions and Hofstadter Butterfly in a van der Waals Heterostructure. *Science* **340,** 1427–1430 (2013).

82. Ponomarenko, L., Gorbachev, R., Yu, G., Elias, D., Jalil, R., Patel, A., Mishchenko, A., Mayorov, A., Woods, C., Wallbank, J., *et al.* Cloning of Dirac fermions in graphene superlattices. *Nature* **497,** 594–597 (2013).

83. Wang, L., Gao, Y., Wen, B., Han, Z., Taniguchi, T., Watanabe, K., Koshino, M., Hone, J. & Dean, C. R. Evidence for a fractional fractal quantum Hall effect in graphene superlattices. *Science* **350,** 1231–1234 (2015).

84. Kumar, R. K., Chen, X., Auton, G. H., Mishchenko, A., Bandurin, D. A., Morozov, S. V., Cao, Y., Khestanova, E., Shalom, M. B., Kretinin, A. V., Novoselov, K. S., Eaves, L., Grigorieva, I. V., Ponomarenko, L. A., Fal'ko, V. I. & Geim, A. K. High-temperature quantum oscillations caused by recurring Bloch states in graphene superlattices. *Science* **357,** 181–184 (2017).

85. Spanton, E. M., Zibrov, A. A., Zhou, H., Taniguchi, T., Watanabe, K., Zaletel, M. P. & Young, A. F. Observation of fractional Chern insulators in a van der Waals heterostructure. *Science* **360,** 62–66 (2018).

86. Yang, W., Lu, X., Chen, G., Wu, S., Xie, G., Cheng, M., Wang, D., Yang, R., Shi, D., Watanabe, K., Taniguchi, T., Voisin, C., Plaçais, B., Zhang, Y. & Zhang, G. Hofstadter Butterfly and Many-Body Effects in Epitaxial Graphene Superlattice. *Nano Letters* **16,** 2387–2392 (2016).

87. Chen, G., Sharpe, A. L., Fox, E. J., Zhang, Y.-H., Wang, S., Jiang, L., Lyu, B., Li, H., Watanabe, K., Taniguchi, T., *et al.* Tunable correlated Chern insulator and ferromagnetism in a moiré superlattice. *Nature* **579,** 56–61 (2020).

88. Herzog-Arbeitman, J., Chew, A., Efetov, D. K. & Bernevig, B. A. Reentrant Correlated Insulators in Twisted Bilayer Graphene at 25 T (2π Flux). *Phys. Rev. Lett.* **129,** 076401 (7 2022).

89. Song, Z., Wang, Z., Shi, W., Li, G., Fang, C. & Bernevig, B. A. All Magic Angles in Twisted Bilayer Graphene are Topological. *Phys. Rev. Lett.* **123,** 036401 (3 2019).

90. Po, H. C., Zou, L., Senthil, T. & Vishwanath, A. Faithful tight-binding models and fragile topology of magic-angle bilayer graphene. *Phys. Rev. B* **99,** 195455 (19 2019).

91. Ahn, J., Park, S. & Yang, B.-J. Failure of Nielsen-Ninomiya Theorem and Fragile Topology in Two-Dimensional Systems with Space-Time Inversion Symmetry: Application to Twisted Bilayer Graphene at Magic Angle. *Phys. Rev. X* **9,** 021013 (2 2019).

92. Lu, X., Stepanov, P., Yang, W., Xie, M., Aamir, M. A., Das, I., Urgell, C., Watanabe, K., Taniguchi, T., Zhang, G., *et al.* Superconductors, orbital magnets and correlated states in magic-angle bilayer graphene. *Nature* **574,** 653–657 (2019).

93. Stepanov, P., Xie, M., Taniguchi, T., Watanabe, K., Lu, X., MacDonald, A. H., Bernevig, B. A. & Efetov, D. K. Competing Zero-Field Chern Insulators in Superconducting Twisted Bilayer Graphene. *Phys. Rev. Lett.* **127,** 197701 (19 2021).

94. Bernevig, B. A., Lian, B., Cowsik, A., Xie, F., Regnault, N. & Song, Z.-D. Twisted bilayer graphene. V. Exact analytic many-body excitations in Coulomb Hamiltonians: Charge gap, Goldstone modes, and absence of Cooper pairing. *Phys. Rev. B* **103,** 205415 (20 2021).

95. Kang, J. & Vafek, O. Strong Coupling Phases of Partially Filled Twisted Bilayer Graphene Narrow Bands. *Phys. Rev. Lett.* **122,** 246401 (24 2019).

96. Lisi, S., Lu, X., Benschop, T., de Jong, T. A., Stepanov, P., Duran, J. R., Margot, F., Cucchi, I., Cappelli, E., Hunter, A., Tamai, A., Kandyba, V., Giampietri, A., Barinov, A., Jobst, J., Stalman, V., Leeuwenhoek, M., Watanabe, K., Taniguchi, T., Rademaker, L., van der Molen, S. J., Allan, M. P., Efetov, D. K. & Baumberger, F. Observation of flat bands in twisted bilayer graphene. *Nature Physics* **17,** 189–193 (2020).

97. Li, G., Luican, A., Lopes dos Santos, J., Castro Neto, A., Reina, A., Kong, J. & Andrei, E. Observation of Van Hove singularities in twisted graphene layers. *Nature physics* **6,** 109–113 (2010).

98. Xie, Y., Lian, B., Jäck, B., Liu, X., Chiu, C.-L., Watanabe, K., Taniguchi, T., Bernevig, B. A. & Yazdani, A. Spectroscopic signatures of many-body correlations in magic-angle twisted bilayer graphene. *Nature* **572,** 101–105 (2019).

99. Choi, Y., Kemmer, J., Peng, Y., Thomson, A., Arora, H., Polski, R., Zhang, Y., Ren, H., Alicea, J., Refael, G., *et al.* Electronic correlations in twisted bilayer graphene near the magic angle. *Nature Physics* **15,** 1174–1180 (2019).

100. Gupta, S. & Yakobson, B. I. What Dictates Rashba Splitting in 2D van der Waals Heterobilayers. *Journal of the American Chemical Society* **143,** 3503–3508 (2021).

101. Yin, J., Maity, P., Xu, L., El-Zohry, A. M., Li, H., Bakr, O. M., Brédas, J.-L. & Mohammed, O. F. Layer-dependent Rashba band splitting in 2D hybrid perovskites. *Chemistry of Materials* **30,** 8538–8545 (2018).

102. Liu, X., Chanana, A., Huynh, U., Xue, F., Haney, P., Blair, S., Jiang, X. & Vardeny, Z. Circular photogalvanic spectroscopy of Rashba splitting in 2D hybrid organic–inorganic perovskite multiple quantum wells. *Nature communications* **11,** 1–8 (2020).

103. Feng, Y., Jiang, Q., Feng, B., Yang, M., Xu, T., Liu, W., Yang, X., Arita, M., Schwier, E. F., Shimada, K., *et al.* Rashba-like spin splitting along three momentum directions in trigonal layered PtBi2. *Nature communications* **10,** 1–8 (2019).

104. Datta, B., Dey, S., Samanta, A., Agarwal, H., Borah, A., Watanabe, K., Taniguchi, T., Sensarma, R. & Deshmukh, M. M. Strong electronic interaction and multiple quantum Hall ferromagnetic phases in trilayer graphene. *Nature communications* **8,** 1–7 (2017).

105. Taychatanapat, T., Watanabe, K., Taniguchi, T. & Jarillo-Herrero, P. Quantum Hall effect and Landau-level crossing of Dirac fermions in trilayer graphene. *Nature Physics* **7,** 621–625 (2011).

106. Uri, A., Grover, S., Cao, Y., Crosse, J. A., Bagani, K., Rodan-Legrain, D., Myasoedov, Y., Watanabe, K., Taniguchi, T., Moon, P., *et al.* Mapping the twist-angle disorder and Landau levels in magic-angle graphene. *Nature* **581,** 47–52 (2020).

107. Herzog-Arbeitman, J., Chew, A., Efetov, D. K. & Bernevig, B. A. Reentrant Correlated Insulators in Twisted Bilayer Graphene at 25 T (2π Flux). *Phys. Rev. Lett.* **129,** 076401 (7 2022).

108. Jain, J. K. *Composite Fermions* (Cambridge University Press, 2007).

109. Lee, P. A., Nagaosa, N. & Wen, X.-G. Doping a Mott insulator: Physics of high-temperature superconductivity. *Rev. Mod. Phys.* **78,** 17–85 (1 2006).

110. Nilsson, F., Karlsson, K. & Aryasetiawan, F. Dynamically screened Coulomb interaction in the parent compounds of hole-doped cuprates: Trends and exceptions. *Phys. Rev. B* **99,** 075135 (7 2019).

111. Yankowitz, M., Chen, S., Polshyn, H., Zhang, Y., Watanabe, K., Taniguchi, T., Graf, D., Young, A. F. & Dean, C. R. Tuning superconductivity in twisted bilayer graphene. *Science* **363,** 1059–1064 (2019).

112. Goodwin, Z. A. H., Corsetti, F., Mostofi, A. A. & Lischner, J. Twist-angle sensitivity of electron correlations in moiré graphene bilayers. *Phys. Rev. B* **100,** 121106 (12 2019).

113. Pizarro, J. M., Rösner, M., Thomale, R., Valentı, R. & Wehling, T. O. Internal screening and dielectric engineering in magic-angle twisted bilayer graphene. *Phys. Rev. B* **100,** 161102 (16 2019).

114. Koshino, M., Yuan, N. F. Q., Koretsune, T., Ochi, M., Kuroki, K. & Fu, L. Maximally Localized Wannier Orbitals and the Extended Hubbard Model for Twisted Bilayer Graphene. *Phys. Rev. X* **8,** 031087 (3 2018).

115. Polshyn, H., Yankowitz, M., Chen, S., Zhang, Y., Watanabe, K., Taniguchi, T., Dean, C. R. & Young, A. F. Large linear-in-temperature resistivity in twisted bilayer graphene. *Nature Physics* **15,** 1011–1016 (2019).

116. Cao, Y., Chowdhury, D., Rodan-Legrain, D., Rubies-Bigorda, O., Watanabe, K., Taniguchi, T., Senthil, T. & Jarillo-Herrero, P. Strange Metal in Magic-Angle Graphene with near Planckian Dissipation. *Phys. Rev. Lett.* **124,** 076801 (7 2020).

117. Hussey, N. E., Mackenzie, A. P., Cooper, J. R., Maeno, Y., Nishizaki, S. & Fujita, T. Normal-state magnetoresistance of Sr_2RuO_4. *Phys. Rev. B* **57,** 5505–5511 (9 1998).

118. Klein, L., Dodge, J. S., Ahn, C. H., Snyder, G. J., Geballe, T. H., Beasley, M. R. & Kapitulnik, A. Anomalous Spin Scattering Effects in the Badly Metallic Itinerant Ferromagnet $SrRuO_3$. *Phys. Rev. Lett.* **77,** 2774–2777 (13 1996).

119. Li, S. Y., Taillefer, L., Hawthorn, D. G., Tanatar, M. A., Paglione, J., Sutherland, M., Hill, R. W., Wang, C. H. & Chen, X. H. Giant Electron-Electron Scattering in the Fermi-Liquid State of $Na_{0.7}CoO_2$. *Phys. Rev. Lett.* **93,** 056401 (5 2004).

120. Wang, Y., Rogado, N. S., Cava, R. J. & Ong, N. P. Spin entropy as the likely source of enhanced thermopower in $Na_xCo_2O_4$. *Nature* **423,** 425–428 (2003).

121. Philip Phillips, P. P. *Advanced solid state physics* illustrated edition (Westview Press, 2002).

122. Franz, R. & Wiedemann, G. Ueber die Wärme-Leitungsfähigkeit der Metalle. *Annalen der Physik* **165,** 497–531 (1853).

123. Liu, X., Wang, Z., Watanabe, K., Taniguchi, T., Vafek, O. & Li, J. I. A. Tuning electron correlation in magic-angle twisted bilayer graphene using Coulomb screening. *Science* **371,** 1261–1265 (2021).

124. Rozen, A., Park, J. M., Zondiner, U., Cao, Y., Rodan-Legrain, D., Taniguchi, T., Watanabe, K., Oreg, Y., Stern, A., Berg, E., *et al.* Entropic evidence for a Pomeranchuk effect in magic-angle graphene. *Nature* **592,** 214–219 (2021).

125. Saito, Y., Yang, F., Ge, J., Liu, X., Taniguchi, T., Watanabe, K., Li, J., Berg, E. & Young, A. F. Isospin Pomeranchuk effect in twisted bilayer graphene. *Nature* **592,** 220–224 (2021).

126. Wu, F., Hwang, E. & Das Sarma, S. Phonon-induced giant linear-in-T resistivity in magic angle twisted bilayer graphene: Ordinary strangeness and exotic superconductivity. *Phys. Rev. B* **99,** 165112 (16 2019).

127. Proust, C. & Taillefer, L. The Remarkable Underlying Ground States of Cuprate Superconductors. *Annual Review of Condensed Matter Physics* **10,** 409–429 (2019).

128. Greene, R. L., Mandal, P. R., Poniatowski, N. R. & Sarkar, T. The Strange Metal State of the Electron-Doped Cuprates. *Annual Review of Condensed Matter Physics* **11,** 213–229 (2020).

129. Grigera, S. A., Perry, R. S., Schofield, A. J., Chiao, M., Julian, S. R., Lonzarich, G. G., Ikeda, S. I., Maeno, Y., Millis, A. J. & Mackenzie, A. P. Magnetic Field-Tuned Quantum Criticality in the Metallic Ruthenate Sr¡sub¿3¡/sub¿Ru¡sub¿2¡/sub¿O¡sub¿7¡/sub¿. *Science* **294,** 329–332 (2001).

130. Shibauchi, T., Carrington, A. & Matsuda, Y. A Quantum Critical Point Lying Beneath the Superconducting Dome in Iron Pnictides. *Annual Review of Condensed Matter Physics* **5,** 113–135 (2014).

131. Löhneysen, H. v., Pietrus, T., Portisch, G., Schlager, H. G., Schröder, A., Sieck, M. & Trappmann, T. Non-Fermi-liquid behavior in a heavy-fermion alloy at a magnetic instability. *Phys. Rev. Lett.* **72,** 3262–3265 (20 1994).

132. Ghiotto, A., Shih, E.-M., Pereira, G. S., Rhodes, D. A., Kim, B., Zang, J., Millis, A. J., Watanabe, K., Taniguchi, T., Hone, J. C., *et al.* Quantum criticality in twisted transition metal dichalcogenides. *Nature* **597,** 345–349 (2021).

133. Zaanen, J. Why the temperature is high. *Nature* **430,** 512–513 (2004).

134. Legros, A., Benhabib, S., Tabis, W., Laliberté, F., Dion, M., Lizaire, M., Vignolle, B., Vignolles, D., Raffy, H., Li, Z., *et al.* Universal T-linear resistivity and Planckian dissipation in overdoped cuprates. *Nature Physics* **15,** 142–147 (2019).

135. Daou, R., Doiron-Leyraud, N., LeBoeuf, D., Li, S., Laliberté, F., Cyr-Choiniere, O., Jo, Y., Balicas, L., Yan, J.-Q., Zhou, J.-S., *et al.* Linear temperature dependence of resistivity and change in the Fermi surface at the pseudogap critical point of a high-Tc superconductor. *Nature Physics* **5,** 31–34 (2009).

136. Giraldo-Gallo, P., Galvis, J. A., Stegen, Z., Modic, K. A., Balakirev, F. F., Betts, J. B., Lian, X., Moir, C., Riggs, S. C., Wu, J., Bollinger, A. T., He, X., Božović, I., Ramshaw, B. J., McDonald, R. D., Boebinger, G. S. & Shekhter, A. Scale-invariant magnetoresistance in a cuprate superconductor. *Science* **361,** 479–481 (2018).

137. Hayes, I. M., McDonald, R. D., Breznay, N. P., Helm, T., Moll, P. J., Wartenbe, M., Shekhter, A. & Analytis, J. G. Scaling between magnetic field and temperature in the high-temperature superconductor BaFe2 (As1- xPx) 2. *Nature Physics* **12,** 916–919 (2016).

138. Saito, Y., Ge, J., Watanabe, K., Taniguchi, T. & Young, A. F. Independent superconductors and correlated insulators in twisted bilayer graphene. *Nature Physics* **16,** 926–930 (2020).

139. Serlin, M., Tschirhart, C. L., Polshyn, H., Zhang, Y., Zhu, J., Watanabe, K., Taniguchi, T., Balents, L. & Young, A. F. Intrinsic quantized anomalous Hall effect in a moiré heterostructure. *Science* **367,** 900–903 (2020).

140. Sharpe, A. L., Fox, E. J., Barnard, A. W., Finney, J., Watanabe, K., Taniguchi, T., Kastner, M. A. & Goldhaber-Gordon, D. Emergent ferromagnetism near three-quarters filling in twisted bilayer graphene. *Science* **365,** 605–608 (2019).

141. Ledwith, P. J., Tarnopolsky, G., Khalaf, E. & Vishwanath, A. Fractional Chern insulator states in twisted bilayer graphene: An analytical approach. *Phys. Rev. Res.* **2,** 023237 (2 2020).

142. Khalaf, E., Chatterjee, S., Bultinck, N., Zaletel, M. P. & Vishwanath, A. Charged skyrmions and topological origin of superconductivity in magic-angle graphene. *Science Advances* **7,** eabf5299 (2021).

143. Po, H. C., Zou, L., Vishwanath, A. & Senthil, T. Origin of Mott Insulating Behavior and Superconductivity in Twisted Bilayer Graphene. *Phys. Rev. X* **8,** 031089 (3 2018).

144. Zhang, Y.-H., Po, H. C. & Senthil, T. Landau level degeneracy in twisted bilayer graphene: Role of symmetry breaking. *Phys. Rev. B* **100,** 125104 (12 2019).

145. Zhang, Y.-H., Mao, D. & Senthil, T. Twisted bilayer graphene aligned with hexagonal boron nitride: Anomalous Hall effect and a lattice model. *Phys. Rev. Res.* **1,** 033126 (3 2019).

146. Rodan-Legrain, D., Cao, Y., Park, J. M., de la Barrera, S. C., Randeria, M. T., Watanabe, K., Taniguchi, T. & Jarillo-Herrero, P. Highly tunable junctions and non-local Josephson effect in magic-angle graphene tunnelling devices. *Nature Nanotechnology* **16,** 769–775 (2021).

147. De Vries, F. K., Portoles, E., Zheng, G., Taniguchi, T., Watanabe, K., Ihn, T., Ensslin, K. & Rickhaus, P. Gate-defined Josephson junctions in magic-angle twisted bilayer graphene. *Nature Nanotechnology* **16,** 760–763 (2021).

148. Diez-Merida, J., Dıez-Carlón, A., Yang, S., Xie, Y.-M., Gao, X.-J., Watanabe, K., Taniguchi, T., Lu, X., Law, K. T. & Efetov, D. K. Magnetic Josephson junctions and superconducting diodes in magic angle twisted bilayer graphene. *arXiv preprint arXiv:2110.01067* (2021).

149. Seifert, P., Lu, X., Stepanov, P., Durán Retamal, J. R., Moore, J. N., Fong, K.-C., Principi, A. & Efetov, D. K. Magic-Angle Bilayer Graphene Nanocalorimeters: Toward Broadband, Energy-Resolving Single Photon Detection. *Nano Letters* **20,** 3459–3464 (2020).

150. Di Battista, G., Seifert, P., Watanabe, K., Taniguchi, T., Fong, K. C., Principi, A. & Efetov, D. K. Revealing the Thermal Properties of Superconducting Magic-Angle Twisted Bilayer Graphene. *Nano Letters* **22,** 6465–6470 (2022).

151. Saha, S., Kahya, O., Jaiswal, M., Srivastava, A., Annadi, A., Balakrishnan, J., Pachoud, A., Toh, C.-T., Hong, B.-H., Ahn, J.-H., *et al.* Unconventional transport through graphene on SrTiO3: a plausible effect of SrTiO3 phase-transitions. *Scientific reports* **4,** 1–6 (2014).

152. Ryu, H., Hwang, J., Wang, D., Disa, A. S., Denlinger, J., Zhang, Y., Mo, S.-K., Hwang, C. & Lanzara, A. Temperature-dependent electron–electron interaction in graphene on SrTiO3. *Nano letters* **17,** 5914–5918 (2017).

153. Sun, J., Gao, T., Song, X., Zhao, Y., Lin, Y., Wang, H., Ma, D., Chen, Y., Xiang, W., Wang, J., Zhang, Y. & Liu, Z. Direct Growth of High-Quality Graphene on High- Dielectric SrTiO3 Substrates. *Journal of the American Chemical Society* **136,** 6574–6577 (2014).